# PREDICTING THE ONSET OF ABNORMAL CARDIAC RHYTHMS

THOMAS QUAIL

DOCTOR OF PHILOSOPHY

DEPARTMENT OF PHYSIOLOGY

MCGILL UNIVERSITY
MONTREAL, QUEBEC
JULY 2015

A THESIS SUBMITTED TO MCGILL UNIVERSITY IN PARTIAL FULFILLMENT OF THE REQUIREMENTS FOR THE DEGREE OF DOCTOR OF PHILOSOPHY

© Thomas Quail 2015

# **DEDICATION**

This thesis is dedicated to my parents, Paddy and Rhona, and my sister, Emma, for their love and support. And to Zoë, my best friend, with whom I couldn't imagine life without.

#### ACKNOWLEDGEMENTS

I first wish to thank my supervisors Leon Glass and Alvin Shrier for their support and supervision over the course of my graduate degree. It has been a pleasure and a privilege to work with both of you on these fascinating problems. I deeply appreciate all the opportunities that you provided for me. I would also like to thank both Michael Mackey and Michael Guevera. My interactions with both of you have been very meaningful, and have considerably shaped my thoughts and approaches to complicated scientific problems. A big thank-you to all the students, post-docs, musicians, and friends with whom I have had contact with throughout the course of my PhD; these day-in, day-out interactions inject joy and meaning into my life. In no particular order: Matthew Leavitt, Lennart Hilbert, Greg Stacey, Rob Gulli, Jane Chan, Bernard Rudny, TK Shajahan, Bart Borek, Zhubo Zhang, Corey Valinsky, Brian Foo, Christine Hantouche, Brittany Williamson, Romain Yvinec, Mike Bjella, Anne-Sophie Berg, Chris Whitley, Amy Hillis, Kate Maloney, Daniel Zysman, Kate Ye Zhao, and the members of the Il Medici di McGill Orchestra. Also I would very much like to thank the administrative staff from the Department of Physiology, who all work very hard to facilitate and improve our experiences as graduate students.

## ABSTRACT

The normal cardiac rhythm can undergo transitions that lead to serious cardiac arrhythmias. In this thesis, I examine these transitions using simplified experimental cardiac models and tools from nonlinear dynamics. Treating spontaneously beating aggregates of embryonic chick cardiac cells with a potassium channel blocker can induce a spectrum of complex dynamics, including highly irregular rhythms. In the first study, I suggest that these irregular rhythms are chaotic and are initiated through a sequence of period-doubling bifurcations. Potassium channel blockade can also lead to the onset of proarrhythmic alternating rhythms through a period-doubling bifurcation. In the second study, I develop a quantitative early warning signal that provides insight into how far the system is from the onset of the period-doubling bifurcation. Alternating rhythms precede the onset of reentrant arrhythmias, which can be driven by spiral waves, self-sustaining vortices of electrical activity. In the third study, I explore mechanisms of spiral wave initiation by introducing inexcitable regions into 1-cm-diameter monolayers composed of embryonic chick cardiac cells, and tracking the dynamics using intracellular calcium imaging. In particular, I find that the location of the inexcitable region in combination with the side pacemaker frequency determines spiral wave rotation direction (chirality). In this system, I also find that an instability in the dynamics of the action potential duration in localized regions of the substrate acts as a precursor of spiral wave initiation.

## ABRÉGÉ

Un rythme cardiaque normal peut subir des transitions qui mènent à des arythmies graves. Cette thèse examine ces transitions en utilisant des modèles cardiaques expérimentaux simplifiés et des méthodes de dynamique non linéaire. Le traitement d'agrégats de cellules cardiaques embryonnaires de poussin battant spontanément avec un inhibiteur de potassium peut provoquer une gamme de dynamiques complexes, y compris des rythmes très irréguliers. Dans la première étude, je suggère que ces rythmes irréguliers sont chaotiques et sont démarrés au cours d'une séquence de bifurcations de dédoublement de période. Le blocage des canaux potassiques peut également entraîner l'apparition d'alternances proarythmiques par une bifurcation de dédoublement de priode. Dans la seconde étude, je développe un signal quantitatif d'alerte précoce qui permet de mieux comprendre l'état du système précédant l'apparition de la bifurcation de dédoublement de période. L'alternance précède l'apparition d'arythmies réentrantes, qui peuvent être entraînées par des ondes spiralées (des tourbillons d'activité électrique qui s'auto-entretiennent). Dans la troisième étude, j'explore les mécanismes de l'initiation d'ondes spiralées en introduisant des régions inexcitables dans des monocouches de 1cm de diamètre composées de cellules cardiaques embryonnaires de poussin, et le suivi des dynamiques à l'aide de l'imagerie de calcium intracellulaire. Notamment, je découvre que l'emplacement de la région inexcitable en combinaison avec la fréquence du stimulateur latérale dtermine le sens de rotation d'ondes spiralées (chiralité). Dans ce systme, je trouve aussi que l'instabilité

des dynamiques de la durée du potentiel d'action dans des régions localisées du substrat agit comme un précurseur de l'initiation d'ondes spiralées.

## **PREFACE**

The heart is remarkably robust. It beats each second, ensuring that oxygen and nutrients reach every cell in the body. Disruptions to this process have existential consequences. In this thesis, I examine the dynamics underlying the onset of abnormal cardiac rhythms associated with life-threatening cardiac arrhythmias. Tackling this problem necessitates providing insight into the nature of these transition. Tools from nonlinear dynamics and bifurcation theory applied to simplified experimental cardiac models has proved fruitful in tackling this problem, shedding insight into the *dynamic* mechanism of these transitions. All three studies in this manuscript-based thesis are grounded in this approach: developing and analyzing nonlinear models based on experimental data to gain insight into transitions associated with the onset of abnormal cardiac rhythms. From this perspective, this thesis makes three original contributions to our understanding of abnormal cardiac rhythms. First, I show that treating aggregates of cardiac cells with a potassium channel blocker can induce chaotic dynamics. Second, I develop a quantitative measure that assesses how far the dynamics of aggregates of cardiac cells treated with a potassium channel blocker are from the onset of clinically relevant alternating rhythms. Lastly, I show that the position of an inexcitable region with respect to a side pacing region can control spiral wave chirality preference.

## CONTRIBUTIONS OF VARIOUS AUTHORS

Chapter 2 is based on a manuscript Chaotic dynamics in cardiac aggregates induced by potassium channel block, by Thomas Quail, Nevin McVicar, Martin Aguilar, Min-Young Kim, Alex Hodge, Leon Glass, Alvin Shrier, Chaos, 22, 033140, (2012). The experiments were performed in the laboratory of Alvin Shrier by Min-Young Kim and Alex Hodge. Myself and Nevin McVicar developed the nonlinear map model simulating the chaotic dynamics. Myself and Martin Aguilar performed and analyzed the results from the numerical simulations of the ionic model. I wrote the manuscript under the supervision of Leon Glass and Alvin Shrier.

Chapter 3 is based on a manuscript **Predicting the onset of period-doubling bifurcations in noisy cardiac systems**, by Thomas Quail, Alvin Shrier, Leon Glass, currently in revisions at *Proceedings from the National Academy of Sciences USA*. The experiments were performed in the laboratory of Alvin Shrier by Min-Young Kim and Alex Hodge. I analyzed the data, developed the theory, and performed the numerical simulations for this study. I wrote the manuscript under the supervision of Leon Glass and Alvin Shrier.

Chapter 4 is based on a manuscript Spatial Symmetry Breaking Determines Spiral Wave Chirality, by Thomas Quail, Alvin Shrier, Leon Glass, *Physical review letters*, **113**, 158101, (2014). I performed the experiments in the

laboratory of Alvin Shrier. I collected and analyzed the experimental data. I performed the numerical simulations and analysis of the mathematical model. I wrote the manuscript under the supervision of Leon Glass and Alvin Shrier.

# TABLE OF CONTENTS

DEI	DICATI	ON
ACK	(NOW	LEDGEMENTS iii
ABS	TRAC	$\Gamma$ iv
ABF	RÉGÉ	
PRE	EFACE	
CON	NTRIB	UTIONS OF VARIOUS AUTHORS viii
LIST	ΓOF F	IGURES xiii
1	Introd	uction
	1.1 1.2 1.3 1.4	Physiology of the heart
2	Chaot	ic cardiac dynamics induced by potassium channel block
	2.1 2.2	Foreword

		2.2.3 Optical imaging technique	37
	2.3		38
		2.3.1 Intracellular recordings	38
		2.3.2 Optical recording examples	39
		2.3.3 Phenomenological model	41
			43
	2.4	Discussion	45
3	Pred	icting the onset of abnormal alternating rhythms	54
	3.1	Foreword	54
	3.2	Results	56
		3.2.1 Onset of alternating rhythms	56
		3.2.2 Analysis of early warning signals	58
		3.2.3 Quantitative measure that predicts the onset of alternat-	
		ing rhythms	62
	3.3	Discussion	64
	3.4	Methods	66
		1 0 00 0	66
			67
		3.4.3 Numerical simulations of the nonlinear model	67
		3.4.4 Slope and autocorrelation calculated from the inter-beat	
			68
		3.4.5 Slope and autocorrelation calculated from the numerical	co
		simulations	68
4	Spati	al symmetry breaking determines spiral wave chirality	76
	4.1	Foreword	76
	4.2	Experimental methods	76
		4.2.1 Introducing inexcitable regions into cardiac monolayers	76
	4.3	•	78
		4.3.1 Spiral wave diversity in monolayers with inexcitable regions	78
	4.4	Theoretical methods	79
		4.4.1 Rapid pacing leads to the onset of spiral waves	79
	4.5		80
			80
			81
		4.5.3 Action potential duration restitution curve analysis	82

	4.6	Discussion	84
5	Conclu	usions and Future Directions	93
App	endix A	A: Ionic model	99
Refe	rences		106

## LIST OF FIGURES

Figure		page
1–1	FitzHugh-Nagumo model of action potential	34
2-1	Irregular rhythms following potassium channel block	49
2-2	Drug-induced chaotic dynamics	50
2-3	Additional example of drug-induced chaotic dynamics	51
2-4	Bifurcation diagrams of mathematical models displaying chaos	52
2-5	Drug-induced chaotic dynamics in ionic model	53
3-1	Drug-induced period-doubling bifurcation	70
3-2	Early warning signals of drug-induced instability	71
3-3	Analysis of early warning signals using linear map	72
3-4	Analysis of early warning signals using nonlinear map	73
3–5	Quantitative measure predicts onset of alternating rhythms	74
3-6	Measure predicts onset of alternating rhythms for nonlinear map	75
4–1	Spiral wave propagation in cardiac monolayers	86
4-2	Rapid pacing generates spiral wave in cardiac monolayer	87
4-3	Spiral wave propagation in mathematical model of the experiments. $% \left( 1\right) =\left( 1\right) \left( 1\right) \left$	88
4-4	Rapid pacing generates spiral waves in mathematical model	89
4-5	Spiral wave chirality as a function of pacemaker period	90
4-6	Frequency-dependent spiral wave chirality behaviors	91
4-7	Instabilities are consistent with transition in spiral wave chirality	92

## CHAPTER 1 Introduction

Over the course of a lifetime, the heart maintains remarkably stable dynamics within a noisy, nonlinear, spatially-extended environment. Every second, a depolarizing wave of excitation propagates throughout the four chambers of the heart, giving rise to a well-coordinated contraction. This process, termed normal sinus rhythm, represents one of the body's fundamental physiological rhythms. Life-threatening cardiac arrhythmias are associated with transitions in the qualitative dynamics of this process. From a mathematical perspective, transitions in the dynamics of complex systems can be associated with bifurcations in the dynamics observed in mathematical models, where the value of a control parameter goes through a critical point leading to the establishment of qualitatively different dynamics. Mackey and Glass first introduced the idea of dynamical disease, which linked bifurcations that arise as a consequence of a change in the value of a model parameter with the onset of human pathology [86, 139]. Since then, this approach has provided insights into potential mechanisms associated with a number of human diseases, including epilepsy [146], respiratory arrest [162], Parkinson's [15], and cardiac arrhythmias [91].

In this thesis, I focus on the initiation of abnormal cardiac rhythms by examining the dynamics of these transitions. In recent years, tools from nonlinear dynamics and dynamical systems have been useful in exploring these problems. Here, I show that this approach can provide insight into a clinically relevant question: can you predict the onset of abnormal cardiac rhythms?

Treating spontaneously beating aggregates of embryonic chick cardiac cells can induce highly irregular rhythms. In the first study of this dissertation, I show that these irregular rhythms are chaotic, and are generated through a sequence of period-doubling bifurcations. Period-doubling bifurcations can also lead to the onset of proarrhythmic alternating rhythms. In the second study, I develop early warning signals that predict the onset of alternating rhythms observed in the beat patterns of aggregates following potassium channel blockade. Alternating rhythms have been linked to the onset of reentrant arrhythmias that are thought to be driven by spiral waves. In the third study, I explore spiral wave initiation by introducing inexcitable obstacles into 1-cm-diameter cardiac monolayers. Numerically simulating this system shows that the position of the obstacle governs spiral wave rotation direction ('chirality').

## 1.1 Physiology of the heart

The central function of the heart is to pump blood throughout the body. To carry this out, there exists an elegantly designed interplay between the heart's spatial structure, the conduction properties of cardiac tissue, and the contractile properties of the organ. In the following section, I will briefly outline how all these dynamic parts collectively give rise to the proper functioning of the heart.

The heart is divided into four chambers: the right and left atria, which represent the upper chambers; and the right and left ventricles, which represent the lower chambers. These chambers contract in a well-coordinated fashion,

which leads to the ejection of deoxygenated blood to the lungs and oxygenated blood to the rest of the body. The heart's electrical conduction system governs the timing of these contractions. Most cardiac cells have both contractile and electrical properties. In particular, cardiac cells propagate action potentials—the fundamental electrical signal of the heart representing the wave of excitation—and, consequently, the action potential causes these cells to contract.

Approximately every second, specialized pacemaker cells in the sino-atrial (SA) node—located in the right atrium—depolarize, giving rise to an action potential. This wave of excitation propagates first throughout the atria, leading to the atrial contraction. The atrioventricular (AV) node connects the atria and the ventricles, allowing the wave of excitation to propagate from the heart's upper chambers to the lower chambers. The cardiac impulse rapidly exits the atrioventricular node through the bundle of His, which leads to the right and left bundle branches of the Purkinje network. Finally, the cardiac impulse propagates through the Purkinje network, which gives rise to the excitation and subsequent contraction of the right and left ventricles. The conduction velocity of the wave of excitation through the cardiac conduction pathways depends on a number of factors, including location within the heart, direction of propagation, action potential upstroke velocity, and the coupling between cells via gap functions. The conduction velocities range from approximately 0.05 m/s in the atrioventricular node to 2 m/s within the Purkinje network [118]. Additionally, the anistropic nature of the heart, wherein cells are preferentially oriented along specific fiber

directions, induces differences between longitudinal and transverse propagation—0.5 m/s as compared to 0.2 m/s in ventricular muscle [118].

The dynamics of the action potential are governed by the opening and closing of voltage-sensitive ion channels that mediate the flow of sodium, potassium, and calcium across the cell membrane. A great deal of work has been conducted on determining how the interactions between the nonlinear responses of ion channels and the balance of extra- and intracellular ionic concentrations give rise to action potentials. This thesis largely focuses on more macroscopic dynamical properties of cardiac systems, but, that being said, I will provide a brief overview of the generation of action potentials (for a review see [95]).

At rest, differences in the ionic concentrations across the membrane govern the membrane potential, which in isolated human cardiac cells is between -80 and -90 mV [134, 57]. Upon activation, sodium channels open, allowing sodium to flow from outside to inside the cell (along its concentration gradient), giving rise to the upstroke leading to depolarization of the membrane voltage to approximately +20 mV [134, 196]. Next, during the plateau phase, depolarizing currents mediated by calcium-specific channels balance the repolarizing potassium-specific currents. This plateau phase prolongs the action potential—in human cardiac cells, the duration of the action potential is roughly 250 msec [149]. In the repolarizing phase of the action potential, the cell's membrane voltage is brought back to its resting membrane potential through the activity of potassium channels.

The heart is made up of cell types with varying functions and electrophysiological properties. In general, cardiac cells can be classified as being either a

pacemaker or an excitable cell. Pacemaker cells in the sinoatrial node discharge periodically leading to the initiation of the normal sinus rhythm. Rather than returning to the resting membrane potential following repolarization, pacemaker cells undergo depolarization as a consequence of a number of ion-channel-mediated currents, most notably  $I_f$ , a hyperpolarization-activated pacemaker current [200]. Excitable cardiac cells, on the other hand, nonlinearly respond to the wave of excitation emanating from the pacemaker cells but do not intrinsically generate action potentials. Hence, during normal sinus rhythm, pacemaker cells 'entrain' the dynamics of the heart's excitable cells, thus governing heart rate.

In this thesis, I examine the dynamics associated with the onset of abnormal cardiac rhythms. In patients with cardiac arrhythmias, cardiologists examine ECG recordings to characterize the mechanism underlying the arrhythmia. However, the human heart is a complex, three-dimensional structure, and ECG recordings often do not provide the level of detail necessary to resolve these mechanistic properties associated with the onset cardiac arrhythmias. Consequently, simplified animal models are used to provide insight into the mechanisms of these processes

#### 1.2 Experimental models of the heart

Simplified experimental models of the heart span all spatial scales. Here, I provide a survey of the simplified animal models that have been used to provide insight into the mechanisms of abnormal cardiac rhythms.

(1) Zero-dimensional models: Examining the dynamics of spontaneously beating aggregates of cardiac cells represents a method of studying beat patterns in response to various stimuli. In particular, DeHaan developed a method to generate

spontaneously beating aggregates of embryonic chick cardiac cells [54]. From a dynamics perspective, aggregates act as pacemakers, and have been used to examine the response of the cardiac rhythm to single depolarizing pulses [89] and periodic stimulation [90, 91, 127]. In these studies, the dynamics were tracked using electrodes that measure intracellular electrical activity. Spontaneously beating aggregates of cardiac cells have also been used to examine changes in dynamics following the treatment of drugs that target ion channels, including the hERG potassium channel [117]. Chapters 2 and 3 are based on a data set first presented in [117], where aggregates were treated with a hERG potassium channelspecific drug E4031. Single cells isolated from tissue preparations represents an experimental model that has also been used to examine cardiac dynamics [55, 77]. (2) One-dimensional cables: Periodic stimulation of a strip of Purkinje fiber represents a well-studied experimental system that has been used to examine a number of cardiac rhythms, transitions between rhythms, and additional properties, including alternating rhythms [39], chaotic dynamics [39], control of abnormal alternating rhythms [41], and onset of conduction block [74]. To examine the dynamics of waves propagating around rings of cardiac tissue, the tissue around the tricuspid valve—the valve linking the right atrium with the right ventricle—has also been used [75].

(3) Two-dimensional sheets: Optical imaging of cardiac monolayers, two-dimensional sheets of interconnected cardiac cells, using calcium- and voltage-sensitive dyes has provided insights into the study of the initiation [22, 24] and termination [2] mechanisms of spiral waves; the dynamics of spiral waves [27]; the

effects of geometry on cardiac dynamics [10]; spatial dynamics of early afterdepolarizations [32]; and the interactions of multiple pacemakers [21]. In chapter 4, I use 1-cm-diameter cardiac monolayers composed of 7-8-day-old embryonic chick cardiac cells to examine how inexcitable regions influence the dynamics of spiral waves.

(4) Three-dimensional measurements: Examining intramural propagation in whole hearts represents a technically challenging problem for which data is scarce [96]. Arrays of microelectrodes that detect electrical activity can be inserted through the heart's walls [60]. Optical fibers have also been used to image transmembrane voltage through the heart's walls using fluorescence from a voltage-sensitive dye [120]. Much work remains towards improving the techniques of imaging wavefront propagation in three dimensions.

## 1.3 Mathematical models of the heart

Mathematical modelling can propose mechanisms to deepen our understanding of experimental data and make predictions that guide the types of experiments that are performed. Furthermore, computational models can provide insight into the types of transitions that take place in the genesis of abnormal cardiac rhythms in experiments.

In 1928, van der Pol and van der Mark first modelled the electrical activity of the heart by coupling oscillators representing the sinus, the atria, and the ventricles together [199]. The model generates stable oscillations and captures a number of properties associated with cardiac function, including an alternation between slow build-up phases and rapid release phases, refractory period, and

all-or-nothing responses to external stimuli. However, at the time, the cellular mechanism underlying these processes in the heart was unclear.

In 1952, Hodgkin and Huxley published a set of landmark studies showing that the propagation of a nerve impulse along the squid's giant axon is mediated by voltage-dependent ion currents [98, 97, 99, 101, 100]. Hodgkin and Huxley also quantitatively described the process, modelling the dynamics of the wave propagation using a set of differential equations which accounted for voltage-dependent sodium, potassium, and leak currents [100]. Neurons and cardiac cells share many properties. However, there are differences in the kinetic properties of the action potential (for example, the duration of the action potential is far longer in cardiac cells than in neurons), and there are also differences in the propagation properties of the wave of excitation and network structure (neurons have axons that are connected by synapses; in contrast, cardiac tissue is composed of intercalated cardiomyocytes arranged in brick-like geometries). Noble used Hodgkin and Huxley's work as a basis to develop an ionic model of the cardiac action potential observed in Purkinje fibers [153].

Since then, there has been a wellspring of research devoted towards the development of cardiac models of the action potential based on ionic currents. These models have exponentially increased in complexity—some models have upwards of 60 dynamic variables [107]—as additional ion-channel-mediated currents and features such as intracellular calcium handling are included. Models have been developed for a number of species; for example, there are models of the action potential for mouse [20], rat [158], rabbit [140], canine [37], guinea pig [137],

and human [196, 37]. Ionic models based on currents from the sinoatrial node and the atria have also been proposed [67]. Analyzing these ever-increasingly complex models is difficult, which makes it tricky to gain mechanistic insight into the dynamics. Consequently, the relevance of these models in the context of improving our understanding of transitions in the normal cardiac rhythm remain to be seen.

## 1.3.1 Excitable media

Cardiac cells are connected together in a brick-like network through which the action potential propagates, giving rise to the wave of excitation that entrains the dynamics of the heart. Given these properties, the heart is a representative example of excitable media.

In response to small-amplitude perturbations, the dynamics of excitable systems rapidly return to the system's stable steady-state value. In response to high-amplitude perturbations—sufficiently strong to carry the system across a threshold—a nonlinear all-or-nothing response takes place, where the return to the system's steady-state value takes place on a longer time scale. Following the all-or-nothing response, excitable systems are refractory to additional stimulation until the system has recovered for a given time window. An excitable medium is a spatially-extended system that is composed of local units that are excitable [198]. The interaction of these local units via a diffusive mechanism can give rise to traveling waves of excitation [198]. Examples abound of excitable media in biological and chemical systems: forest fires [11], neurons [100], spreading waves of depression in the cerebral cortex [121], chemical reactions such as the Belousov-Zhabotinsky reaction [150], and cAMP signalling in slime mould [130].

Again, the heart is an example of an excitable medium: (1) cardiac cells generate action potentials, all-or-nothing responses to stimuli; (2) cardiac cells are refractory during and following the generation of an action potential; and (3) cardiac cells propagate and sustain wavefronts. Consequently, generic models of excitable media—often much simpler than Hodgkin-Huxley-style ionic models—can be used examine the dynamics of the heart. Below, I will discuss the properties of a generic model that has been used extensively to simulate the heart's dynamics.

Following the development of the Hodkgin-Huxley model, FitzHugh [73] and Nagumo [151] sought to reduce the complexity of the Hodgkin-Huxley equations, while extracting the central mathematical features of wave propagation in the squid giant axon: excitability, propagation, and refractoriness. Since then, this model—termed the FitzHugh-Nagumo model—has been used to study myriad dynamical features of the heart, including the motion of spiral waves through cardiac tissue [213], the interaction of multiple spiral waves [62], the coexistence of spiral waves with alternative stable periods [212], unidirectional pulses of activity around a ring of cardiac tissue [155, 85], the interaction of multiple pacemakers [21], and the interaction of spiral waves and pacemakers [182]. (This list of references represents but a few examples of how the FitzHugh-Nagumo model has been used to model cardiac dynamics.) Because I use the FitzHugh-Nagumo model to examine the initiation of spiral waves in chapter 4 of the thesis, I will expand on some of the model's basic properties. The FitzHugh-Nagumo model simulating the

generation of action potentials in a single cell is given as follows:

$$\frac{\mathrm{d}v}{\mathrm{d}t} = \frac{1}{\epsilon} (v - \frac{v^3}{3} - w) + I_p, 
\frac{\mathrm{d}w}{\mathrm{d}t} = \epsilon (v + \beta - \gamma w)$$
(1.1)

where v represents the activation variable—simulating the transmembrane voltage in cardiac cells—w represents the tissue's recovery processes, and  $\epsilon$ ,  $\beta$ ,  $\gamma$ , and  $I_p$  are positive parameters. Because the value of  $\epsilon$  is small and positive, changes in v take place on a faster time scale than changes in w. Given the appropriate parameter values, there exists a unique fixed point, which can be determined by computing the intersection of the v and w nullclines. (The v nullcline is the set of points for which dv/dt = 0, and the w nullcline is the set of points for which dw/dt = 0.) Plotting the nullclines in the phase plane, w as a function of v, shows that the fixed point is where the cubic v nullcline intersects with the linear wnullcline, Fig. 1-1B. For  $I_p = 0$ , the fixed point is stable and small perturbations rapidly return to the fixed point. However, a sufficiently strong perturbation in voltage (that is, an increase in v) across threshold will lead to a solution in the phase plane as shown in Fig. 1–1B. (Panel A in Fig. 1–1 represents the corresponding v time series following the perturbation.) Furthermore, increasing the value of  $I_p$  can induce pacemaker activity, whereby the stable fixed point destabilizes through a Hopf bifurcation, leading to the generation of stable oscillations.

In order to simulate wavefront propagation in a two-dimensional sheet of cardiac tissue, a diffusion term is added to the voltage (v) variable, which gives rise

to a set of reaction-diffusion partial differential equations:

$$\frac{\partial v}{\partial t} = \frac{1}{\epsilon} \left( v - \frac{v^3}{3} - w \right) + I_p + D \left( \frac{\partial^2 v}{\partial x^2} + \frac{\partial^2 v}{\partial y^2} \right) 
\frac{\partial w}{\partial t} = \epsilon \left( v + \beta - \gamma w \right)$$
(1.2)

where D represents the diffusion coefficient of the system. The local cellular dynamics (the reaction terms) related to the generation of the action potential remain the same as in Eq. 1.1, and the intercellular connections are modelled by assuming that voltage spreads via a diffusion process in both the x and y directions. The details associated with numerically computing these equations and some additional features of the model are expanded upon in chapter 4.

Cellular automaton models have also been used to model the dynamics of wavefront propagation in excitable media. A cellular automaton is represented as a grid of cells where each cell has a state that depends on a set of rules based on the states of the surrounding cells. These models are discrete in the sense that at a given time point, each grid point is either active, refractory, or resting. Based on these rules, these systems can model the general properties of excitable media such as excitability and refractoriness. Activity consistent with spiral waves have been observed in cellular automaton models [148]. Wavefront curvature effects have also been introduced into cellular automaton models to capture more of the known properties of wavefront propagation through cardiac tissue [81]. Furthermore, cellular automaton models have been used to study the propagation of wavefronts and the initiation of spiral waves in heterogeneous cardiac tissue [22, 24].

## 1.4 Cardiac arrhythmias

In general, there are three central mechanisms associated with the onset of cardiac arrhythmias: automaticity, triggered activity, and reentry [204]. Abnormal automaticity represents a change in the pacemaking dynamics of the heart, including a change in the rate of the dominant pacemaker (the sinoatrial node) or the emergence of a secondary, ectopic pacemaker [7]. Further, abnormal depolarizations that take place during or following the action potential associated with normal sinus rhythm represents triggered activity, which can precipitate tachyarrhythmias [7].

Reentrant arrhythmias represent a class of abnormal cardiac rhythms for which the dynamics of the heart are not governed by the intrinsic rhythm generated by the heart's pacemaker but rather by a circulating pulse that reenters the same localized tissue region. In order for the reentrant rhythm to entrain the normal rhythm of the heart, the time it takes for the reentrant rhythm to complete one loop of the circuit must be less than the intrinsic period of the heart. In general, reentrant arrhythmias can be split into two classes: anatomic and functional reentry [204].

## 1.4.1 Anatomic reentry

Anatomic reentry represents the unidirectional propagation of a wavefront around an inexcitable region in the heart. A number of inexcitable regions exist in the heart, including the tricuspid valve linking the right atrium and right ventricle, and the four pulmonary veins that deliver oxygenated blood into the left atrium. Inexcitable obstacles can also be generated pathologically. A block in the coronary

blood supply—the circulation system that delivers oxygenated blood to cardiac cells—can lead to ischemia, the reduction of oxygenated blood to regions in the heart, and, consequently, the generation of scar tissue. The scar tissue, termed a myocardial infarction, represents an inexcitable region of tissue, and can act as a substrate for the generation of re-entrant arrhythmias. Myocardial infarctions greatly increase the risk of sudden cardiac death [165].

Ablation therapy represents a surgery that aims to reduce the incidences of reentrant activity underlying a number of arrhythmias, including atrial fibrillation [29], atrial flutter [29], and ventricular tachycardias. The surgery targets inexcitable obstacles, and, in patients with myocardial infarctions, it targets the regions of scar [109]. Understanding the dynamics and the dynamic mechanisms associated with obstacle-induced rhythms represents an important goal from a basic science and clinical perspective.

The dynamics of anatomic reentry have been modelled using a circulating pulse around a one-dimensional ring of cardiac tissue. G.R. Mines first demonstrated that a ring of cardiac tissue could sustain a circulating pulse of excitation [147]. The dynamics of a circulating pulse around a one-dimensional ring of cardiac tissue were examined more carefully by Frame and Simson using tricuspid rings of canine hearts [75]. They found that oscillations in the action potential duration and conduction time preceded the termination of the reentry. To model the dynamics of this process, Courtemanche et al. examined the dynamics of a unidirectional pulse propagating around a one-dimensional ring, and found that the dynamics destabilize at a critical ring length [44, 45]. In particular, once the length

of the ring is critically small, the wavefront runs into its own (partially refractory) wave back, which causes the wavefront to slow down, and, consequently, leads to the onset of the instability. The effects of single and multiple external stimuli on a unidirectionally propagating wavefront in one spatial dimension have also been examined experimentally [93] and theoretically using both partial differential equations and discrete systems [85, 155, 106].

The circulating pulse around the ring simulates macroscopic reentry within the heart, which underlies dangerous tachyarrhythmias. Consequently, methods have been developed to terminate the circulation of the pulse. From a clinical perspective, rapid pacing can terminate anatomic reentry, a method called antitachycardia pacing [193]. Implantable cardioverter defribillators often use antitachycardia-pacing protocols to terminate reentrant arrhythmias detected in patients' hearts [193]. The mechanisms underlying how these pacing protocols terminate reentry are less clear. By stimulating directly on the reentrant circuit, there exist a range of phases, stimulation frequencies, and number of stimuli for which termination of the reentrant circuit takes place [155]. Sinha et al. examined termination of anatomic reentry using stimulation from a site located a specific distance from the circuit [186], discovering that regions of slow conduction are critical for the termination of reentry. A considerable amount of work remains on understanding the details of antitachycardia pacing protocols, and optimizing these protocols to improve success rates.

A coordinated, high-voltage electric shock across the whole heart ('cardioversion') represents another mechanism of terminating reentrant activity [104]. The

high-energy shock can be painful and potentially damaging to the heart [203]. Recent studies have sought to develop new protocols with multiple low-energy shocks [71, 138]. To better understand the mechanism of these new low-energy protocols, modelling studies have used multiple one-dimensional rings to simulate multiple vortices of activity that drive the abnormal dynamics [156].

## 1.4.2 Propagation block

The above studies sought to understand the dynamics and termination properties of a circulating pulse propagating around an inexcitable region. However, what are the mechanisms underlying the initiation of this process? Unidirectional block, where a wavefront can propagate in one direction through a localized region of the tissue but fails to propagate through the same tissue in the opposite direction, represents the central mechanism underlying reentry (both anatomic and functional). Unidirectional block arises as a consequence of spatial inhomogeneity, including differences in the refractory period in a local region of tissue [4] or anatomic nonuniformities [28].

Propagation block can be split into two classes: geometric block and functional block [114]. Geometric block represents a condition within the tissue for which propagation through a region cannot take place. Functional block, in contrast, takes place due to the dynamic properties of the medium, whereby propagation takes place when the tissue has had enough time to recover, but does not take place when the tissue has not had enough time to recover.

Geometric block can take place as a consequence of cellular uncoupling or the introduction of non-conducting heterogeneities into the media [12, 24, 22]. Abrupt

changes in the geometry of the conducting pathway can also induce geometric block. In particular, wavefronts are more susceptible to propagation failure if the conduction pathway suddenly expands in width [28, 23, 64]. A source-sink mismatch—where the amount of tissue that is currently excited by the wavefront (the source) is less than the amount of tissue the wavefront is invading (the sink)—underlies the increased likelihood of propagation failure as a consequence of channel width expansion [65].

Single or multiple stimuli elicited at or near the refractory period of the tissue represents the central mechanism underlying functional block [114]. The heart is composed of tissue with heterogeneous responses to stimuli, including the duration of the action potential, the refractory period, and the local conduction velocity [4]. These differences in the properties of the tissue become clinically relevant as the coupling interval of the stimuli—the time between beats—nears the refractory period, where propagation block can take place locally, leading to the onset of reentry. Structural changes to the heart (following a myocardial infarction, for example) can introduce larger gradients in these properties [129], which can increase the likelihood of functional block. Experimental and computational modelling studies have explored how inexcitable barriers and regions of ionic heterogeneity control these spatial gradients of action potential duration and refractory period, and, consequently, influence the likelihood of functional block [129, 172, 43, 38, 125].

Wavefront curvature represents an additional property that influences the likelihood of functional block. A source-sink mismatch underlies how wavefront

curvature can affect the likelihood of functional block. A convex-shaped wavefront has more sink than source, and, hence, convex wavefronts are more likely to give rise to functional block [65]. Again, structural changes to the tissue structure and rapid expansions of the cardiac conduction pathway induce changes in wavefront curvature, which can also lead to functional block [65, 119].

In chapter 4, we found that changing the position of an inexcitable obstacle in a two-dimensional sheet of cardiac tissue induces changes in the wavefront curvature, which predisposes particular regions of the substrate to functional block and the onset of reentry.

## 1.4.3 Functional reentry

Anatomic reentry represents a wavefront macroscopically propagating around an inexcitable region in the heart. However, reentry can also take place in a sheet of cardiac tissue in the absence of an inexcitable obstacle, a process termed functional reentry. Spiral waves, self-sustaining vortices of electrical activity, represent the pattern thought to underlie functional reentry. Spiral waves have been observed in virtually all types of excitable media, including chemical systems such as the Belousov-Zhabotinsky reaction [210], slime mould [130], and neural systems [121]. Spiral waves have three fundamental properties: period, the rate of rotation; tip trajectory, the macroscopic motion of the spiral wave throughout the media; and chirality, which represents whether the spiral wave rotates clockwise or counterclockwise.

Theory first predicted the existence of spiral waves in cardiac systems. In the 1960s, Krinksy proposed that a wavefront propagating through cardiac tissue interacting with an inexcitable barrier could give rise to a spiral wave, which he called a reverberator [124]. Wiener and Rosenbleuth also predicted the existence of spiral waves propagating about an obstacle [208]. These early studies linked spiral waves with dangerous cardiac arrhythmias. Early experimental studies of the dynamics focused on the Belousov-Zhabotinsky reaction, a chemical reaction that gives rise to spiral waves [210]. In cardiac systems, spiral waves were first observed experimentally in the 1990s [52, 163, 214].

The spiral tip is the point that connects the wavefront, the leading edge of the spiral wave, with the waveback, the end of the refractory period. Exploring the motion of the spiral tip, the tip trajectory, has proved an effective method of exploring the dynamics of how spiral waves propagate through tissue. In particular, the tip trajectory has provided insight into two processes: meander and drift.

Winfree tackled spiral wave meander using the FitzHugh-Nagumo equations in two spatial dimensions [213]. He observed a spectrum of spiral wave behaviour depending on the excitability properties of the tissue, including circular, linear, and outwardly- and inwardly-rotating 'flower petal' tip trajectories [213]. These tip trajectories were also observed in higher-dimensional cardiac ionic models [13], and many of these patterns have been observed experimentally [116].

The tip can also be a useful tool to understand how spiral waves respond to external perturbations that induce spiral wave drift, the directed motion of a spiral wave. Drift can be induced through a number of mechanisms, including resonant drift, where periodic stimulation at precise phases of the spiral wave oscillation can

induce motion [16]; inhomogeneity-induced drift [164]; anisotropy-induced drift [1]; and boundary-induced drift [61].

As stated above, chirality represents whether the spiral wave rotates in a clockwise or counterclockwise direction. Chirality controls the direction of electric-field-induced spiral wave drift in the Belousov-Zhabotinsky reaction [190] and in corresponding numerical simulations [35, 133]. Furthermore, chirality is thought to play a role in the dynamics of atrial flutter, a tachyarrhythmia found in the right atrium, where the direction of circulation waves is typically classified as clockwise or counterclockwise [176]. However, many features of spiral wave chirality remain unexplored. In chapter 4, we find that the position of an inexcitable obstacle with respect to a side pacemaker region determines spiral wave chirality. In the chapter we also explore how spiral wave chirality and the frequency of the side pacemaker are related.

Scroll waves are self-sustaining vortices that propagate in three spatial dimensions, and represent three-dimensional analogs of spiral waves [115]. The scroll filament is composed of the set of points for which the three-dimensional wavefront meets the waveback—tracking the motion of the filament represents a method to examine scroll wave dynamics [6]. Understanding the dynamics of scroll waves is of considerable importance due to the three-dimensional nature of the heart.

Spiral and scroll waves ('rotors') underlie a number of cardiac arrhythmias, including atrial fibrillation, ventricular tachycardia, and ventricular fibrillation.

Atrial fibrillation, an arrhythmia characterized by disorganized electrical activity in

the atria, remains a major cause of mortality and morbidity [29]. Elegant animal models first proposed that rotors could sustain atrial fibrillation [142]. However, recording techniques could not confirm whether these patterns underlied atrial fibrillation in humans. The CONFIRM study first provided evidence that rotors sustain atrial fibrillation in humans [152]. In this study, Narayan et al. identified vortices in patients with atrial fibrillation, and then targeted these rotors for ablation, significantly reducing the recurrence of atrial fibrillation in those patients [152].

Spiral and scroll waves have also been linked to polymorphic and monomorphic ventricular tachycardia [87]. Polymorphic ventricular tachycardia is diagnosed when there is an elevated heart rate and there are beat-to-beat changes in the morphology of the ECG. A rotor undergoing drift through the heart is thought to underlie polymorphic ventricular tachycardia [87, 51]. On the other hand, a rotor that has pinned to an inexcitable obstacle, such as in anatomic reentry, is thought to underlie monomorphic ventricular tachycardia (where the shape of the ECG is constant and the heart rate is elevated). Ikeda et al. proposed that the mechanism underlying the transition from polymorphic to monomorphic ventricular tachycardia is potentially related to the pinning of a drifting spiral wave to an inexcitable obstacle [105]. In patients with a myocardial infarction, the unidirectional propagation of a wavefront through an isthmus of healthy tissue located between regions of scar represents an additional mechanism of monomorphic ventricular tachycardia [192, 191, 109]. Clinicians performing ablation therapy to terminate the onset of these monomorphic tachycardias target these isthmuses of tissue [192, 191, 109].

Again, unidirectional block represents the central mechanism that gives rise to spiral waves. The S1-S2 protocol represents a well-established protocol to initiate spiral waves in the heart [211, 113, 36, 76]. Consider that a plane wave is propagating through a sheet of cardiac tissue from the left edge towards the right edge (the S1 wavefront). A pulse, termed S2, is elicited from a point source in the wake of the S1 wavefront. If the pulse is given directly after the S1 wavefront propagates through the area of stimulation, then the S2 pulse cannot be generated because the tissue is in refractory. In contrast, if the S2 pulse is given a long time after the S1 wavefront has passed, then the S2 wavefront propagates in all directions from the point source. However, when the S2 wavefront is elicited during the vulnerable window, the S2 wavefront is blocked in the rightwards direction, but can propagate in the leftwards direction because that tissue has had more time to recover, which leads to the initiation of a pair of counterrotating spiral waves. The likelihood of reentry also depends on the intensity of the S2 pulse—increased intensity magnitude prolongs the vulnerable window for which a S2 stimulus will induce reentry [211, 113].

Rapid pacing through an inexcitable obstacle can also lead to the detachment of wavefronts from the obstacle leading to the onset of spiral wave activity.

Consider a two-dimensional sheet of cardiac tissue with a side pacemaker region and an inexcitable obstacle. At low side pacing frequencies, the wavefront collides with the obstacle, splits into two wavelets, and these wavelets reconnect behind the obstacle. As the side pacing frequency increases, the wavelets—propagating on either side of the obstacle—destabilize, and detach from the obstacle, which

leads to reentry and the onset of spiral wave activity. This process has been examined in both simplified models of excitation and ionic models of cardiac tissue [159, 215, 17, 141]. Rapid pacing leads to spiral wave initiation through a source-sink mismatch introduced by the inexcitable obstacle, which leads to wavefront-obstacle separation. Starobin and Starmer carefully examined the source-sink mismatch, deriving requirements for wavefront-obstacle separation [188, 189]. Coronary blocks can give rise to ischemia in localized regions of the heart, which can act as triggers for reentry and complex rhythms. Pacing through these slow-conducting regions influences propagation, conduction block, and the onset of reentry [14, 8].

The propagation of wavefronts through heterogeneous tissue, with randomly-distributed non-conducting cells, represents an additional mechanism of spiral wave initiation. Reducing cell-to-cell coupling can lead to reduced conduction velocity, an increased likelihood of propagation block, and greater susceptibility to reentry [24, 25, 181]. As the coupling between cells is reduced, Bub et al. showed that three types of behaviour are observed as a function of the density of non-conducting cells: first, plane waves propagate; second, plane waves break up into spiral waves; and third, plane waves are blocked [24].

In general, sudden cardiac death is caused by ventricular fibrillation, where the electrical activity of the heart is disorganized, and the ventricles cannot give rise to coordinated contractions. Spiral and scroll wave breakup represents a mechanism thought to underlie the transition from tachycardia to fibrillation. Breakup is characterized by the transition from a single rotor to multiple wavelets. Fenton et al. described a number of mechanisms that lead to spiral and scroll wave breakup, which include steep action potential duration restitution curves in the tissue, bistability, and super-normal conduction [68].

In chapter 4, we explore the onset of spiral waves using simplified experimental and theoretical models. In particular, I examine how the position of an inexcitable region in combination with pacemaker frequency determine spiral wave chirality. Many studies have examined precursors preceding the onset of spiral wave initiation. Alternating rhythms have been shown to precede the onset of spiral wave activity [30, 160]. In particular, alternating rhythms increase the likelihood of propagation block, which can lead to the initiation of reentry—I examine the details associated with the onset of alternating rhythms in the section below.

#### 1.4.4 Alternans

Alternating rhythms, also termed alternans, represent beat-to-beat variations in the heart's dynamics. First reported over 100 years ago [80, 147], alternating rhythms are one of several different precursors that can precede the onset of dangerous reentrant arrhythmias. Recent clinical studies also suggest a possible link between alternating rhythms and the likelihood of sudden cardiac death [187, 171].

Beat-to-beat alternations in the response of the action potential underlie alternating rhythms. Periodic stimulation can induce alternating rhythms in cardiac systems. As the pacing frequency nears the refractory period of the tissue, a transition from a 1:1 rhythm, where for every stimulus there is a single, stable response, to a 2:2 rhythm, where for every two stimuli, there are two different

types of responses (i.e. an alternation between long and short action potential durations), takes place. Nolasco and Dahlen studied alternating rhythms induced by periodic stimulation of ventricular cardiac tissue from frogs using a graphical method, where they plotted curves that displayed the duration of the action potential as a function of the diastolic interval, the amount of time the tissue had to recover [154]. Using these curves—termed action potential duration restitution curves—they found that the slope of the curve could predict the onset of the alternans.

Guevara et al. rediscovered these properties nearly 20 years later, analyzing the features of the slope prediction using experimental data from the periodic stimulation of embryonic chick cardiac cells, and the stability of fixed points in one-dimensional maps [91]. To analyze the stability, standard techniques can be used, which I describe briefly.

A one-dimensional map represents a dynamical system for which the dynamics of the system are controlled simply by the functional relationship relating the value at the following iteration with the value at the current iteration. The stability analysis of fixed points in one-dimensional maps represents a method of evaluating the dynamics of these systems. For a one-dimensional map,  $x_{n+1} = g(x_n)$ , there exists a fixed point,  $x^*$ , where  $g(x_n)$  intersects with the function  $x_{n+1} = x_n$ . In particular, a fixed point represents a point from the function for which the value at the following iteration is the same as the value at the current iteration.

A fixed point can be stable or unstable. In the neighbourhood of a stable fixed point, subsequent iterations will approach the value of the fixed point;

near an unstable fixed point, subsequent iterations will be repelled by the fixed point. To analyze the stability of fixed points in nonlinear one-dimensional maps, linearization techniques are used to evaluate the dynamics.

For nonlinear one-dimensional maps, the curve in the neighbourhood of the fixed point can be approximated as a straight line. The slope through the fixed point determines the dynamics of fixed points in linear one-dimensional maps. This analysis extends to the stability of fixed points in nonlinear systems, where we designate the slope at the fixed point as  $\alpha = g'(x^*)$ . If  $|\alpha| > 1$ , the fixed point is unstable; in contrast, if  $|\alpha| < 1$ , the fixed point is stable, and, for initial conditions in the neighbourhood of the fixed point, subsequent iterates will approach  $x^*$ .

Changing the value of a control parameter can change the value of  $\alpha$  through  $\pm 1$ . For one-dimensional maps, the system will undergo a saddle-node bifurcation when  $\alpha = 1$ , where the fixed point disappears. Or, in contrast, the system goes through a period-doubling bifurcation when  $\alpha = -1$ , where a transition from a stable fixed point to a period-2 cycle takes place. More complex bifurcations, such as torus bifurcations, can take place for higher-dimensional maps.

To understand how one-dimensional maps can be used to understand the onset of alternating rhythms in the heart, I first assume that the duration of the next action potential is a function of the amount of time the cell has had to recover [91]:

$$A^{n+1} = f(t_r^n) \tag{1.3}$$

I also assume that the pacing period (the inverse of the pacing frequency) is the sum of the current action potential duration and the current recovery time:

$$T_p = A^n + t_r^n (1.4)$$

We can determine the functional relationship,  $f(t_r^n)$ , by changing the pacing frequency, thereby changing the amount of time the cell has to recover. These restitution relationships can typically be fitted using an exponential function, where at long  $t_r$ , the action potential duration plateaus, and as  $t_r$  is lowered, the action potential duration curve decreases. By rearranging Eq. 1.4 and inserting this relationship into Eq. 1.3, we derive a one-dimensional map as follows:

$$A^{n+1} = f(T_p - A^n) (1.5)$$

where there, in general, exists a unique fixed point. For Eq. 1.5, the slope at the fixed point is governed by  $T_p$ , the pacing period. As  $T_p$  decreases, the slope at the fixed point approaches and goes through -1, which gives rise to a period-doubling bifurcation, establishing a stable period-2 limit cycle that oscillates between a longer action potential duration and a shorter action potential duration.

The mechanistic details, however, associated with how alternating rhythms influence the dynamics of the 3-dimensional heart are less clear. T-wave alternans represents a cardiac arrhythmia characterized by a beat-to-beat alternation in the morphology of the ECG, which has been linked to the genesis of fibrillation [160]. Improved signal processing techniques can now detect microvolt alternations in the T-wave of the ECG, which represents a possible indicator of the risk of sudden

cardiac death [202, 201]. However, the effectiveness of T-wave alternans as an indicator remains unclear as there have been studies that have shown that it does not predict increased likelihood of sudden cardiac death [40].

A beat-to-beat alternation in the ECG could arise through a couple of mechanisms. First, an alternation in the duration of the action potential duration—consistent with dynamic mechanism given above by Guevara et al. [91]—could give rise to the T-wave alternans [160]. Second, localized conduction block on every other beat could decrease the amount of tissue contracting, which would also give rise to T-wave alternans. Gaskell first reported this class of alternans [80], and the dynamics have been described numerically [8] and experimentally [69].

Periodic stimulation of a sheet of cardiac tissue can lead to the emergence of different spatial alternating patterns: concordant or discordant alternans. Spatially concordant alternans take place when the entire tissue is alternating between long to short beats in phase. In contrast, spatially discordant alternans take place when localized tissue regions are alternating between long and short beats, and other regions are alternating between short and long beats. Both spatially concordant and discordant alternans can be initiated in homogeneous sheets of tissue [160, 206]. Traditionally, studies showed that a transition from normal sinus rhythm to concordant alternans to discordant alternans would take place as a function of increasing pacing frequency. However, Gizzi et al. showed that more complicated transitions between concordant and discordant alternans can emerge as a function of pacing period [82]. Recent studies have also explored how

inexcitable barriers can increase the susceptibility of cardiac tissue to the onset of alternans [161, 125].

If alternating rhythms represent a precursor to the onset of fibrillatory activity, what is the mechanism through which this takes place? There is a delicate interplay between the duration of the action potential, the refractory period, and the conduction velocity of propagating wavefronts in the heart. However, in general, wavefronts with short action potential durations are more susceptible to propagation failure. Pastore et al. proposed a mechanism, using optical mapping data of rapidly paced guinea pig heart, whereby the wavefront with a short action potential duration runs into the refractory tail of the wavefront with the longer action potential duration, which gives rise to local unidirectional block, and, hence, the initiation of reentrant activity [160].

A steep action potential duration restitution curve, associated with the onset of alternans, underlies one of the mechanisms of spiral wave breakup leading to the onset of fibrillatory behaviour [111, 112, 68]. Spiral waves rapidly pace the tissue, which can give rise to alternans in the duration of the action potential. If the oscillations in the action potential duration are of sufficiently large amplitude, the wavefront associated with the short action potential duration can run into the refractory tail of the longer wavefront, giving rise to local conduction block, which can lead to the initiation of reentrant activity. As described above, alternans are associated with steep action potential duration restitution curves. Thus, studies have sought to flatten the restitution curve of the tissue using pharmacological means, reducing the susceptibility of the heart to fibrillatory activity [168, 78].

Alternating rhythms represent precursors to reentrant cardiac rhythms. In chapter 3, we predict the onset of alternating rhythms through period-doubling bifurcations using one-dimensional map theory. In chapter 4, we use action potential duration restitution curves computed throughout the substrate to make predictions about the pacing frequency at which specific regions of the substrate will destabilize, giving rise to spiral wave initiation.

## 1.5 Predicting the onset of abnormal cardiac rhythms

Biological, physical, and social systems often display qualitative changes in dynamics. Developing early warning signals to predict the onset of transitions in complex systems remains a challenging problem, and is relevant in diverse contexts [180], including climate change [50, 131], ecology [143, 31], population dynamics [47, 46, 48], physiology [145, 123], and finance [144].

Instabilities in the dynamics of cardiac systems can represent precursors for the onset of potentially dangerous cardiac rhythms. Above, I discuss how alternating rhythms, which can arise as a consequence of a period-doubling bifurcation, can precede the onset of abnormal reentrant arrhythmias [160]. Therefore, the development of early warning signals that herald the onset of these instabilities represents a potentially useful therapeutic goal for the prevention of cardiac arrhythmias.

Transitions in the dynamics of complex systems can take place through a number of mechanisms. These transitions can be linked to bifurcations, whereby a change in the value of a model parameter leads to qualitative differences in the dynamics of the system. For a number of bifurcations, as a parameter value

approaches a bifurcation point, there is a slower return to equilibrium following perturbations, a property called slowing down, which can be targeted to develop early warning signals of these transitions [180, 126, 31, 47, 50, 49]. Slowing down takes place in the neighbourhood of period-doubling bifurcations [209, 94], a property that I use to analyze the period-doubling bifurcations in chapter 3.

A number of studies have focused on developing early warning signals of saddle-node bifurcations, where, at a critical parameter value, there is a transition in the value of the system's steady-state value [180, 49]. These transitions can be characterized by tipping points, which represent the threshold that the system crosses leading to the establishment of a new steady-state value [83]. In the 1970s, May used the saddle-node bifurcation to simulate collapses in models of vegetation biomass as a function of the number of herbivores [143]. Models developed by researchers working on catastrophe theory also simulated rapid and abrupt changes in steady states using saddle-node bifurcations [218].

Contemporary work on abrupt transitions as a consequence of saddle-node bifurcations (mostly in continuous-time contexts) have focused on two early warning signals: an amplification of the noise and an increase in the system's memory. The eigenvalue associated with the stable steady-state governs how rapidly equilibrium is reestablished following perturbations. As the system nears the saddle-node bifurcation, the magnitude of the real part of the eigenvalue approaches zero, reducing the system's rate of recovery back to equilibrium. Consequently, both the noise and memory increase as the system nears the transition. To quantify changes in the system's memory, these studies report an

increase in the autocorrelation in the neighbourhood of the transition [180, 126, 31, 47, 50, 49]. Another phenomenon that can predict the oncoming saddle-node bifurcation is flickering, where the system flips back and forth between two stable steady states near a critical parameter value [205].

These early warning signals can predict transitions in systems that undergo saddle-node bifurcations as a consequence of a slowly-varying parameter. However, transitions in physical, chemical, and biological systems take place through a number of bifurcations with varying properties near the onset of these bifurcations. Predicting the onset of noise-induced transitions is difficult because the underlying properties of the system have not changed, but rather a chance event (typically a large excursion from the steady-state value) leads to a transition in the dynamics [131, 56]. Additionally, transitions in dynamics take place through a number of bifurcations. Noisy precursors have been reported for other bifurcations, including pitchfork, hopf, and period-doubling bifurcations, in terms of changes in the power spectra in the neighbourhood of the transitions [209].

In chapter 3, potassium channel blockade leads to the onset of alternating rhythms through period-doubling bifurcations in aggregates of spontaneously beating cardiac cells. The transition takes place over a long time scale—on the order of tens of minutes. I analyze these bifurcations and develop a quantitative measure that can predict the onset of the period-doubling bifurcations.

Alternating rhythms can evolve into more complicated rhythms. In fact, sequences of period-doubling bifurcations are associated with the onset of chaotic dynamics.

## 1.6 Period-doubling route to chaos

Period-doubling bifurcations can underlie the transition from a normal cardiac rhythm to an alternating rhythm as the value of a control parameter goes through a critical point [91]. A sequence of period-doubling bifurcations can also lead to the generation of chaotic dynamics. Chaotic dynamics have been reported in simplified cardiac systems [88, 79]. Cardiac fibrillation was perhaps thought to be driven by spatiotemporal chaos, but it does not appear that this dynamic mechanism underlies fibrillatory behaviour in the heart.

Chaotic dynamics are aperiodic, sensitive to initial conditions, bounded, and deterministic. A question arises, however: if all biological systems contain noise, then how can one suggest that a biological system (such as the heart) gives rise to chaotic dynamics. Glass proposed that chaotic dynamics observed in experimental systems could be considered 'chaotic' if the dynamics of the experimental system follow bifurcations that are consistent with a transition to chaos observed in theoretical models [84].

In chapter 2, we find that potassium channel blockade can give rise to highly irregular rhythms in spontaneously beating aggregates of cardiac cells. Analyzing these rhythms using low-dimensional maps demonstrates that these rhythms are, in fact, chaotic and take place through a sequence of period-doubling bifurcations.

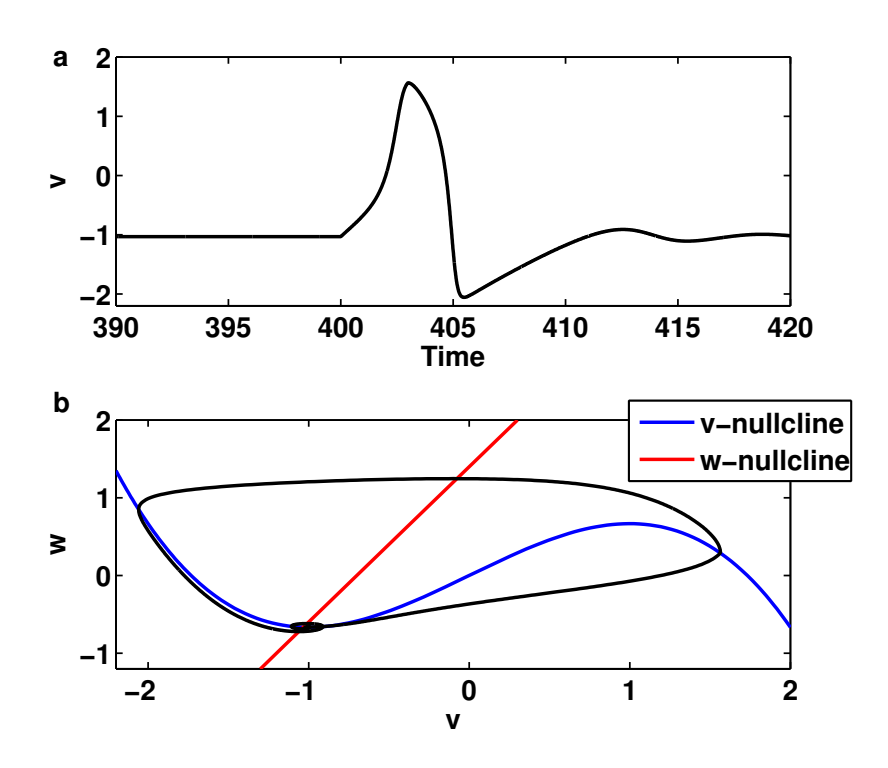


Figure 1–1: Sample solution and phase plane for the FitzHugh-Nagumo model (A) Representative voltage trace in response to a perturbation. (B) FitzHugh-Nagumo model phase plane. The v-nullcline is cubic (in blue) and the w-nullcline is linear (in red). The fixed point of the system is where the nullclines intersect. The black line represents the trajectory of the system in response to a perturbation.

#### CHAPTER 2

## Chaotic cardiac dynamics induced by potassium channel block

## 2.1 Foreword

Nonlinear systems often show sequences of changes in dynamics as key parameters continuously change. In one type of transition, termed a period-doubling bifurcation, the period of an oscillator doubles as a parameter passes through a critical value. Sequences of period-doubling bifurcations can lead to the onset of chaotic dynamics. Chaotic rhythms are aperiodic, deterministic, sensitive to initial conditions, and bounded. Examples of chaotic dynamics have been observed in a number of biological [88, 3], chemical [185], and physical [135] systems.

This thesis focuses on instabilities of the cardiac rhythm—both because of its fundamental importance for human health as well as the clear connections to nonlinear dynamics. Attention has also focused on the effects of mutations and drugs on the hERG potassium channel that mediates the delayed potassium  $I_{Kr}$  current [174]. Instabilities in cardiac activity associated with the lengthening of action potential duration as a consequence of mutations or drugs represents an additional important cause of cardiac arrhythmia [169, 173, 9, 72, 175, 132, 179, 178]. Experimental modification of the  $I_{Kr}$  is carried out by treatment with E4031, a drug that specifically blocks the hERG potassium channel [184, 183, 174, 42]. Since ion flow through potassium channels leads to repolarization, blocking  $I_{Kr}$ 

leads to a prolongation of the action potential duration. In related work, a variety of complex rhythms have been observed from potassium channel blockade in experimental and theoretical studies of neural systems [102, 33, 63, 34].

In early unpublished experimental studies carried out in our laboratory, we observed complicated sequences of interbeat intervals (IBIs) following treatment of E4031 to spontaneously beating aggregates of embryonic atrial heart cells, Fig. 2–1. Subsequently, a new set of studies on the effects of E4031 on cardiac cells was initiated [117]. To carry out recordings over a longer time window, we adopted optical methods to record the motion of heart cell aggregates. The study reported complex bursting rhythms, and developed a Hodgkin-Huxley-style ionic model that was capable of generating similar dynamics to those experimentally observed [117]. Although in our earlier work we noted that chaotic dynamics could be present, we did not give experimental or theoretical models that displayed chaos.

In this chapter, I focus on the chaotic dynamics observed in embryonic chick aggregates following E4031 treatment. First, I present the experimental methods, and then consider two examples of chaotic rhythms from the experimental data, analyzing the dynamics using one-dimensional maps. I also describe the dynamics and bifurcations of the Hodgkin-Huxley-style ionic model as a function of potassium channel blocker concentration.

## 2.2 Experimental methods

## 2.2.1 Tissue preparation

Either atrial or ventricular tissue were prepared according to the DeHaan method [53, 127]. The intracellular recordings performed in the early 1990s were

conducted with atrial aggregates. The optical recordings were carried out on ventricular aggregates, including data from 93 aggregates described earlier [117] and 11 subsequent experiments. The atria or ventricles of seven-day-old White Leghorn chick embryo hearts were dissected and dissociated into single cells by trypsinization. The cells were added to an Erlenmeyer flask containing a culture medium gassed with five per cent  $CO_2$ , 10 per cent  $O_2$ , 85 per cent  $N_2$  (pH=7.4), and placed on a gyratory shaker for 24-48 hours at 37° C. The aggregates had a diameter of approximately 100-300  $\mu$ m. In this environment, the aggregates beat with an intrinsic frequency in the range of 700-2000 msec. The experiments were conducted two to six hours after the aggregates were plated on the tissue culture.

The  $I_{Kr}$  channel blocker E4031 (Alomone Labs, Jerusalem) was added at various concentrations in the range of 0.5–2.5 $\mu$ M.

## 2.2.2 Intracellular recordings

Intracellular recordings were carried out as described previously [127] on atrial preparations. Briefly, electrical activity was recorded using microelectrodes filled with 3 M KCl solution (typical microelectrode resistance was 40-60 M $\Omega$ ). Transmembrane potential was recorded, using an amplifier with negative capacitance compensation. The bathing medium was kept at virtual ground by coupling to a current-to-voltage converter (10-100 mV/nA) through an agar-salt bridge and a chlorided silver wire.

## 2.2.3 Optical imaging technique

We used an optical imaging apparatus that monitored the aggregates' motion. The device recorded the light-intensity variation of a specific pixel on the edge of an aggregate. The edge pixel data was then processed through a bandpass filter (cutoff frequencies: 0.1Hz-6.5Hz). Using Matlab, we identified the beats and computed the time interval between consecutive beats. The system employed phase-contrast imaging sampled at 40 Hz and a CCD camera (RedShirtImaging, LLC, NeuroCD-SM) at an  $80 \times 80$  pixel spatial resolution. Recordings were carried out at  $35-37^{\circ}$  C.

## 2.3 Results

## 2.3.1 Intracellular recordings

The transmembrane voltage was recorded following the application of E4031.

The complex dynamics observed following E4031 application of atrial aggregates merely provided motivation for further study. However, since the optical recordings reflect the motion of the aggregates and the electrical recordings reflect the transmembrane voltage, the two sets of experiments complement each other.

Figure 2–1 displays two examples of recorded activity. Panel A shows irregular dynamics in which there are variable IBIs. This type of variability suggests the possibility of underlying chaotic dynamics. However, the recording was not sufficiently long to carry out a detailed analysis. (This intracellular recording is similar to the work that will be presented in Fig. 2–3.) Panel B from Fig. 2–1 shows a transition from a regular rhythm of doublets to a rhythm with bursts of activity and doublets. This trace is similar to the bursting rhythms described earlier [117].

## 2.3.2 Optical recording examples

The transition times following E4031 application display a great deal of variability, even for aggregates in the same culture dish subjected to the same preparation procedure. Following E4031 application, the aggregates' intrinsic beat frequency was maintained for variable lengths of time—between 10 and 40 minutes. Following this periodic activity there were qualitative changes in the dynamics that depended on E4031 concentration. In general, when we applied between 0.0 to 0.9  $\mu$ mol E4031 to the dish, the aggregate's intrinsic frequency was maintained throughout the experiment. When more than 2.5  $\mu$ mol was applied, the IBIs became increasingly shorter, settling at a stable accelerated rate. Between 1.0  $\mu$ mol and 2.0  $\mu$ mol, though, complex dynamics tended to emerge. An alternation between long and short intervals (doublets) was observed in 71/104 aggregates. In 21/104 aggregates, there were added beat rhythms with occasional doublets. Bursting patterns were observed in 45/104 aggregates. In 9/104 aggregates, chaotic dynamics were observed. In this paper we focus on the dynamics that appear to be chaotic.

Figures 2–2 and 2–3 display examples of highly irregular rhythms. Panel A of these figures give the IBIs over the course of the experiments, as well as traces displaying typical time series of activity. Panel B of Figs. 2–2 and 2–3 show return maps in which each IBI is plotted as a function of the preceding IBI at a few times throughout the experiments. The data in both figures share the common feature that the initial regular oscillations undergo bifurcations to more complex rhythms. A striking feature of the diagrams is that the data in panel A of both Figs. 2–2

and 2–3 resemble the common bifurcation diagrams showing the iterates of a function as a parameter is changed. In the current case, the changing parameter is either associated with changing concentrations of drug as a result of diffusion, or changing physiology secondary to the presence of the drug. Independent of the particular mechanism, the changes take place over a time scale of tens of minutes.

The return maps displayed in panels B of Figs. 2–2 and 2–3 share some common features and also show some striking differences. For both examples, the dynamics appear to evolve over the course of the experiment. Further, the irregular activity shown in the time series is consistent with a one-dimensional map with a single extremal point. However, for the data in Fig. 2–2 the extremal point is a maximum, whereas in Fig. 2–3 it is a minimum. Data similar to that displayed in Fig. 2–2 was found in four preparations, whereas data similar to that displayed in Fig. 2–3 was found in five preparations. Since these one-dimensional maps are similar to one-dimensional maps with quadratic extrema that display chaotic dynamics, we attribute the observed complex dynamics to deterministic chaos. For short, noisy data such as we have here, we believe that well-defined one-dimensional return maps consistent with chaos provide a better method for identifying chaos than other criteria such as the Lyapunov exponent [84].

We do not understand the origin of the differences between the two preparations. Although the concentrations of E4031 were somewhat different, we also found patterns similar to those in Fig. 2–2 at 1.0  $\mu$ mol and 1.5  $\mu$ mol, and similar to those in Fig. 2–3 at 2.0  $\mu$ mol. However, the five preparations similar to those shown in Fig. 2–3 were done by one investigator, whereas the four preparations

similar to experiments shown in Fig. 2–2 were done by a second investigator about two years following the initial experiments.

Despite these discrepancies, we believe that it is useful to develop simple phenomenological models of the data using one-dimensional maps with adjustable parameters, as well as ionic models.

## 2.3.3 Phenomenological model

The data presented in Fig. 2–2 appears similar to data that could be generated using a one-dimensional map with stochastic terms, as a parameter changes leading to bifurcations. To develop a phenomenological model for the experiments we used an analytic function to fit the final chaotic return map, and then translated the fitted map to generate bifurcations.

For the first example displayed in Fig. 2–2, we used the following equation:

$$x_{n+1} = \alpha(x_n - \beta)e^{-\gamma(x_n - \beta)} - \delta(x_n - \beta) + \tau$$
 (2.1)

where  $x_n$  represents the nth IBI, and  $\alpha, \beta, \gamma, \delta$ , and  $\tau$  are all positive parameters. We selected the function's parameters—which are phenomenological in nature—based on which values could most closely reproduce the experimental data. Panel B of Fig. 2–2 displays the one-dimensional return maps—which maps the IBI at time t with the IBI at time t + 1—of the IBIs at four particular time points throughout the experiment. The value of parameter  $\tau$  is different for each time point;  $\tau$  continuously decreases throughout the course of the experiment, giving rise to the complex transitions.

A sequence of period-doubling bifurcations gives rise to the experimentally observed chaotic dynamics. A transition from period-1 to period-2 takes place between 10 to 13 minutes following E4031 application, as the upper and the lower branches of the IBIs split apart. The system oscillates in the period-2 experimental parameter regime for approximately 10 to 15 minutes before another period-doubling bifurcation occurs. Following this transition, however, the system's intrinsic noise covers the underlying period-4 beat pattern, and it is difficult to delineate the branches. The onset of chaotic dynamics appears to take place at around t=37 minutes and lasts until the end of the recording.

We fit the analytic function given by Eq. 2.1 to the experimentally generated chaotic return map. We constructed the chaotic map with IBIs from t=37 minutes until the end of the recording. The analytic function displayed the same sequence of period-doubling bifurcations, providing strong evidence that the seemingly irregular activity between t=37 minutes and the end of the record is consistent with deterministic chaos. We decreased the parameter  $\tau$ , which translated the function vertically, to display the sequence of transitions (from period-1 to period-2 and so on). Using the listed values of parameters and within the given range of  $\tau$ , Eq. 2.1 has two fixed points:  $x_1^*$  and  $x_2^*$ .  $x_1^*$  is always unstable because the slope of the function through the line  $x_{n+1} = x_n$  is always much greater than 1.  $x_2^*$ , however, gives rise to a set of period-doubling bifurcations as  $\tau$  is lowered.

For approximately  $\tau > 0.713$ ,  $x_2^*$  is stable, destabilizing when  $\tau < 0.713$  because the slope of the function through the line  $x_{n+1} = x_n$  at the fixed point goes from greater than -1 to less than -1. (Recall that the criterion for stability

of a fixed point of a one-dimensional map is given by  $\left|\frac{d_{xn+1}}{d_{x_n}}\right|_{x_n=x^*} < 1$ , where  $x^*$  is a fixed point.) Once  $x_2^*$  destabilizes, a cycle of period-2 emerges. A cycle of period-4 emerges as  $\tau$  is further reduced. Again this is consistent with the experimental observations' dynamical structure.

For the second chaotic example, displayed in part A of Fig. 2–3, we used the following equation:

$$x_{n+1} = \alpha(x_n - \beta)e^{\gamma(x_n - \beta)} + \tau \tag{2.2}$$

where  $x_n$  represents the IBIs, and  $\alpha, \beta, \gamma$ , and  $\tau$  are all positive parameters. Panel B of Fig. 2–3 displays the associated one-dimensional return maps at three time points throughout the experiment. For this example, the bifurcation parameter  $\beta$ , which controls the horizontal position of the fitted return map, is continuously decreased, horizontally translating the map. A sequence of period-doubling bifurcations gives rise to the chaotic dynamics, which is qualitatively similar to the experimental data. Panel A of Fig. 2–4 displays Eq. 2.1's bifurcation structure as a function of  $\tau$ . Likewise, panel B of Fig. 2–4 represents Eq. 2.2's bifurcation structure as a function of  $\beta$ . These bifurcation diagrams display in more detail the cascade of period-doubling bifurcations leading to chaotic dynamics.

## 2.3.4 Hodgkin-Huxley ionic model

We assembled a single-cell cardiac ionic model to numerically simulate the effects of adding drug to a spontaneously beating chick cell aggregate. The model adapts the equations given by Kowtha et al., [122] and has seven discrete ionic currents and ten dynamic variables. Kim et al. [117] initially presented this model; however, for this study, we used a different set of parameter values. The differences

in the parameter values and a full explanation of the model are described in Appendix A at the end of the thesis.

A forward Euler numerical scheme was employed with a step-size of  $\Delta t = 0.00005$  seconds. The model states that  $\dot{V} = -I_{tot}(V)/C_i$ , where V is the total membrane current,  $I_{tot}$  is the total membrane current, and  $C_i$  is the input capacitance. The model also assumed that  $I_{tot} = I_{Na} + I_{Ks} + I_{Kr} + I_{K1} + I_{Ca} + I_b + I_f$ , where  $I_{Na}$  is the inward sodium current,  $I_{Ks}$  is the slowly activating potassium current,  $I_{Kr}$  is the rapidly activating delayed rectifier potassium current,  $I_{K1}$  is the inward rectifier potassium channel,  $I_{Ca}$  is the inward calcium current,  $I_b$  is the time-independent background current, and  $I_f$  is the hyperpolarization-activated pacemaker current. The specific parameters and equations are included in Appendix A.

Figure 2–5 displays the ionic model's numerical results. We studied the effects of changing  $I_{Kr}$  conductance,  $g_{Kr}$ , which represents the number of potassium channels available to mediate  $I_{Kr}$ . In an experimental context,  $g_{Kr}$  decreases as E4031 concentration increases. The model reproduces dynamics and transitions similar to those observed experimentally. We observe singlets (single cycle length) for high  $g_{Kr}$  values. As  $g_{Kr}$  decreases, the action potential duration increases as a consequence of reduced inwardly rectifying current. At a critical  $g_{Kr}$  value, a period-doubling bifurcation takes place, giving rise to a doublet pattern. The bifurcation takes place rapidly in  $g_{Kr}$  parameter space. Another period-doubling bifurcation—from period-2 to period-4—takes place as  $g_{Kr}$  is further decreased. We observe dynamics consistent with chaos at approximately  $g_{Kr} = 12$ . Reverse

period-doubling bifurcations shift the system out of the chaotic regime, establishing another stable, accelerated limit cycle at low  $g_{Kr}$  values.

The numerically computed chaotic parameter regime was studied in more detail. We reduced a time series with a  $g_{Kr} = 11.898$  to a one-dimensional return map by computing the IBIs, and plotting each IBI as a function of the preceding value. The one-dimensional return map displays qualitatively similar characteristics to the experimental chaotic example shown in Fig. 2–2. For the simulation in Fig. 2–5C, we estimated the Lyapunov exponent of the IBI return map by estimating the slope of the fitted map at each point. The Lyapunov exponent (the logarithm of product of the absolute values of the slopes) was positive, consistent with chaotic dynamics in the ionic model.

## 2.4 Discussion

Following the addition of E4031, a drug that blocks potassium channels, a variety of complex rhythms are observed in spontaneously beating embryonic chick heart cells, including alternating rhythms, bursting rhythms, and irregular rhythms. In some preparations, a return map, in which the interbeat interval (IBI) is plotted as a function of the preceding IBI, falls on a one-dimensional function that generates chaotic dynamics, lending support to the identification of chaotic dynamics. Further, we propose an ionic model that reproduces many of the characteristic dynamical regimes as a function of decreasing potassium channel conductance: alternans, bursting dynamics, period-doubling bifurcations, chaotic dynamics, and a stable, accelerated rhythm regime.

In the past there have been a large number of experimental and theoretical studies analyzing the effects of ionic channel blockade and modification in nerve and heart cells. Following pioneering studies on the effects of potassium channel blockade on a molluscan neuron by Holden et al. [102], Chay and colleagues demonstrated a variety of complex rhythms in simplified ionic models of nerve cells as potassium current was reduced [33, 63, 34]. More recently, there have been extensive studies on the dynamical effects of extracellular calcium on a neural pacemaker generating chaotic interspike interval return maps that are similar to Fig. 2–2 [136, 108]. The above papers refer to dynamical systems that are well described by ordinary differential equations. Extending this work to spatially distributed cardiac systems that are best described by partial differential equations, manipulation of ionic channel properties can lead to the induction of complex reentrant rhythms similar to those believed to underlie serious cardiac arrhythmias [9, 216, 128, 26]. This body of work makes clear that even though neural and cardiac oscillations must necessarily be robust to environmental perturbations, there is nevertheless a delicate interplay of ionic conductances. Disturbing the relative contributions of different channels can lead to degeneration of dynamics yielding rhythms similar to those generated by well-known bifurcations in nonlinear dynamics.

Our experimental technique allows for the simultaneous monitoring of multiple aggregates subject to the same experimental manipulations over long times. We measured the aggregates' beat activity by collecting the light intensity from a pixel on the edge of a particular aggregate and detecting the changes of the light

intensity—a jump in the light intensity was considered to be a contraction and a consequence of an action potential. We selected this method over intracellular measurement or dye application because the drug's effect over the aggregate's dynamics took place over the course of tens of minutes, and other methods of data collection are difficult to sustain over such long time periods. Since parameters are continuously changing, this method generates bifurcation diagrams, e.g. see Figs. 2–2 and 2–3, similar to classic bifurcation diagrams that depict dynamics in theoretical models as a function of a parameter. Thus, the addition of drugs to excitable biological systems enables direct experimental observation of bifurcation diagrams. This procedure could be useful for the screening of drugs for proarrhythmic effects. From a nonlinear dynamical perspective, the method could be exploited to analyze questions of robustness of dynamics and bifurcations as a function of physiological differences between different aggregates.

From a medical perspective, the initiation of complex arrhythmia as a consequence of modifying ionic channel activity represents a major impediment and problem for the development of new drugs [72, 175]. The current work points to the difficult mathematical problems that will need to be solved in order to understand the complex dynamics induced by drugs that modify potassium channels conductance in heart cells.

In this chapter, I showed that sequences of period-doubling bifurcations in the dynamics of aggregates of embryonic chick cardiac cells can lead to the initiation of chaotic dynamics. Potassium channel blockade can also lead to the onset of alternating rhythms through a period-doubling bifurcation. Alternating rhythms

in the spatially-extended context of the heart can precede the onset of serious reentrant arrhythmias. In chapter 3, I develop early warning signals to predict the onset of alternating rhythms based on data collected from spontaneously beating aggregates of cardiac cells following potassium channel block.

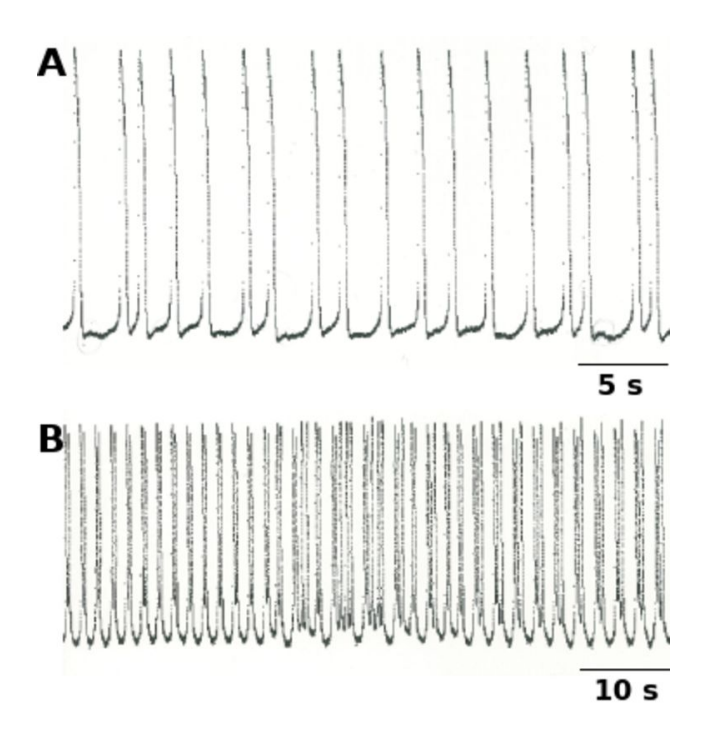


Figure 2–1: Intracellular transmembrane voltage recording of a spontaneously beating atrial aggregate following E4031 application. (A) Representative chaotic example. (B) Transition from doublet beat pattern to more complex bursting behavior. The transition takes place at roughly t=25 seconds.

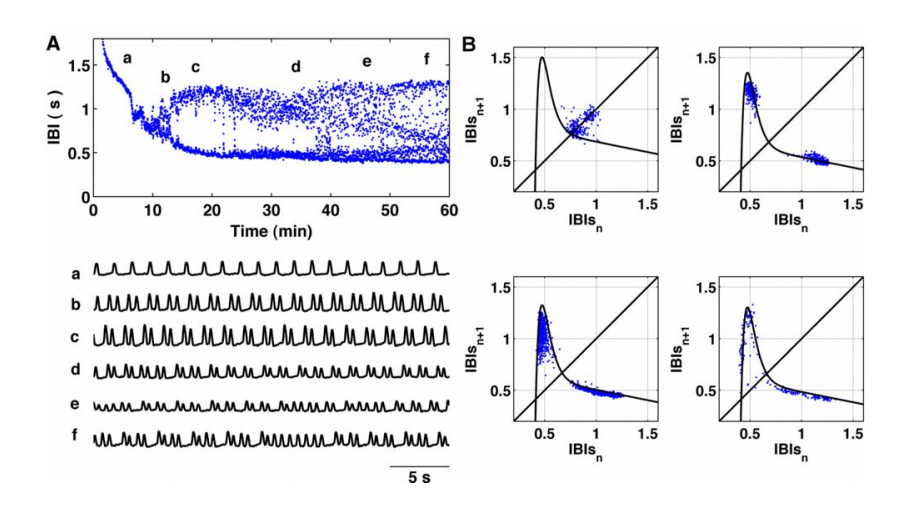


Figure 2–2: Chaotic dynamics in spontaneously beating aggregate of cardiac cells following the application of 1.5  $\mu$ mol E4031. (A) Experimental observations of the motion of a ventricular aggregate. This experiment was performed by the second investigator in the set of follow-up experiments to the initial study [117]. The drug is applied at time t=0 minutes. The aggregate maintains its intrinsic frequency for roughly 15 minutes before the initial bifurcation takes place as the E4031 diffuses throughout the dish. (a) Aggregate's intrinsic beat frequency. (b-d) Doublet pattern generated through a period-doubling bifurcation. (e-f) Chaotic dynamics. (B) The IBIs are plotted as a function of the preceding IBI and a phenomenological one-dimensional map is fitted to the beats as the dynamics evolve. Equation 2.1 governs the fitted map's shape. The function has five parameters:  $\alpha$ =35,  $\beta$ =0.42,  $\gamma$ =18,  $\delta$ =0.2, and  $\tau$ , which is the bifurcation parameter.  $\tau$  vertically translates the function, so  $\tau$  continuously decreases throughout the course of the experiment.

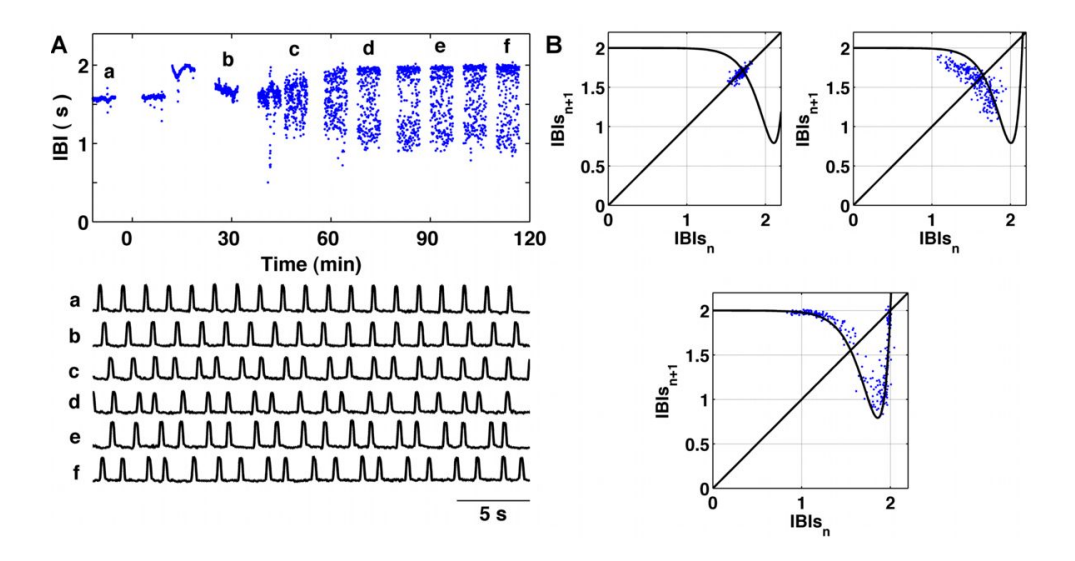


Figure 2–3: Chaotic dynamics in cardiac aggregate following the application of 2.0  $\mu$ mol E4031. (A) Experimental observations of the motion of a ventricular aggregate. The first investigator performed this experiment. The initial bifurcation takes place at approximately t=40 minutes. (a-b) Singlets. (c-f) Irregular chaotic dynamics. (B) One-dimensional return maps of the IBIs from experimental data described in panel A. The function is described by Eq. 2.2. The function has four parameters:  $\alpha$ =23,  $\gamma$ =7,  $\tau$ =2, and  $\beta$ , which is the bifurcation parameter.  $\beta$  horizontally translates the function, so  $\beta$  continuously decreases throughout the course of the experiment.

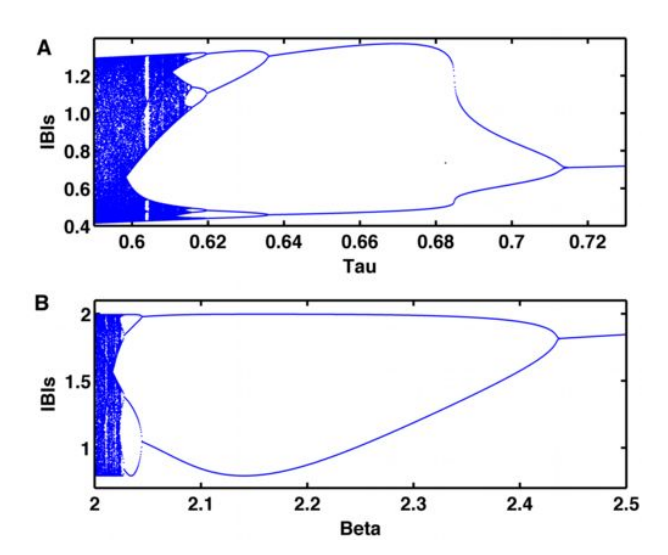


Figure 2–4: Bifurcation diagram of the one-dimensional maps that simulate the drug-induced chaotic cardiac rhythms in Figs. 2–2 and 2–3. (A) Bifurcation diagram of the one-dimensional return map given by Eq. 2.1 that describes the IBIs as a function of the bifurcation parameter,  $\tau$ . The function has five parameters:  $\alpha$ = 35,  $\beta$ =0.42,  $\gamma$ =18,  $\delta$ =0.2, and  $\tau$ , which is the bifurcation parameter.  $\tau$  governs the vertical orientation of the function, and, as  $\tau$  decreases a sequence of period-doubling bifurcations take place. (B) Bifurcation diagram of the one-dimensional return map given by Eq. 2.2. The function has four parameters:  $\alpha$ =23,  $\gamma$ =7,  $\tau$ =2, and  $\beta$ , which is the bifurcation parameter.  $\beta$  represents the horizontal orientation of the map, and, as  $\beta$  decreases, the map shifts towards the curvilinear portion of the map, generating a cascade of period-doubling bifurcations leading to chaos.

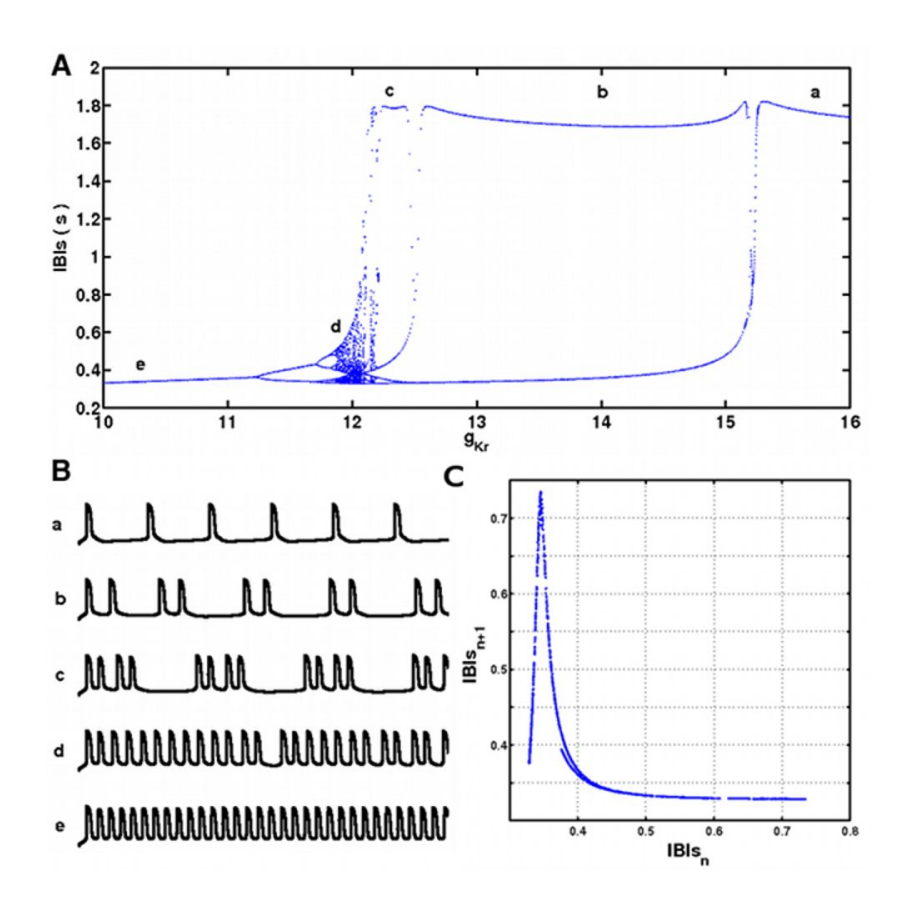


Figure 2–5: Hodgkin-Huxley-style ionic model captures dynamics consistent with experimental dynamics as a consequence of potassium channel blockade. (A) Bifurcation diagram that describes the dynamics of the Hodgkin-Huxley-style model. The asymptotic IBIs of the model are displayed as a function of the hERG potassium channel conductance,  $g_{Kr}$ . (Units for  $g_{Kr}$  are mS/cm<sup>2</sup>.) (B) The time series associated with particular values of the bifurcation diagram. (a) Intrinsic frequency of the single cell. (b) Coupled beats following a period-doubling bifurcation. (c) Bursting dynamics following another period-doubling bifurcation. (d) Chaotic dynamics. (e) Sustained accelerated rhythm. (C) One-dimensional return map of the IBIs within the chaotic regime,  $g_{Kr}$ =11.898 mS/cm<sup>2</sup>.

# CHAPTER 3 Predicting the onset of abnormal alternating rhythms

#### 3.1 Foreword

In the human heart, a number of mechanisms underlie the transition from a normal cardiac rhythm to arrhythmia. The onset of an alternating cardiac rhythm, where, for example, an alternation in the duration of the action potential is observed, represents one such mechanism [160, 82]. These alternating rhythms (alternans) can herald the initiation of arrhythmias, including tachycardia and fibrillation [206, 177, 82]. Furthermore, T-wave alternans is an arrhythmia for which an alternation in the T-wave of the electrocardiogram is observed. Clinically, the manifestation of T-wave alternans increases the patient's risk for sudden cardiac death [171, 201].

The mechanism underlying the transition from normal cardiac rhythm to alternans is linked to a mathematical instability called a period-doubling bifurcation, where the period of the system's oscillation doubles as a consequence of a change in the value of a model parameter [91, 58, 59]. Examples of parameters that can induce a period-doubling bifurcation in cardiac systems include pacing frequency [88], temperature [70], and drugs [110, 167]. Thus, further development of statistical measures to predict the onset of period-doubling bifurcations is clinically relevant. Theoretical studies have demonstrated that, near the onset of the transition, period-doubling bifurcations induce dynamical slowing down and noisy

precursors such as the emergence of an additional peak in the power spectrum [94, 209]. Recent studies have also examined pre-bifurcation amplification of an iterated map's response to alternate pacing protocols [222].

In a previous study from our group and chapter 2 of this thesis, treating spontaneously beating aggregates of cardiac chick cells with E4031, a hERG potassium channel blocker, led to a spectrum of complex dynamics [117, 167], including alternating rhythms, bursting rhythms, accelerated rhythms, and chaotic dynamics. In this chapter, I develop early warning signals to predict the onset of alternating rhythms, which take place through period-doubling bifurcations.

By analyzing the inter-beat intervals, I show that, near the onset of the period-doubling bifurcation, damped oscillations appear in the autocorrelation function, and the standard deviation of the inter-beat intervals increases. Then I provide an analytic framework underlying the changes in these statistical indicators by computing analytic expressions for the autocorrelation function and the probability density function. Lastly, analysis of return maps of interbeat intervals—for which the current inter-beat interval is plotted as a function of the following inter-beat interval—reveals that the slope of the return map represents a quantitative measure that can assess how close the system is to a period-doubling bifurcation. Additionally, I show that the slope measure and the lag-1 autocorrelation coefficient are equal. This work demonstrates the presence of early warning signals for transitions in noisy cardiac systems.

#### 3.2 Results

## 3.2.1 Onset of alternating rhythms

Between 0.5– $2.5~\mu$ mol E4031 was applied to spontaneously beating aggregates of embryonic chick cardiac cells, blocking the human Ether-à-go-go-Related Gene (hERG) potassium channel [42] (see Methods for details on the experimental protocols). Following the application of the drug, the aggregates maintain their intrinsic beat frequency for roughly 10-40 minutes before a qualitative change in the dynamics took place. These transitions gave rise to a spectrum of complex dynamics, including alternating rhythms, bursting oscillations, chaotic dynamics, and accelerated rhythms. We analyzed the dynamics of the aggregates by computing the inter-beat intervals, the time between successive beats.

Of the aggregates we analyzed, 43/104 underwent a period-doubling bifurcation. In 71/104 cases, the aggregates exhibited an alternating rhythm. Figure 3–1A displays the inter-beat intervals from a representative experiment following the application of 1.5  $\mu$ mol E4031 at t=0, where a period-doubling bifurcation of the dynamics takes place at approximately t=50 min. The spaces between the sets of inter-beat intervals in the panel represent the times when recording was stopped for data storage purposes (approximately 2-3 mins). The three representative time series plotted in Fig. 3–1A correspond with the dynamics in the first (i), fourth (ii), and fifth (iii) sets of inter-beat intervals.

Theory predicts that in the neighbourhood of a period-doubling bifurcation the system takes longer to recover to equilibrium following a perturbation [94, 209]. If the system is far from a bifurcation, the system rapidly re-establishes its steady-state value, so the system has no 'memory'—consecutive inter-beat intervals are not correlated. However, close to the period-doubling bifurcation, the system re-establishes the steady-state value less rapidly—and in an oscillatory fashion—leading to a negative correlation between successive beats. We observe negative correlation between successive inter-beat intervals in the neighbourhood of the bifurcation in Fig. 3–1B—panel B is a zoomed-in plot of the fifth set of inter-beat intervals from panel A (corresponding with iii).

To quantify how the statistical features of the inter-beat intervals change as the system approaches the period-doubling bifurcation, we examine the system's noise and autocorrelation. In Fig. 3–2A, we plot the return maps for the first (i), fourth (ii), and fifth (iii) sets of inter-beat intervals from Fig. 3–1A. Based on the return maps, we observe that as the system approaches the period-doubling bifurcation, the variation of the inter-beat intervals increases and successive interbeat intervals become negatively correlated. In Fig. 3–2B, we plot the histograms of the detrended inter-beat intervals again for the same sets of inter-beat intervals examined above in Fig. 3–1A. We show that the distributions of inter-beat intervals spread out, suggesting an amplification of the noise of the inter-beat intervals. We compute the standard deviation for each set of detrended inter-beat intervals and find that the standard deviation of the inter-beat intervals changed from  $\sigma = 0.013$  in the first set of inter-beat intervals to  $\sigma = 0.14$  in the fifth set of inter-beat intervals given in Fig. 3–1A.

In Fig. 3–2C, we compute the autocorrelation function for a set of detrended inter-beat intervals (20 beats long) centred at the 150th beat for the same three

sets of inter-beat intervals we looked at above. Near the beginning of the experiment (t=0), because the system is far from the bifurcation, successive inter-beat intervals are uncorrelated, so the lag-1 autocorrelation coefficient is approximately equal to zero, as shown in the autocorrelation functions computed for i (left panel) and ii (middle panel) in Fig. 3–2C. However, as the system nears the bifurcation, damped oscillations emerge in the autocorrelation function, reflecting the effect of longer recovery times following perturbations in the neighborhood of the bifurcation, as shown in the right panel of Fig. 3–2C. We propose that the emergence of damped oscillations in the autocorrelation function and an amplification of the system's noise represent possible early warning signals to anticipate the onset of period-doubling bifurcations.

## 3.2.2 Analysis of early warning signals

In chapter 2 of this thesis, we modelled the inter-beat intervals observed in the experimental data following the treatment with E4031 using an exponential nonlinear one-dimensional map in the absence of noise. However, the dynamics of virtually all biological systems are influenced by noise. Therefore, we consider the following continuously perturbed exponential nonlinear one-dimensional map to model the inter-beat intervals following the treatment of E4031:

$$x_{n+1} = \alpha e^{(-\beta(x_n - \gamma))} + \delta + \sigma \zeta_n \tag{3.1}$$

where  $x_n$  represents the *n*th inter-beat interval,  $\zeta_n$  is a random variable drawn from a normal distribution with a mean equal to zero and a standard deviation equal to one.  $\sigma$  is a positive parameter, which we assume to be equal to 0.01, consistent with the fluctuations observed in the inter-beat intervals when the system is far from the bifurcation.  $\alpha, \beta, \gamma$ , and  $\delta$  are parameters that govern the shape of the exponential map. To simulate the experiments, we study the dynamics of the map as we decrease  $\gamma$ . The map has a unique fixed point, which, at a critical  $\gamma$ , destabilizes, giving rise to a period-doubling bifurcation. (See Methods for full description of numerical simulations and parameter values.)

To gain mathematical insight into the early warning signals observed in the experimental data, we set out to derive analytic expressions for both the probability density function and the autocorrelation function as the system approaches a period-doubling bifurcation. We approximate the dynamics of Eq. 3.1 using a continuously perturbed linear one-dimensional map with a unique fixed point at  $x^* = 0$ , examining the dynamical features as the slope at the fixed point approaches -1, the requirement for the initiation of a period-doubling bifurcation. We define the noisy linear map as follows:

$$x_{n+1} = Ax_n + \sigma\zeta_n \tag{3.2}$$

where  $x_n$  represents the deviation of the *n*th inter-beat interval from the mean,  $\zeta_n$  is a random variable drawn from a normal distribution with a mean of zero and a standard deviation equal to one. Again,  $\sigma = 0.01$ , which is consistent with the system-level noise of the experimental data. A represents the slope of the map at the fixed point,  $x^*$ . Following work from [194, 180], we analytically compute the probability density function. Iterating the map directly leads to the following

series:

$$x_n = \sum_{i=0}^n A^i \sigma \zeta_{n-i} \tag{3.3}$$

We computed the probability density function as  $n \to \infty$  as follows:

$$f_n(x; A, \sigma) = \sqrt{\frac{1 - A^2}{2\pi\sigma^2}} \exp\left(\frac{-x^2(1 - A^2)}{2\sigma^2}\right)$$
 (3.4)

The standard deviation of the probability density function is as follows:  $\zeta(\sigma, A) = \sigma/\sqrt{1-A^2}$ . Assuming  $\sigma$ , the system's intrinsic noise, remains constant, the analytic expression shows that as A, the slope through the fixed point, approaches -1 the standard deviation of the system increases nonlinearly. Figure 3–3A shows representative return maps for Eq. 3.2 for three values of A: -0.05, -0.65, and -0.95. In Fig. 3–3B, we superimpose the analytic expressions for the probability density functions as defined by Eq. 3.4 for the three values of A upon histograms of data generated by Eq. 3.2—the numerical simulations and the analytical expression are in close agreement. Consistent with the experimental data, we show that, as the system approaches the transition point, we observe an increase in the variation of the system.

To derive the analytic expression of the autocorrelation function for a noisy linear map, we define the autocorrelation function for a discrete system:

$$\rho(k) = \frac{\sum_{t=1}^{n-k} (x_t - \mu) (x_{t+k} - \mu)}{\sum_{t=1}^{n} (x_t - \mu)^2}$$
(3.5)

where n is the length of the time series,  $\mu$  is the mean ( $\mu = 0$  for this example), and  $\rho(k)$  represents the autocorrelation function at lag k. Considering that random inputs lack correlation, we derive the autocorrelation function:

$$\rho(k) = A^k \tag{3.6}$$

Thus, for A < 0, we observe damped oscillations in the autocorrelation function as a function of the lag coefficients. Additionally, as A approaches -1, the autocorrelation function decays to zero (no correlation) less rapidly, and the oscillations in the autocorrelation function grow in amplitude, properties consistent with experiments. In Fig. 3–3C, we superimpose the analytic expression, Eq. 3.6, over the numerically computed autocorrelation for three values of A. The numerically computed autocorrelation function and the analytical expression for the autocorrelation function show close agreement.

We examine how accurately the analytic expressions derived from the noisy linear map matched the dynamics in the neighborhood of the period-doubling bifurcation from the noisy nonlinear map, Eq. 3.1. Figure 3–4A shows the return maps computed from Eq. 3.1 for three values of  $\gamma$ : 3.0, 1.75, and 1.5 for  $\sigma$  = 0.01. Consistent with the return maps displayed in Fig. 3–2A, as  $\gamma$  decreases, the slope through the fixed point approaches -1, the requirement for the initiation of a period-doubling bifurcation, and the noise of the system increases. Figure 3–4B displays the superimposed analytic expressions for the probability density functions as defined by Eq. 3.4, where A represents the slope of the function at the fixed point, over the numerically generated data. The analytic expression is consistent with the numerical simulations. Figure 3–4C shows the numerically computed autocorrelation function and the fitted analytic expression from Eq. 3.6.

Again, the analytic expression of the autocorrelation function for the linear case shows good agreement with the numerically generated autocorrelation function for the nonlinear map.

# 3.2.3 Quantitative measure that predicts the onset of alternating rhythms

Returning to the experimental data, we test a prediction that emerged from the analysis: that the slope from a linear regression of a return map composed of a sliding window of detrended inter-beat intervals could provide a quantitative measure to assess how close the system is to a period-doubling bifurcation. Period-doubling bifurcations in continuously perturbed discrete systems take place when the slope through the fixed point goes through -1. Therefore, the distance from -1 of the slope measure represents a quantitative early warning signal for a period-doubling bifurcation.

We examine the inter-beat interval dynamics of eight aggregates for which we observe and capture a period-doubling bifurcation (see Methods for further details). Figure 3–5 shows that when the slope goes below -0.75 for at least five consecutive beats, the period-doubling bifurcation takes place between 3 and 232 beats later—approximately 3 to 200 seconds in the future. We consider a period-doubling bifurcation to have taken place when the slope measure goes below -0.98 for at least five consecutive beats. In Fig. 3–5, the black dashed lines represent the time at which the system goes through the early warning signal (slope = -0.75) and the red dashed lines represent the time at which the system goes through the period-doubling bifurcation (slope = -0.98). The mean number of beats of advanced warning is 86.6 beats. We consider a false alarm to occur when the slope

of the system goes below -0.75 for five consecutive beats and the period-doubling bifurcation does not take place within 300 beats of the early warning signal. Analyzing the time before the onset of the period-doubling bifurcations (typically 30-50 mins) for all eight aggregates that exhibited the transition, we found exactly one false alarm for a threshold of -0.75.

Many studies have used an increase in the lag-1 autocorrelation coefficient as an early warning signal to predict oncoming dynamic transitions [180, 49, 50, 47]. Equation 3.6 represents an analytic expression for the autocorrelation coefficients as a function of the slope through the fixed point, A, of the nonlinear map. The analytic expression predicts that the lag-1 autocorrelation coefficient (k = 1) should be equal to the slope through the fixed point of the map. In Fig. 3–5, we plot the lag-1 autocorrelation coefficient computed from a sliding window of the previous 20 detrended inter-beat intervals and show that the prediction from Eq. 3.6 is consistent with the slope of the linear regression for the experimental data.

To examine the slope measure in a theoretical framework, we modeled the period-doubling bifurcation using Eq. 3.1 by linearly decreasing the value of  $\gamma$  towards and through the bifurcation point (see Methods for further details and parameter values). To mimic the experiments, we applied both parametric noise to  $\gamma$  and system-level noise as given in Eq. 3.1. In Fig. 3–6A, we compute the slope measure, the lag-1 autocorrelation coefficient, and the value of the slope at the fixed point given by Eq. 3.1 as a function of  $\gamma$ . Consistent with the experiments, all three measures approach -1 as the system nears the period-doubling bifurcation. The black dashed line represents the early warning signal

and the red dashed line represents the period-doubling bifurcation, with the same criteria given above—the early warning signal predicts the onset of the bifurcation 69 beats in advance. Figure 3–6B gives the values of x for the system with the corresponding values of  $\gamma$  given below in Fig. 3–6C.

### 3.3 Discussion

In order for early warning signals to be practically useful, they should provide quantitative information to make predictions [19, 49]. We found that when the slope of the experimental fixed point (also equal to the lag-1 autocorrelation coefficient) reached -1, the system underwent a period-doubling bifurcation. The slope and the lag-1 autocorrelation coefficient, therefore, represent quantitative early warning signals that can predict the onset of period-doubling bifurcations. This is related to the establishment of a new steady-state through a saddle-node bifurcation if the slope through the fixed point goes through one [180].

In this study, there is diversity in the behaviour of the aggregates in the neighborhood of the bifurcation. In particular, as the system nears the bifurcation, the slope and lag-1 autocorrelation coefficient approach -1 at different rates and with complex trajectories, Fig. 3–5. What accounts for this diversity? To address this question, in Fig. 3–6, we model the transition using a one-dimensional map, where we attempt to include all the features associated with the period-doubling bifurcation: (i) shifting baseline value of the fixed point, (ii) system-level noise, (iii) parametric noise, (iv) the nonlinear nature of the one-dimensional map, and (v) the dynamic influence of slowing down on all of these properties. Consistent with the experiments, the slope and lag-1 autocorrelation coefficient

trajectories in the neighborhood of the bifurcation are complicated and somewhat unpredictable. Thus, even though the type of dynamic transition is known a priori, the nonlinear interactions between various features of the complex system present challenges in predicting when exactly a transition will take place. This diversity in dynamic behaviour in the neighborhood of the bifurcation was only revealed as a consequence of the large quantities of data we analyzed in this study. The development of early warning signals is often a data-starved domain. Thus, we posit that the development of optimal early warning signals for any dynamic transition requires large amounts of data, owing to the large number of factors associated with the transition. Future studies of early warnings preceding bifurcations should track the change of the appropriate parameter (e.g. slope of the return map) to assess the distance from the transition and the rate at which it is approached.

To date, the study of early warning signals has focused on the nonlinear dynamics near the onset of saddle-node bifurcations. While these bifurcations are relevant in many fields, transitions in dynamical systems can take place through a number of different bifurcations. The development and experimental validation of early warning signals for these other bifurcations remains an open research direction.

Alternating rhythms in the heart can precede propagation block that leads to the onset of reentrant arrhythmias ('reentry'). Spiral waves, vortices of electrical activity, are thought to represent one of the central mechanisms underlying reentry. In chapter 4, to examine mechanisms associated with spiral wave initiation, I perform intracellular calcium imaging of 1-cm-diameter cardiac monolayers composed of embryonic chick cardiac cells following the introduction of inexcitable regions, analyzing this experimental data using numerical simulations.

### 3.4 Methods

## 3.4.1 Spontaneously beating aggregates of cardiac cells

The aggregates were prepared according to the method of DeHaan [53]. The ventricles of seven-day-old White Leghorn chick embryo hearts were dissected and dissociated into single cells by trypsinization. The cells were added to an Erlenmeyer flask containing a culture medium gassed with five per cent  $CO_2$ , 10 per cent  $O_2$ , 85 per cent  $N_2$  (pH = 7.4), and placed on a gyratory shaker for 24–48 h at 37 °C. The aggregates had a diameter of approximately 100–200  $\mu$ m. The aggregates beat with an intrinsic period of between 0.7–2 s. The experiments were conducted two to six hours after the aggregates were plated. We used an optical imaging apparatus that monitored the aggregates' motion. The device recorded the light-intensity variation of a specific pixel on the edge of an aggregate. The edge pixel data was then processed through a bandpass filter (cutoff frequencies: 0.1 Hz—6.5 Hz). Using MATLAB, the beats and the time interval between consecutive beats, the inter-beat intervals, were calculated. The system employed phase-contrast imaging sampled at 40 Hz and a CCD camera (RedShirtImaging, LLC, NeuroCD-SM) at an  $80 \times 80$  pixel spatial resolution. Recordings were carried out at 35–37°C. The beating patterns of multiple aggregates (between 4-20) were recorded simultaneously.

## 3.4.2 Detrending inter-beat intervals

To filter out short-term fluctuations in the inter-beat intervals in the analysis, we detrend the inter-beat intervals using the detrend function in MATLAB. This function first performs a least-squares linear regression for a sliding window of inter-beat intervals. Then the linear regression is subtracted from the raw values of the inter-beat intervals, which leaves the deviation from the regression. To compute the histograms of the deviation from the mean in Fig. 3–2B and the autocorrelation functions in Fig. 3–2C, we use a detrended sliding window composed of 20 beats in all cases. We performed these analyses for larger and smaller window sizes, and the increase in the standard deviation and the oscillations in the autocorrelation function were observed robustly.

#### 3.4.3 Numerical simulations of the nonlinear model

We simulate the period-doubling bifurcation that the inter-beat intervals of the aggregates undergo using a nonlinear one-dimensional exponential map given by Eq. 3.1,  $x_{n+1} = \alpha e^{(-\beta(x_n - \gamma))} + \delta + \sigma \zeta_n$ , where  $x_n$  represents the *n*th inter-beat interval,  $\zeta_n$  is a random variable drawn from a normal distribution with a mean equal to zero and a standard deviation equal to one with the following parameter values:  $\alpha = -0.804$ ,  $\beta = -1.115$ , and  $\delta = 2.423$ . In Fig. 3–4, we plot the return map, histogram, and autocorrelation function for three values of  $\gamma$ : 3.0 (left), 1.75 (middle), and 1.5 (right). For the return maps in Fig. 3–4, we simulate Eq. 3.1 starting from a random initial condition for 5000 values of x, and plot the return map for the last 4000 x values. We also apply normally-distributed systemlevel noise with a standard deviation  $\sigma = 0.01$ , consistent with the fluctuations

associated with the inter-beat intervals when the system is far away from the bifurcation. For the histograms, we plot the deviation from the mean x value from the simulations.

# 3.4.4 Slope and autocorrelation calculated from the inter-beat intervals

The quantitative measure that assesses how far the system is from the period-doubling bifurcation is given by the slope of a return map—a plot where the following inter-beat interval is given as a function of the current inter-beat interval—composed of a detrended sliding window of inter-beat intervals. We first detrend the raw inter-beat intervals using the method given above. From the detrended data, we plot return maps composed of a sliding window composed of the previous 20 beats. Then we compute a linear regression (least-squares) through each return map, where our slope measure, Fig. 3–5, represents the slope of the linear regression. We compute the lag-1 autocorrelation coefficient using the 'autocorr' function in MATLAB with a sliding window composed of the previous 20 detrended inter-beat intervals.

# 3.4.5 Slope and autocorrelation calculated from the numerical simulations

We simulate the nonlinear map given above with the following parameter values  $\alpha = -0.804$ ,  $\beta = -1.115$ , and  $\delta = 2.423$ , while linearly decreasing the value of  $\gamma$  such that we simulate the system approaching the period-doubling bifurcation. We apply system-level, normally-distributed noise with a standard deviation  $\sigma = 0.01$ , consistent with the fluctuations associated with the inter-beat intervals when the system is far away from the bifurcation. We linearly decrease the value of  $\gamma$  along the linear function  $\gamma_1(t) = 5.01 - 0.012 \cdot t$  for the first 300 beats and then the

linear function  $\gamma_2(t) = 2 - 0.002 \cdot t$  for the remaining 50 beats, where t represents the beat number from the figure. We apply parametric, normally-distributed noise with a standard deviation equal to 0.05 to the value of  $\gamma$ , which we calculated by considering a quasi-stationary sequence of the slope measure from the experimental data. We compute the slope measure and the lag-1 autocorrelation coefficient with a sliding window composed of the previous 20 values of x using the same method as given in the Methods section above.

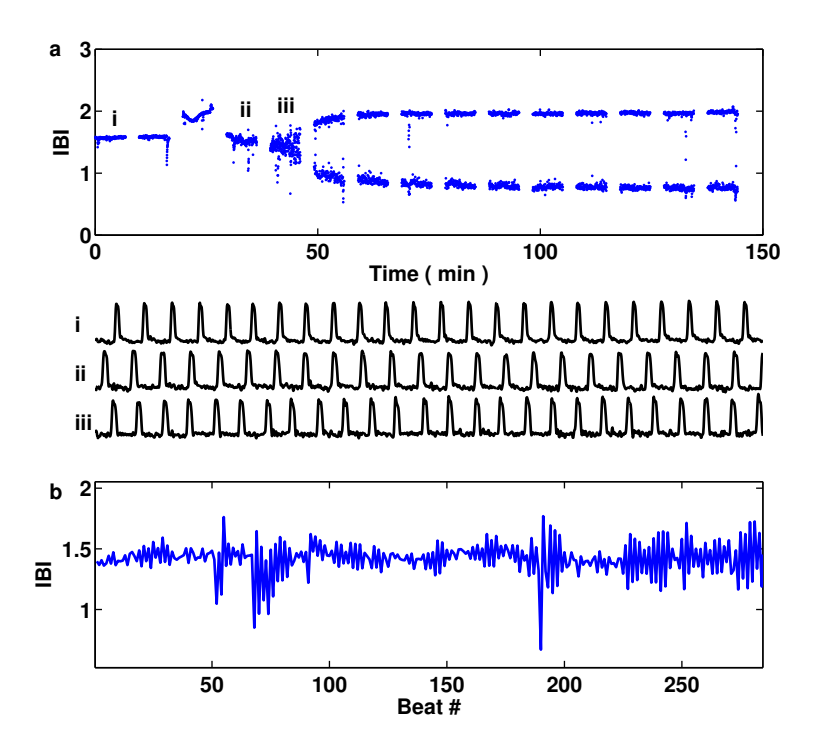


Figure 3–1: Period-doubling bifurcation in an aggregate of embryonic chick cardiac cells following treatment with a potassium channel blocker. (a) Inter-beat intervals through time following the application of E4031 at t=0. There are spaces between sections of data for storage reasons. A period-doubling bifurcation takes place at approximately t=50 min. The traces below the inter-beat intervals—i, ii, and iii—represent time series corresponding with the inter-beat intervals in the first, fourth, and fifth sets of inter-beat intervals. (b) The fifth set of inter-beat intervals (from approximately t=42 min to t=48 min) corresponding with iii in panel A. This set of data precedes the period-doubling bifurcation.

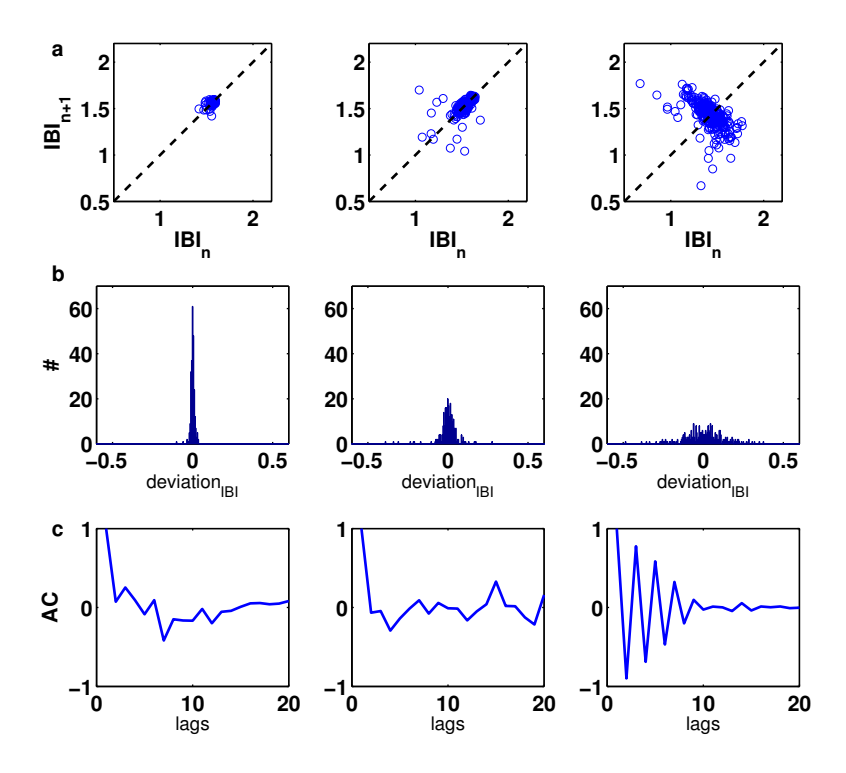


Figure 3–2: Detection of noise amplification and oscillations in the autocorrelation function of the aggregate's inter-beat intervals in the neighbourhood of the period-doubling bifurcation following treatment with potassium channel blocker. (a) Return maps of the inter-beat intervals from the first (i), fourth (ii), and fifth (iii) sets of inter-beat intervals from Fig. 3–1A. (b) Histograms of 250 detrended inter-beat intervals (see Methods for details on detrending) for the three sets of inter-beat intervals (i,ii, and iii) from Fig. 3–1A. Deviation represents the deviation of each IBI from the mean value computed through the detrending process. The standard deviation increases as the system approaches the period-doubling bifurcation, particularly in iii. (c) Autocorrelation function for a window of 20 detrended beats centred on the 150th beat for three sets of inter-beat intervals. Damped oscillations emerge in the autocorrelation function in iii, consistent with the oscillations in the inter-beat intervals observed in Fig. 3–1B.

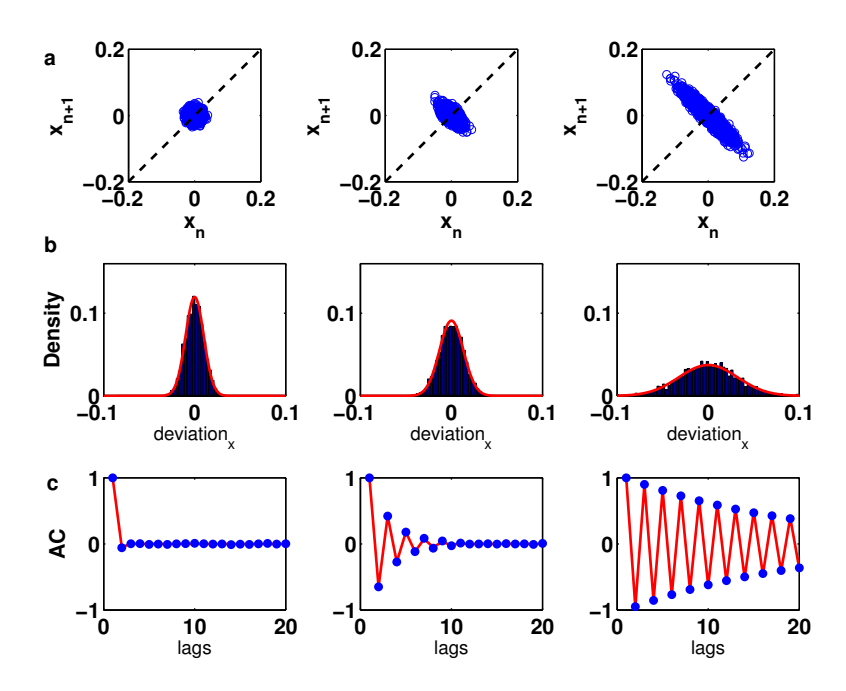


Figure 3–3: Detection of noise amplification and oscillations in the autocorrelation function as the slope at the fixed point of a continuously perturbed linear map approaches -1. (a): Representative return maps for three values of A (the slope at the fixed point): -0.05 (left-hand column), -0.65 (middle columns), and -0.95 (right-hand column). For these simulations, we applied normally-distributed noise with a standard deviation  $\sigma = 0.01$ . (b): Histograms of the the deviation from the mean for the last 4000 values of x (as shown above in the return maps) for the three values of A. The red curves represent the probability density functions computed using Eq. 4 as given in the paper. (c): Autocorrelation functions for the three above values of A. The blue dots represent the numerically computed autocorrelation function and the red curve represents the analytical expression for the autocorrelation function calculated using Eq. 6 in the paper.

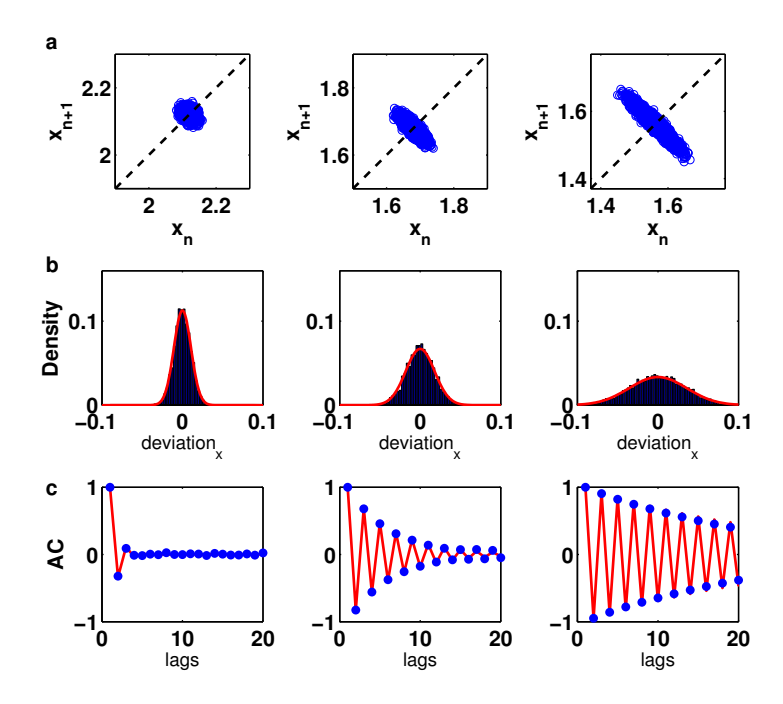


Figure 3–4: Detection of noise amplification and oscillations in the autocorrelation function for a model of the data in the neighbourhood of a period-doubling bifurcation. (a) Return maps computed from Eq. 3.1 for  $\gamma = 3.0$  (left), 1.75 (middle), and 1.5 (right). (b) Histograms and probability density functions corresponding to the data that make up the return maps. Deviation represents the deviation of each x value from the mean value of the sequence of x values. The red curve represents the analytic expression of the probability density function computed from the linear approximation, Eq. 3.4. (c) The blue dots represents the analytic expression computed from the linear approximation, Eq. 3.6, for all three values of  $\gamma$ .

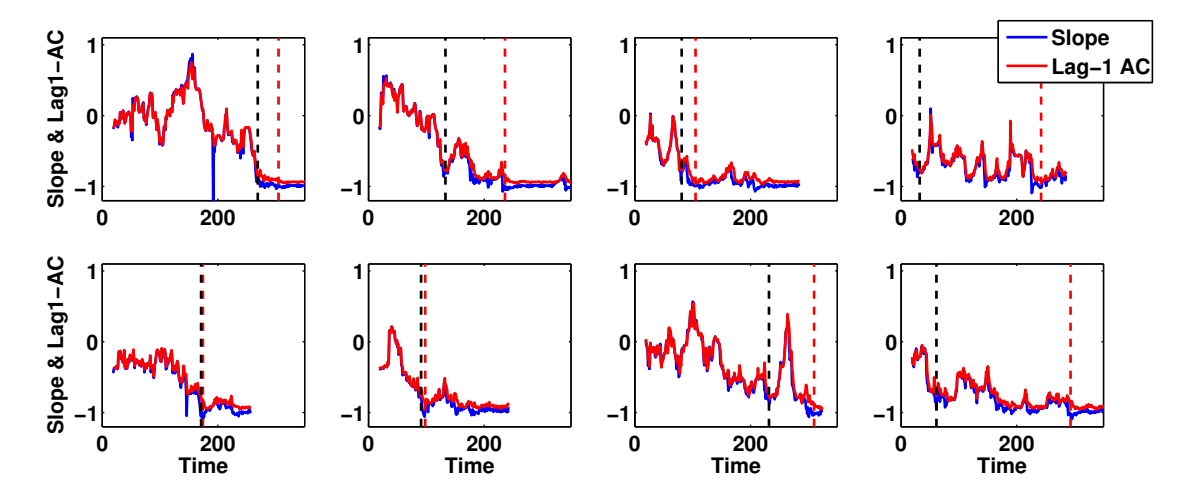


Figure 3-5: Slope of a return map of inter-beat intervals and the lag-1 autocorrelation coefficient represent quantitative measures that assess how far the aggregates' dynamics are from a period-doubling bifurcation. Each panel represents an aggregate for which we observed and captured a period-doubling bifurcation in the dynamics of the inter-beat intervals. The slope (in blue) represents the slope of a linear regression of a sliding window of the previous 20 detrended inter-beat intervals. The lag-1 autocorrelation coefficient of a sliding window composed of the previous 20 detrended inter-beat intervals, plotted in red, is consistent with the slope of the linear regression of the return map. This is predicted by Eq. 3.6 for k=1, where A represents the slope through the fixed point (simply the slope of the linear regression here). The black hatched line represents the beat at which the slope first remains under -0.75 for 5 consecutive beats, which we consider the early warning signal. The red hatched line represents the beat at which the slope first remains under -0.98 for at least 5 consecutive beats, which we consider as when the system goes through the period-doubling bifurcation.

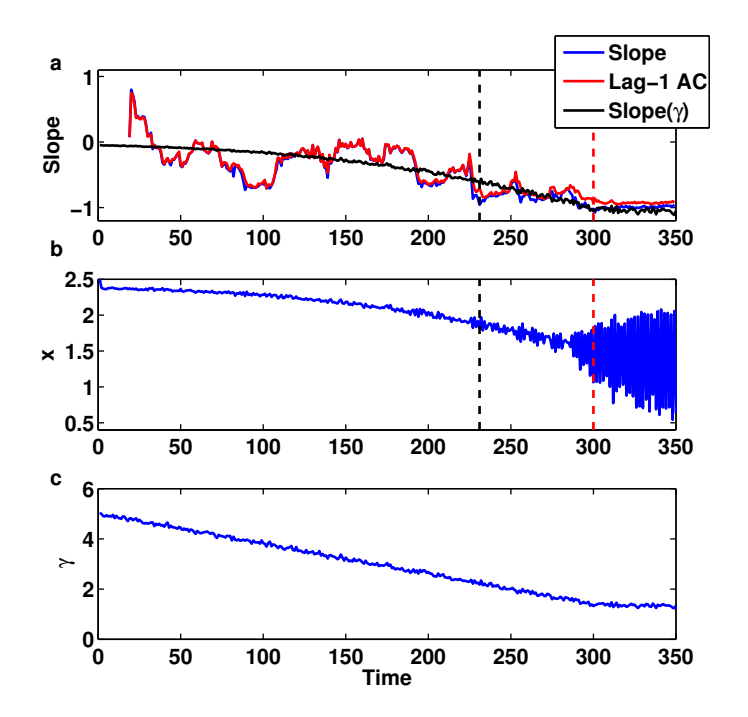


Figure 3-6: Slope of a return map and the lag-1 autocorrelation coefficient represent quantitative measures that assess how far the dynamics of the mathematical model of the experiments are from the perioddoubling bifurcation. We linearly decreased the value of  $\gamma$  from Eq. 3.1, which gave rise to a period-doubling bifurcation. (a) The slope of the return map (in blue) represents the slope of a linear regression through a return map composed of a sliding window of the previous 20 detrended values of x (as given in panel b). The lag-1 autocorrelation coefficient of a sliding window composed of the previous 20 detrended values of x (in red) is consistent with the slope of the linear regression of the return map. Slope( $\gamma$ ) represents the slope of the fixed point as calculated using Eq. 3.1 and the current value of  $\gamma$  as given in panel c. The black dashed line represents the early warning and the red hatched line represents the period-doubling bifurcation. The signal gives the system 69 beats of advanced warning. (b) The value of x as numerically generated by Eq. 3.1 as a function of time. Again the black dashed line represents the early warning and the red dashed line represents the period-doubling bifurcation. (c) The value of  $\gamma$  as a function of time.

#### CHAPTER 4

# Spatial symmetry breaking determines spiral wave chirality

## 4.1 Foreword

Spiral waves, self-sustaining vortices of activity, have been observed in diverse biological and chemical contexts [52, 157, 103], and have been linked to mechanisms underlying various cardiac arrhythmias [152, 105]. Chirality ('rotation direction') represents a fundamental property of spiral waves [217, 220, 219, 190, 1], and has recently been implicated in the dynamics of spiral wave anchoring to inexcitable obstacles [221]. The key factors regulating spiral wave chirality, however, remain unclear. A number of mechanisms have been implicated in spiral wave initiation [52, 159, 215, 24, 207, 5]. Here, we investigate how inexcitable obstacles can lead to the initiation of spiral waves propagating in the tissue neighbouring the obstacle [159, 215]. To examine how the position of an inexcitable obstacle influences the chiral properties of these spiral waves, we introduced obstacles of varying sizes, approximately 1–8 mm in width, into cardiac monolayers (two of the preparations had two obstacles introduced).

## 4.2 Experimental methods

## 4.2.1 Introducing inexcitable regions into cardiac monolayers

We incubated 30 fertilized white leghorn chick eggs at 37 °C for 7-8 days [53, 21]. We removed the ventricular portions of the embryonic hearts, dissociating the cells with trypsin. The cells were centrifuged, suspended in 818A medium

[53, 21], and plated in 10-mm-diameter circular glass rings on 35-mm-diameter plastic culture dishes. We incubated the cells for 48 hours at 37 °C and 5 per cent CO<sub>2</sub> during which time the monolayers formed—16 monolayers were included in the study. Thirty minutes prior to imaging, we loaded the cells with Calcium Green-1, a fluorescent dye that tracks intracellular calcium. The cells were imaged at between 35 - 37  $^{\circ}\mathrm{C}$  using a custom-built macroscope with a 1  $\mathrm{cm}^{2}$  field of view—we imaged the entire preparation (1-cm diameter). The system excites the calcium dye at 500 nm and monitors emission at 545 nm. The fluorescence was sampled at 40 Hz, with a spatial resolution of  $80 \times 80$  pixels (0.15  $\mu$ m<sup>2</sup>). The dish was continuously perfused with fresh Hank's solution [53]. Side pacemakers emerged spontaneously with periods of 1–2 s. The wavefront propagation velocity was approximately 4-5 mm/s. We introduced obstacles into the monolayers by surgical ablation. In particular, following the dye-loading incubation period, we made incisions into the monolayer using a fine x-acto blade, representing the approximate outline of a square, though due to the difficulty of the surgery some of the incisions were curvilinear. (In the two preparations with two obstacles, the obstacle shape was more circular.) We then excised the cells from within the outline of the obstacle. In some of the preparations, cell debris—and the associated calcium signal—became attached to the bottom of the dish in the obstacle area. This debris, however, was nonfunctional and did not influence the monolayer's dynamics. The approximate centre of the obstacle was selected to be as close to the middle of the monolayer as possible. The fluorescent images were

acquired using a Cardio-CCD camera with Cardioplex software (Redshirt Imaging) approximately 3–5 minutes after the surgical ablation took place.

## 4.3 Experimental results

## 4.3.1 Spiral wave diversity in monolayers with inexcitable regions

We observed a spectrum of spiral wave dynamics in the experimental recordings, including clockwise-rotating spiral waves (8), counterclockwise-rotating spiral waves (10), opposite-chirality pairs of spiral waves (4), a same-chirality clockwise-rotating pair of spiral waves (1), and same-chirality counterclockwise-rotating pairs of spiral waves (2). We determined the chirality through visual inspection. Transitions took place between spiral wave chiralities over the course of a single recording. In Fig. 4–1A, two counterrotating spiral waves govern the dynamics of a monolayer with an obstacle approximately 2 mm wide. In Fig. 4–1B, a counterclockwise-rotating spiral wave governs the dynamics of a monolayer with an obstacle approximately 5 mm in diameter. Further, the positions of the obstacles are different: the approximate centroid of the obstacle in Fig. 4–1A is positioned down and to the left with respect to the centroid of the obstacle in Fig. 4–1B.

The ubiquity of spiral waves observed in the experimental recordings led us to consider mechanisms of obstacle-induced spiral waves. Figure 4–2 shows the initiation of an obstacle-induced spiral wave. We observed this transition in a five-minute recording in which a counterclockwise-rotating spiral wave on the left-hand-side of the monolayer with a spiral period of approximately 0.55 s rapidly paced the tissue, initially generating wavefronts that propagated around a central obstacle that was positioned closer to the upper boundary, Fig. 4–2A.

Approximately three and a half minutes later, waves emitted from the spiral wave detached from the obstacle, leading to the initiation of a counterclockwise-rotating spiral wave with a period of approximately 0.65 s, Fig. 4–2B.

# 4.4 Theoretical methods

## 4.4.1 Rapid pacing leads to the onset of spiral waves

Theoretical studies have demonstrated that rapid side pacing of a sheet of cardiac tissue with an inexcitable and a partially excitable obstacle can lead to spiral wave initiation [159, 215, 17, 141]. We investigated how the location of an obstacle with respect to a side pacemaker influenced the rotation direction of the initiated spiral waves using a highly simplified model of wave propagation through cardiac tissue based on the classic FitzHugh-Nagumo equations [92, 21]:

$$\frac{\partial v}{\partial t} = \frac{1}{\epsilon} \left( v - \frac{v^3}{3} - w \right) + I_p + D \left( \frac{\partial^2 v}{\partial x^2} + \frac{\partial^2 v}{\partial y^2} \right) 
\frac{\partial w}{\partial t} = \epsilon \left( v + \beta - \gamma w \right) g(v)$$
(4.1)

where  $\epsilon$ =0.42,  $\beta$ =0.7, and  $\gamma$ =0.5. v represents the activation variable, the cells' transmembrane voltage, and w represents the tissue's recovery processes. We first tuned the parameters to locate a region in parameter space in which rapid side pacing would lead to spiral wave initiation. We then explored the range of the tissue's excitability parameter,  $\epsilon$ , for which we could initiate spiral waves. Because cardiac monolayers composed of embryonic chick cells are slow conducting, we selected a larger value for  $\epsilon$ . We integrated the equations using an Euler integration scheme with a dt=0.98 msec (0.025 time units) and dx=dy=0.0083 cm (0.025 space units) on a 1 cm  $\times$  1 cm grid. We scaled the arbitrary time

and space units such that the dimensions of the system and the conduction velocity of propagating wavefronts were consistent with experiments. The diffusion coefficient is  $D=0.0028~{\rm cm^2s^{-1}}$ . The boundary conditions along the edge of the square grid are no flux. We set D=0 in the inexcitable obstacle, and in the tissue between the edge of the square grid and the monolayer's circular boundary.  $I_p$  and  $g(v)=(w_h-w_p)/(1+e^{-4v})+w_p$  control the tissue's pacemaker properties. The periodic trajectory of the model can be split into four phases: the upstroke, the plateau, repolarization, and the pacemaker phase.  $w_p$  simply controls the rate of trajectory through the pacemaker phase. In the circular-shaped side pacemaker region (0.83 mm in diameter) located on the left-hand-side of the sheet,  $I_p=1$ ,  $w_h=0.6$ , and  $w_p$  is varied from between 0.15 to 0.66 to control the frequency. For the rest of the active cells,  $I_p=0$ ,  $w_h=0.6$ , and  $w_p=0.4$ . The sheet of tissue is isotropic, consistent with the lack of fiber orientation typically observed in monolayers. The obstacle is square-shaped (2.5 mm in length) and is located in the center unless otherwise indicated.

#### 4.5 Theoretical results

#### 4.5.1 Spatial symmetry breaking determines spiral wave chirality

First, we considered the spatially symmetric system shown in Fig. 4–3A. Figure 4–3A displays the steady-state dynamic following a 19.62-second burst of rapid pacing at a pacemaker period of  $T_p = 0.548$  s, which gave rise to a pair of opposite-chirality spiral waves (the 'time' given in the figure's panels is the time elapsed following the cessation of pacing). We broke the spatial symmetry by

positioning the obstacle above the central axis of symmetry by 0.75 mm, Fig. 4–3B, and pacing the tissue at the same period ( $T_p = 0.548$  s), which led to the initiation of a counterclockwise-rotating spiral wave. Figure 4–4 shows the details of the initiation of the counterclockwise-rotating spiral wave during rapid pacing. The chirality of the initiated spiral wave observed numerically is consistent with the experimental trace in Fig. 4–2, in which an obstacle positioned closer to the upper boundary led to the initiation of a counterclockwise-rotating spiral wave following rapid pacing.

## 4.5.2 Frequency-dependent transition in spiral wave chirality

Since frequency-dependent transitions are ubiquitous in the dynamics of cardiac systems, we examined how spiral wave dynamics changed as a function of side pacemaker period  $(T_p)$  when the obstacle was positioned above the central axis of symmetry by 0.75 mm. To mimic the experimental conditions, we introduced sparse randomly-distributed heterogeneities ('breaks') into the medium by selecting a probability at each grid point of setting the diffusion coefficient equal to zero,  $m_b$ = 0.000837 [21].

We generated 20 substrates, simulating each substrate through a range of  $T_p$ , Fig. 4–5. For each  $T_p$  value, using visual inspection, we classified the dynamics (following 100,000 iterations corresponding to approximately one and a half minutes in the experimental system) into four behaviours: clockwise-rotating spirals, counterclockwise-rotating spirals, no spiral formation, and others, which included pairs of spiral waves of the same or opposite chirality, and groups of 3 or more spiral waves. Then we computed the moving average of the fraction f of the

experiments (out of 20) that displayed each spiral wave behaviour (Fig. 4–5 shows the number of clockwise- and counterclockwise-rotating spiral waves and Fig. 4–6 displays all spiral wave behaviour.) We averaged the corresponding f values over two  $T_p$  discretizations (totalling 0.002 s) to smooth out short-term noise-induced fluctuations.

At  $T_p$  values > 0.59 s, spiral waves did not form because the substrate supported the stable propagation of waves through the system. Second, at \*1 in Fig. 4–5, the region above the obstacle destabilized, leading to the initiation of predominantly clockwise-rotating spiral waves (typically forming above the obstacle). Third, at \*2 in Fig. 4–5, the region below the obstacle destabilized, leading to the initiation of predominantly counterclockwise-rotating spiral waves. Lastly, for short  $T_p$  values, the pacemaker transitioned from 1:1 propagation (in which 1 pulse propagates away from the side pacemaker region for every stimulus) to 3:2 propagation (in which 2 pulses propagate away from the side pacemaker for every three stimuli) and spiral wave formation was infrequent.

#### 4.5.3 Action potential duration restitution curve analysis

Spiral wave initiation takes place in a region of the substrate following an instability that leads to propagation block. Action potential duration (APD) restitution curves predict the onset of instabilities in excitable media [91, 58, 125]. We computed steady-state APD restitution curves at positions both above and below the obstacle (see Fig. 4–4 for the precise locations) by varying  $w_p$ , the parameter controlling the pacemaker period. Both spatial locations are 0.75 mm from the left edge of the obstacle and 0.17 mm above or below the obstacle.

We considered the duration of the action potential to be the time that v is greater than -0.5. We fit the steepest portions of the curves only to maximize the precision of the pacing period at which these maps destabilized. We fit the following exponential to both of the restitution curves:  $f(\rho) = \alpha e^{\eta(\rho-\delta)} + \Gamma$  where for the curve computed above the obstacle:  $\alpha = -0.89$ ,  $\eta = -5.32$ ,  $\delta = 11.06$ , and  $\Gamma = 3.34$ —and for the curve computed below the obstacle:  $\alpha = -0.51$ ,  $\eta = -5.74$ ,  $\delta = 10.80$ , and  $\Gamma = 3.26$ . The output from these curves was in time units (t.u.). To convert to seconds, we applied the time scale factor: 1 t.u. = 0.0392 s. The morphology of the restitution curves along the top and bottom edges of the obstacle change due to the interactions of the curved wavefront with the obstacle. However, given two restitution curves the same distance along both the top and bottom edge (with the same threshold), the restitution curve along the top of the obstacle becomes steeper before the restitution curve along the bottom of the obstacle because the wavefront curvature is greater along the top edge.

We plotted the corresponding APD restitution curves in Fig. 4–7A, where the blue curve corresponds with the location above the obstacle, and the red curve corresponds with the location below the obstacle. To compute the  $T_p$  at which these maps destabilized, we assume that:

$$T_p = A(n) + \rho(n) \tag{4.2}$$

where the pacemaker period is equal to the duration of the action potential plus the recovery time. We also assume that  $A(n+1) = f(\rho(n))$ —that is, the duration of the 'next' action potential, A(n+1), is a function of the amount of time the cell has had to recover,  $\rho(n)$ . By rearranging equation 4.2, we derive the following one-dimensional map:  $A(n+1)=f(T_p-A(n))$ , which has a unique fixed point that destabilizes at a particular  $T_p$  value, Fig. 4–7B. The map derived from the dynamics of the region above the obstacle (blue curve) destabilizes at  $T_p=0.57$  s, which corresponds with \*1 in Fig. 4–5, predicting the increase in the clockwise-rotating spirals. The map derived from the region below the obstacle (red curve) destabilizes at  $T_p=0.55$  s, which corresponds with \*2 in Fig. 4–5, predicting the increase in the counterclockwise-rotating spirals. Both  $T_p$  values predicted by the maps computed at these spatial locations are consistent with the pacemaker periods at which both regions destabilized, and thus are predictive of the increases in the number of clockwise-rotating and counterclockwise-rotating spiral waves as a function of  $T_p$ .

#### 4.6 Discussion

Here, we discovered that an asymmetry in the position of an obstacle with respect to a position of a pacing site in combination with the side pacing frequency determines spiral wave chirality for an isotropic cardiac medium. We used the slope of a map derived from an action potential duration restitution curve to provide insight into the transition in spiral wave chirality that we observed as a function of pacemaker period. The spiral wave forms as a consequence of propagation block (a necessary condition for initiation) taking place locally throughout the tissue. The value of the slope going below -1 is a correlative measure that we use to quantitatively describe how obstacle position changes the dynamics in local regions throughout the substrate. Recently, Gizzi et al. demonstrated that

the location of the pacing site gave rise to differences in the patterns of alternans observed in the right ventricles of canines [82]. Gizzi et al. also claimed that the intrinsic heterogeneities of the right ventricle accounted for the differences [82], which is consistent with the findings of our study. Studies have also addressed the role of obstacle shape in the context of electric-field-induced wave source initiation [66, 166, 18]. However, our study opens up a number of future research directions, which we outline in chapter 5. Our examination of the symmetry breaking properties and instabilities of this simplified cardiac system provide another example in which the geometry of the substrate plays a critical role in the determination of the system's asymptotic dynamics.

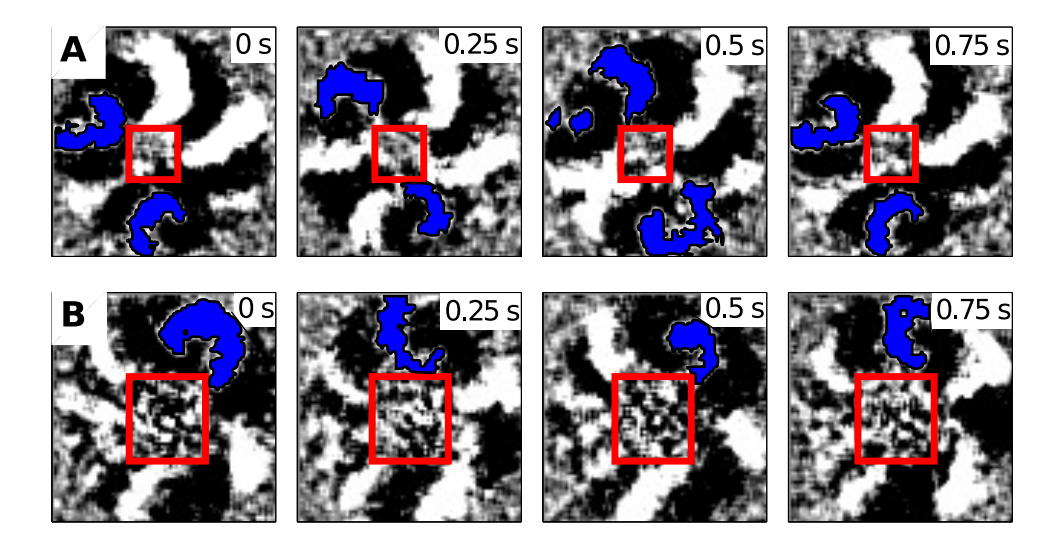


Figure 4–1: Spiral wave propagation in cardiac monolayers with inexcitable obstacles imaged using calcium sensitive dyes in embryonic chick heart cell monolayers. The red squares represent the position of the obstacles, the blue coloring represents the spiral wave, and the white coloring represents the waves emitted from the spiral waves. The diameter of the monolayer is 1 cm. (A) Two counterrotating spiral waves (at 10 and 6 o'clock) propagating in a cardiac monolayer with an obstacle width of 2 mm. The frames are separated by 0.25 s. (B) Counterclockwise-rotating spiral wave (at 1 o'clock) propagating in a cardiac monolayer with an obstacle width of 5 mm.

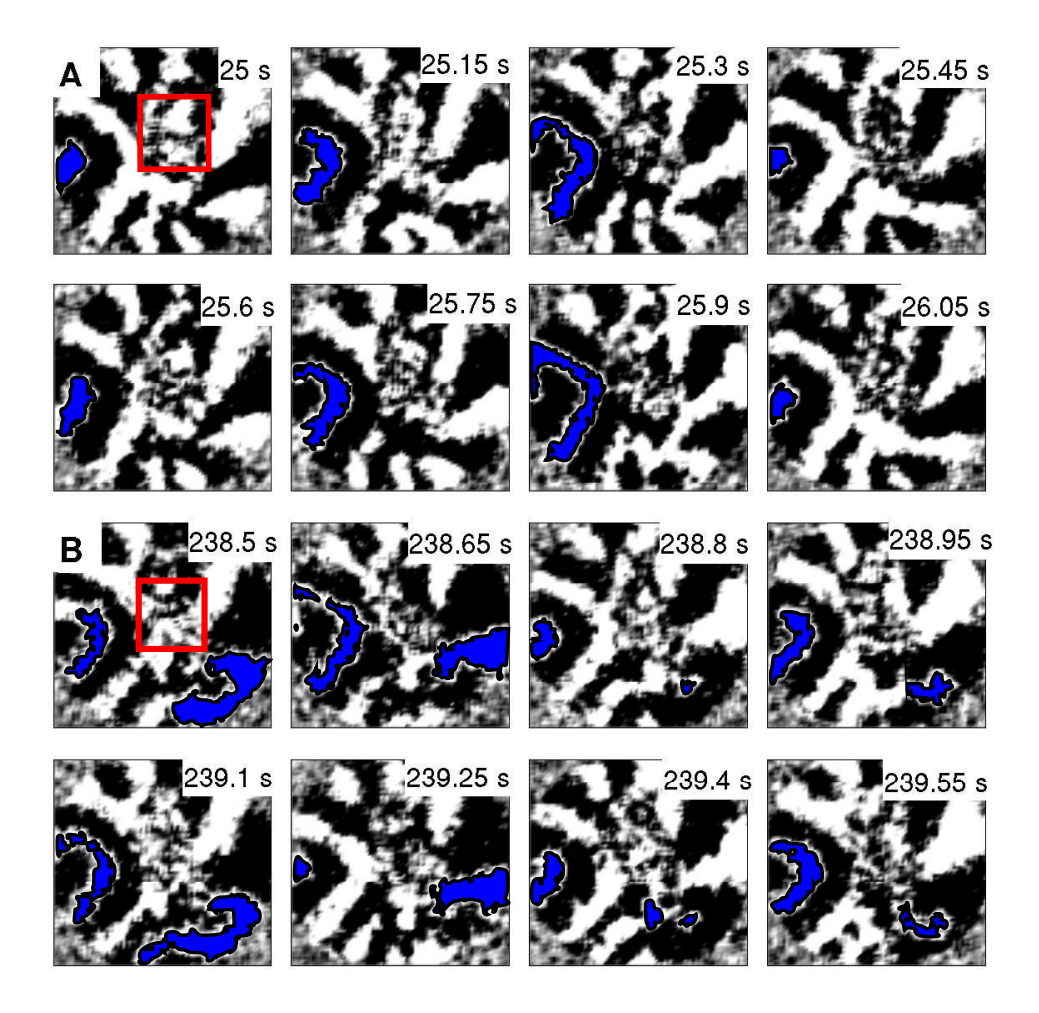


Figure 4–2: **Spiral wave initiation induced by rapid side pacing in a cardiac monolayer.** (A) A counterclockwise-rotating spiral wave on the left-hand side (in blue) emits wavefronts with a period of approximately 0.55 s. Wavefronts from the spiral wave propagate through the media and around the obstacle. The red rectangle represents the outline of the obstacle. The obstacle is positioned such that it is closer to the upper boundary with respect to the spiral wave on the left-hand side. (B) Three and a half minutes later, waves emitted from the spiral wave on the left-hand side detach from the obstacle and reenter, leading to the initiation of a counterclockwise-rotating spiral wave (in blue) on the right-hand side of the dish. The spiral wave has a period of approximately 0.65 s.

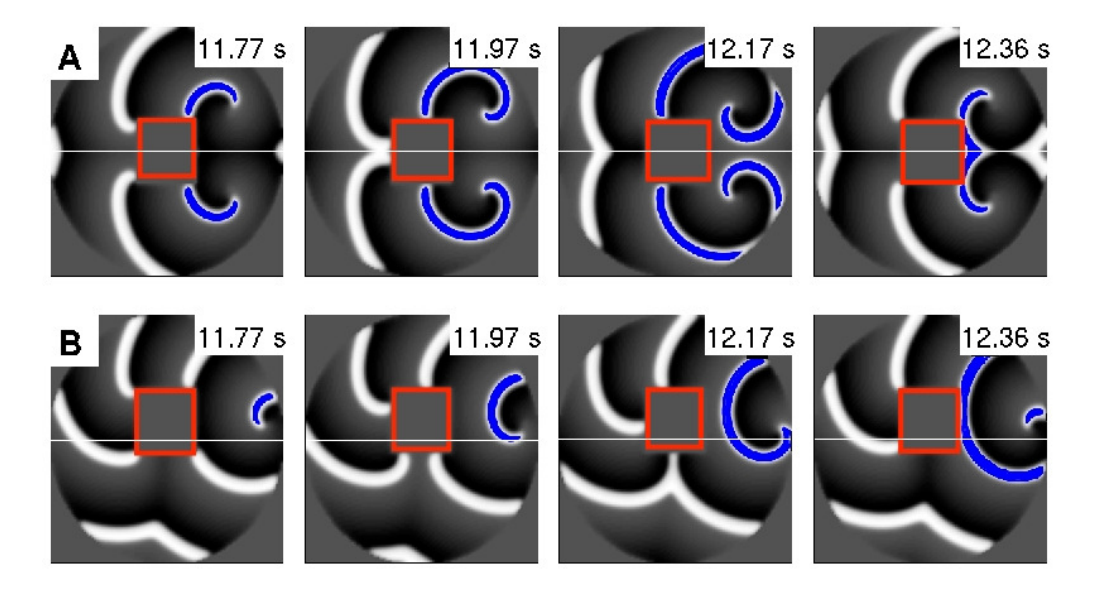


Figure 4–3: Spiral wave propagation in a mathematical model of the experiments. The red squares represent the position of the obstacles, the blue coloring represents the spiral waves, and the white coloring represents the waves emitted from the spiral waves. The white line is the axis of symmetry between the pacemaker and the obstacle. (A) Two counterrotating spiral waves are initiated following rapid pacing at  $T_p = 0.548$  s when the obstacle and the side pacemaker are symmetric. The times given in the top-right of each panel represent the time following the cessation of rapid pacing. (B) A counterclockwise-rotating spiral wave is generated following rapid pacing ( $T_p = 0.548$  s) when the obstacle is positioned upwards by 0.75 mm and pacing the tissue at  $T_p = 0.548$  s.

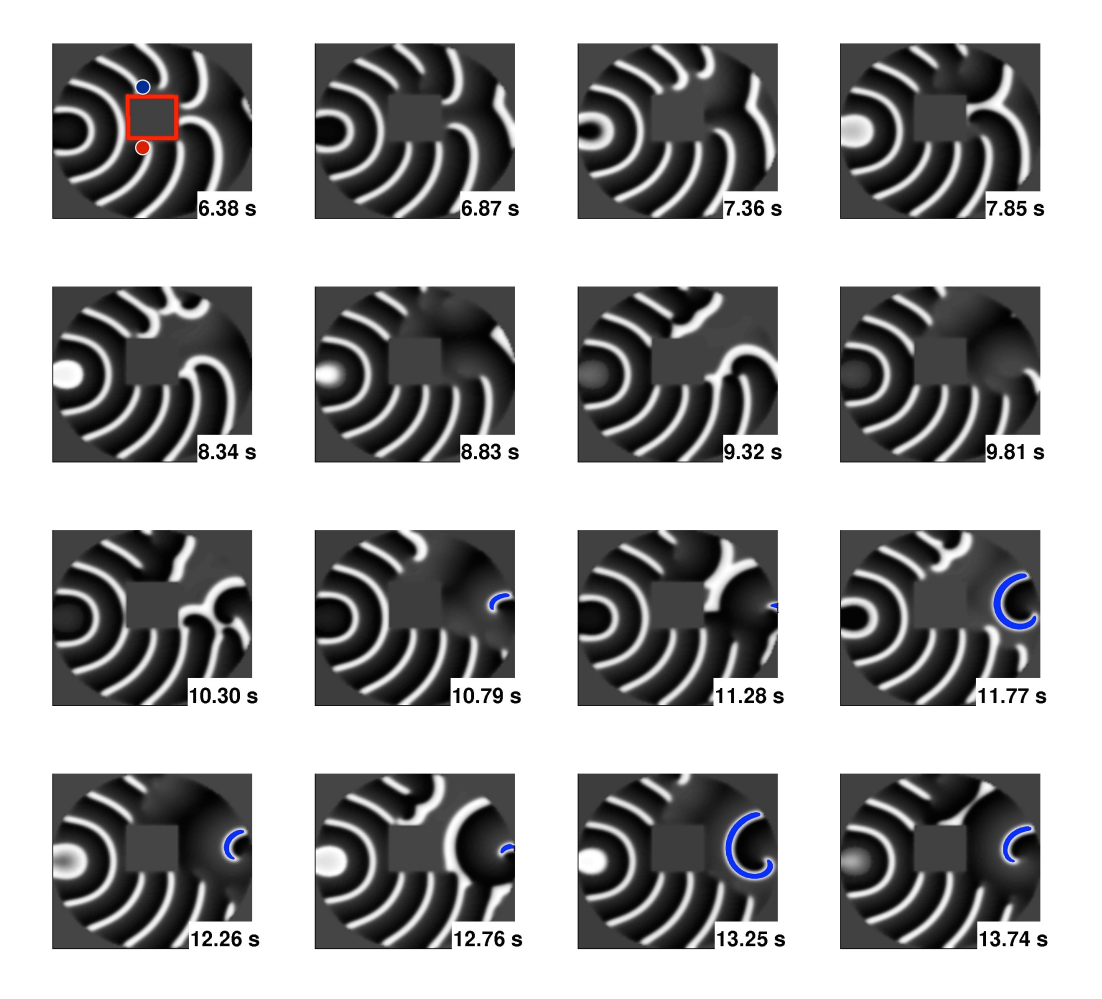


Figure 4–4: Spiral wave initiation induced by rapid side pacing in a mathematical model. Rapidly pacing the tissue ( $T_p = 0.548 \mathrm{\ s}$ ) from a pacemaker on the left-hand side leads to the initiation of a counterclockwise-rotating spiral wave. The red rectangle represents the location of the obstacle. The obstacle is positioned 0.75 mm closer to the upper boundary. The blue represents the spiral wave. The time in the bottom-right corner of each panel represents the time elapsed following the onset of rapid pacing. The blue and red dots above and below the obstacle—as shown in the top-left panel—represent the locations at which we computed the action potential duration restitution curves.

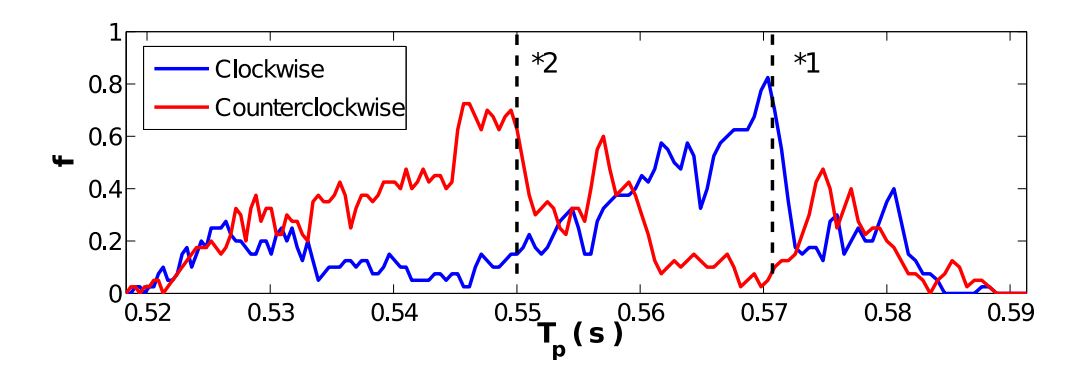


Figure 4–5: Spiral wave chirality as a function of the pacemaker period  $(T_p)$ . f represents the moving average of the fraction out of 20 from each category that was observed at each value of  $T_p$ . The obstacle was positioned above the central axis of symmetry by 0.75 mm. \*1 represents the  $T_p$  at which the map derived from the action potential duration (APD) restitution curve above the obstacle destabilized. \*2 represents the  $T_p$  at which the map from below the obstacle destabilized.

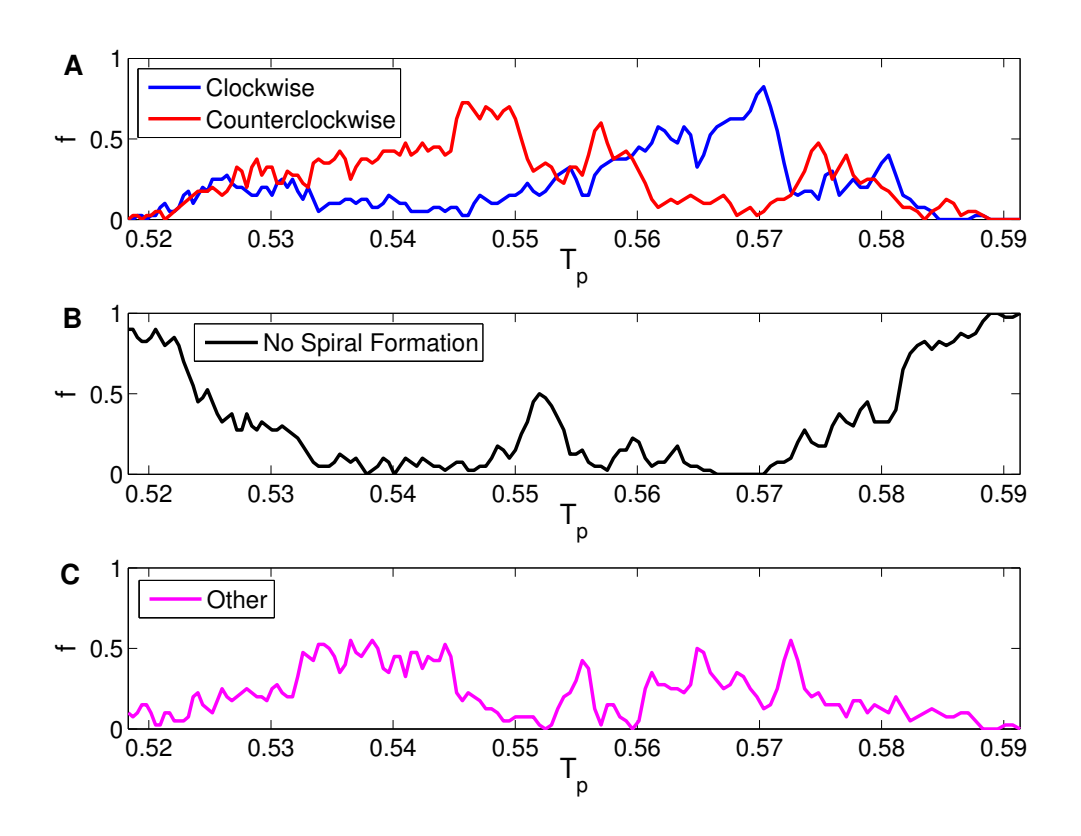


Figure 4–6: Spiral wave chirality as a function of pacemaker period  $(T_p)$  for all types of spiral wave behaviour. f represents the moving average of the fraction (out of 20) that gave rise to the spiral wave dynamic as given in the legend of each panel.  $T_p$  represents the pacemaker period in seconds. (A) This figure is the same as Fig. 4–5, and is included as a reference. Decreasing  $T_p$  leads to a change from clockwise-rotating spiral waves to counterclockwise-rotating spiral waves. (B) The moving average of the fraction of substrates that did not give rise to spiral waves was high at both high and low  $T_p$  values. At high values, the substrate, in general, supported the stable propagation of waves through the system. At low values, the pacing region transitioned from 1:1 propagation to 3:2 propagation (where, for ever 3 stimuli from the pacemaker, only 2 wavefronts propagated away from the pacing region and through the media). (C) The moving average of the fraction of substrates included in the 'other' spiral wave dynamic subsection. Opposite-chirality pairs of spiral waves, same-chirality pairs of spiral waves, and examples with 3 or more stably-rotating spiral waves were included.

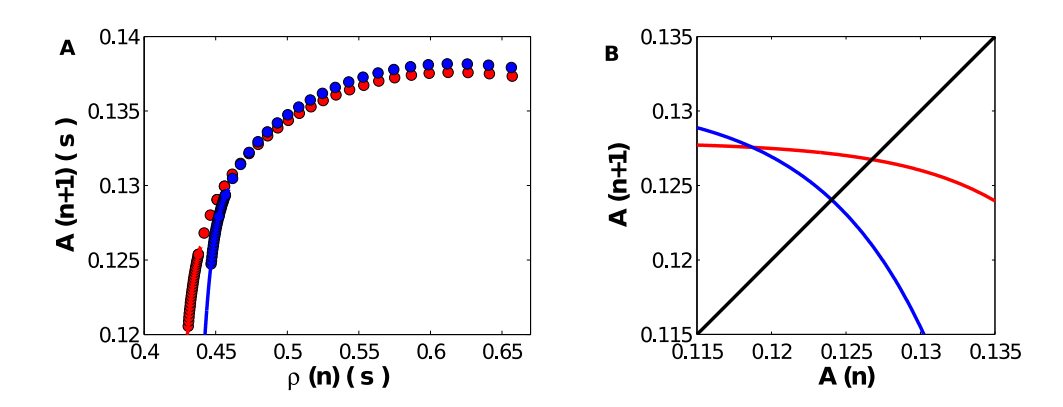


Figure 4–7: Instabilities in the action potential duration (APD) restitution curves at different spatial locations are consistent with the change in spiral wave chirality observed in Fig. 4–5. (A) APD is computed as a function of recovery time,  $\rho(n)$ , both above (blue) and below (red) the obstacle. The dots represent the steady-state APD computed numerically. The lines represent a nonlinear-least-squares regression fit to an exponential. (B) One-dimensional maps of APD at  $T_p = 0.57$  s are derived from the restitution curves computed both above (blue curve) and below (red curve) the obstacle. At  $T_p = 0.57$  s, the dynamics below the obstacle are stable because the absolute value of the slope through the fixed point is < 1, and the dynamics above the obstacle are unstable because the absolute value of the slope through the fixed point is > 1.

# CHAPTER 5 Conclusions and Future Directions

This thesis examined the dynamics associated with the onset of abnormal cardiac rhythms using simplified experimental models and nonlinear dynamics. In chapter 2, I focused on a set of experiments where treating spontaneously beating aggregates of cardiac cells with a potassium channel blocker led to the initiation of a spectrum of complex cardiac dynamics, including highly irregular rhythms. I examined these highly irregular rhythms, providing evidence that the dynamics were chaotic. Potassium channel blockade also led to the onset of alternating rhythms, a dynamic that can precede the onset of reentrant arrhythmias. In chapter 3, I developed a quantitative measure to anticipate the onset of the transition from a normal to alternating rhythm. To better understand the onset of abnormal cardiac rhythms in a spatially extended system, in chapter 4, I examined mechanisms of spiral wave initiation using calcium imaging of 1cm-diameter cardiac monolayers following the introduction of an inexcitable region and numerical simulations. In particular, I found that the location of the inexcitable region in combination with side pacemaker frequency governed spiral wave chirality preference. Furthermore, instabilities in the dynamics of the action potential duration in localized regions of the substrate preceded the onset of spiral wave activity. In this chapter, I wish to place the main points of my thesis (given

above) as well as other important findings from the studies which I believe merit discussion in a broader scientific context.

In chapter 2, I characterized irregular rhythms following potassium channel blockade as chaotic. As a consequence of a slowly varying parameter, the dynamics of a spontaneously beating aggregate composed of embryonic chick cardiac cells underwent a sequence of period-doubling bifurcations that gave rise to low-dimensional chaos. Indeed, the presence of irregular rhythms in the heart increases the likelihood of propagation block, which could lead to the initiation of serious reentrant cardiac arrhythmias. However, is there a dynamic difference between a chaotic rhythm or a rhythm driven by a noisy pacemaker? Assessing the functional relevance of chaotic cardiac rhythms represents a possible future research direction.

In chapter 3, I developed early warning signals based on data that was non-spatial. The heart's rhythm is set by the cardiac impulse that propagates in a nonlinear spatially-extended environment. The development of early warning signals in spatially-extended experimental cardiac systems, such as cardiac monolayers, represents an important future research question. Thus, the clinical relevance of the early warning signals developed here to predict the onset of T-wave alternans, for example, remains to be seen. That being said, this finding represents a strong first step towards the development of clinically-relevant early warning signals to predict the onset of abnormal cardiac rhythms in patients.

The mechanism underlying the increase in noise near the period-doubling bifurcation from a biological perspective remains unclear. Single ion channels open and close in a stochastic manner. Perhaps as more potassium channels are blocked—as the aggregate's dynamics approach the period-doubling bifurcation—the noise associated with the system amplifies. Furthermore, what is the biological mechanism underlying the alternating pattern? Potassium channel blockade leads to the prolongation of the action potential, which can lead to early afterdepolarizations, depolarizations that take place during the recovery phase of the action potential [195]. Early afterdepolarizations have been implicated in triggering the onset of cardiac arrhythmias [195, 216]. Because the beat patterns were collected using the motion of the aggregates, I could not provide insight into the biological mechanism. However, intracellular recordings of aggregates undergoing potassium channel blockade represents a future topic worth exploring.

To what extent is it possible to predict the future accurately? Studies have claimed that 'generic' early warning signals can provide insight into transitions in the qualitative dynamics of complex systems [180]. However, more recent work [49] has argued that there are limits on our ability to predict transitions in dynamics, claiming that it is only possible to predict future transitions if (1) the transition in dynamics takes place as a consequence of a bifurcation and (2) the control parameter goes through the bifurcation point on a slow time scale. If these requirements are met, then it is, in principle, possible to develop early warning signals. However, transitions in the dynamics of complex systems take place through a number of mechanisms, including noise-induced transitions, changes to the spatial structure of the system, and external perturbations leading to a change in the dynamics.

In chapter 4, I found that substrate geometry can govern spiral wave chirality ('rotation direction'). Chirality is a fundamental property of spiral waves alongside period and tip trajectory—and yet our study represents one of the first forays into developing a broader understanding of spiral wave chirality preference. In particular, my study opens up many research directions, including how obstacle size, obstacle shape, model parameters controlling tissue excitability, and fiber orientation influence spiral wave chirality. To numerically simulate the system composed of a side pacemaker and an inexcitable region, I used a generic model of excitable media, the FitzHugh-Nagumo equations. An open question remains: to what extent do these results related to spiral wave chirality preference extend to higher-dimensional Hodgkin-Huxley-style ionic models of the cardiac action potential? Experimental confirmation of the theoretical prediction represents an important research trajectory as well. From a clinical perspective, spiral waves propagating in excitable media are believed to play an important role in the genesis of many serious cardiac arrhythmias, though not much attention has focused on the chiral nature of spiral waves. However, the chirality of one arrhythmia, atrial flutter, is clinically relevant, and the direction of circulation of excitation waves in the right atrium is typically classified as either clockwise or counterclockwise [176].

The heart has a complicated geometry: wavefronts propagate through heterogeneous tissue, colliding with inexcitable barriers in three spatial dimensions. Recent studies have analyzed the effects of changing the cardiac geometry using realistic three-dimensional numerical models [170, 197]. The study from chapter

4 demonstrates a clear example of how the geometry can influence the dynamics. Furthermore, from a clinical standpoint, changes to the heart's geometry significantly influence the dynamics: a myocardial infarction increases the likelihood of sudden cardiac death. (Myocardial infarctions also give rise to complicated spatially inhomogeneous effects on the heart's electrophysiology, which can increase the likelihood of sudden cardiac death [8].) Other cardiac dynamics studies have included effects of geometry [44, 38, 159, 189], but much work remains to be done.

Instabilities in the dynamics of cardiac systems can precede propagation block, which can lead to reentry and the establishment of spiral waves. Increasing the stimulation frequency can induce alternating rhythms, often associated with period-doubling bifurcations, which can act as precursors of reentry [160]. Furthermore, experiments of circulating pulses of excitation in rings of cardiac tissue have demonstrated that instabilities in the beat-to-beat patterns can precede propagation block [75]. Larger fluctuations in the magnitude of successive action potential durations increases the likelihood of propagation block, but many questions related to the mechanism of this process remain. Quantifying the maximum difference in amplitude of successive alternating action potential durations that various cardiac systems (with different geometries) can sustain represents a future research question.

Transitions take place in the dynamics of the heart with serious consequences.

Combining simplified experimental models with tools from nonlinear dynamics represents a powerful approach to unearth the mechanistic properties of these

transitions, and to provide insight that could potentially guide future therapeutic strategies.

## Appendix A: Ionic model

This appendix describes the equations of the ionic model that were used for the theoretical computations in chapter 2. This ionic model was initially presented in Kim et al. [117]; however, the parameter values used in the earlier study did not give rise to chaotic dynamics. To obtain chaotic dynamics we decreased the conductances of the slowly activating potassium current and the inward calcium current. Relatively, the sodium current plays a greater role in the new parameter regime, and this enabled the model to generate the bursting and chaotic dynamics when the  $g_{Kr}$  parameter is decreased. We adapt equations developed by Kowtha et al. to model the embryonic chick heart cell preparation [122]:

$$\dot{V} = -I_{tot}(V)/C_i,\tag{5.1}$$

where the V is the membrane voltage,  $I_{tot}$  is the total current density and  $C_i$  is the capacitance.  $I_{tot}$  is a sum of the different ionic component currents so that,

$$I_{tot} = I_{Na} + I_{Ks} + I_{Kr} + I_{K1} + I_{Ca} + I_b + I_f$$
(5.2)

where  $I_{Na}$  is the sodium current,  $I_{Ca}$  is the calcium current,  $I_b$  is the background current,  $I_f$  is a depolarizing current, and  $I_{Ks}$ ,  $I_{Kr}$ , and  $I_{K1}$  are three potassium currents. The magnitude of each of these currents depends on membrane voltage, ionic concentrations, and time. We describe each current in turn. We use standard notation in which  $g_w$  is the conductance of ionic current w,  $E_w$  is the equilibrium potential of ion w. Following the original notation of Hodgkin-Huxley, terms entering the time and voltage dependent currents are written in two equivalent forms. For component x, we have,

$$\dot{x}(t) = (x_{\infty}(V) - x(t))/\tau_x(V), \text{ or}$$

$$\dot{x}(t) = \alpha_x(V) - (\alpha_x(V) + \beta_x(V))x(t)$$

so that

$$x_{\infty}(V) = \frac{\alpha_x(V)}{\alpha_x(V) + \beta_x(V)}, \quad \tau_x(V) = \frac{1}{\alpha_x(V) + \beta_x(V)}$$

$$(5.3)$$

Sodium current

$$I_{Na} = g_{Na} \ m(t)^3 h(t) j(t) (V - E_{Na}), \tag{5.4}$$

where,

$$\dot{m}(t) = (m_{\infty}(V) - m(t))/\tau_m(V) \tag{5.5}$$

$$\dot{h}(t) = (h_{\infty}(V) - h(t))/\tau_h(V)$$
 (5.6)

$$\dot{j}(t) = (j_{\infty}(V) - j(t))/\tau_{i}(V) \tag{5.7}$$

and

$$\alpha_{m} = \frac{320 (V + 47.13)}{1 - \exp^{-0.1(V + 47.13)}}$$

$$\beta_{m} = 80 \exp^{-V/11}$$

$$\alpha_{h} = 2/3 \times [135 \exp^{-(V + 80)/6.8}(1 - STEP(V + 40))]$$

$$\beta_{h} = 2/3 \times [(3560 \exp^{0.079V} + 3.1 \times 10^{8} \exp^{0.35V})(1 - STEP(V + 40))$$

$$+ \frac{1}{0.00013 (\exp^{-(V + 10.66)/11.1} + 1)} STEP(V + 40)]$$

$$\alpha_{j} = (V + 37.78) \times \frac{-1.2714 \times 10^{8} \exp^{0.2444V} - 3.474 \times 10^{-2} \exp^{-0.04391V}}{1 + \exp^{0.311(V + 79.23)}}$$

$$\times (1 - STEP(V + 40))$$

$$\beta_{j} = \frac{121.1 \exp^{-0.01052V}}{1 + \exp^{-0.1378(V + 40.14)}}(1 - STEP(V + 40))$$

$$+ \frac{300 \exp^{-2.535 \times 10^{-7}V}}{1 + \exp^{-0.1(V + 32)}} STEP(V + 40)$$

Potassium currents

Slow potassium current

$$I_{Ks} = g_{Ks} \ n(t)(V - E_{Ks}),$$
 (5.8)

where

$$\dot{n}(t) = (n_{\infty}(V) - n(t))/\tau_n(V), \tag{5.9}$$

and

$$\alpha_n = 2/3 \times \frac{0.08 (V - 15)}{1 - \exp^{-0.08(V - 15)}}$$
  
 $\beta_n = 2/3 \times 0.156 \exp^{-0.055(V - 15)}$ .

Rapid potassium current

$$I_{Kr} = \frac{g_{Kr}s(t) \ y_0^2(145P_{Kr} - 1.3R_{Kr})}{1 + y_0 + 52.8y_0^2}$$
 (5.10)

where

$$\dot{s}(t) = (s_{\infty}(V) - s(t)) / \tau_s(V) \tag{5.11}$$

and

$$\alpha_s = 18.4 \exp^{0.12 (V+12)}$$

$$\beta_s = 0.0288 \exp^{-0.09 (V+12)}$$

Inward rectifier potassium current

$$I_{K1} = \frac{g_{K11} \ y_1^3 (145 P_{Kr} - 1.5 R_{Kr})}{1 + y_1 + y_1^2 + 1.5 y_1^3} + \frac{g_{K12} \ |V + 65| y_2^2 (145 P_{Kr} - 10.7 R_{Kr})}{1 + y_2 + 9 y_2^2}$$
 (5.12)

where

$$R_{Kr} = \frac{1.0}{1 + \exp(V/25)}, \quad P_{Kr} = 1 - R_{Kr}$$
  
 $y_0 = \frac{1.3R_{Kr}}{145P_{Kr}}, \quad y_1 = \frac{1.5R_{Kr}}{145P_{Kr}}, \quad y_2 = \frac{10.7R_{Kr}}{145P_{Kr}}$ 

Calcium current

$$I_{Ca} = g_{Ca} \ d(t) f(t) g(t) (V - E_{Ca}) \tag{5.13}$$

where

$$\dot{d}(t) = (d_{\infty}(V) - d(t)) / \tau_d(V)$$
(5.14)

$$\dot{f}(t) = (f_{\infty}(V) - f(t))/\tau_f(V)$$
 (5.15)

$$\dot{g}(t) = (g_{\infty}(V) - g(t))/\tau_g(V)$$
 (5.16)

$$[\dot{C}a] = -13 \times 10^{-6} I_{Ca}(V) + 80(10^{-7} - [Ca])$$
 (5.17)

and

$$d_{\infty} = \frac{1}{1 + \exp^{-(V+10)/6.24}}$$

$$\tau_d = d_{\infty} \times \frac{1 - \exp^{-(V+10)/6.24}}{35 (V+10)}$$

$$f_{\infty} = \frac{1}{1 + \exp^{(V+28)/6.9}}$$

$$\tau_f = \frac{1}{19.7 \exp^{-(0.0337(V+10))^2 + 20}}$$

$$g_{\infty} = \frac{1}{1 + [Ca]/(3.5 \times 10^{-7})}$$

$$\tau_g = 0.002$$

Pacemaker current

$$I_f = g_f \ p(t)(V - E_f)$$
 (5.18)

where

$$\alpha_p = 0.095 \exp^{-0.075(V+62)}$$
 (5.19)

$$\alpha_p = 0.095 \exp^{-0.075(V+62)}$$

$$\beta_p = \frac{1.05 (V+62)}{1 - \exp^{-0.2(V+62)}}$$
(5.19)

Background current

$$I_b = g_b \left( V - E_b \right) \tag{5.21}$$

The numerical values of the different parameters are:

$$C_i = 1 \, \mu \text{F/cm}^2$$

$$g_{Na} = 1500 \text{ mS/cm}^2$$

$$g_{Ks} = 1.2546 \text{ mS/cm}^2$$

$$g_b = 0.093 \text{ mS/cm}^2$$

$$g_{K11} = 409.5 \text{ mS/cm}^2$$

$$g_{K12} = 1.476 \text{ mS/cm}^2$$

$$g_{Ca} = 55.0 \text{ mS/cm}^2$$

$$g_f = 0.03 \text{ mS/cm}^2$$

$$E_{Na} = 40.0 \text{ mV}$$

$$E_{Ks} = -100.0 \text{ mV}$$

$$E_b = 40.0 \text{ mV}$$

$$E_{Ca} = 40.0 \text{ mV}$$

$$E_f = -30 \text{ mV}$$

$$dt = 50 \,\mu\mathrm{s}$$

## References

- [1] K Agladze and P De Kepper. Influence of electric field on rotating spiral waves in the Belousov-Zhabotinskii reaction. *J. Phys. Chem.*, 96(13):5239–5242, 1992.
- [2] K Agladze, MW Kay, V Krinsky, and N Sarvazyan. Interaction between spiral and paced waves in cardiac tissue. *Am. J. Physiol.-Heart C.*, 293(1):H503–H513, 2007.
- [3] K Aihara, G Matsumoto, and M Ichikawa. An alternating periodic-chaotic sequence observed in neural oscillators. *Phys. Lett. A*, 111(5):251–255, 1985.
- [4] MA Allessie, FI Bonke, and FJ Schopman. Circus movement in rabbit atrial muscle as a mechanism of tachycardia. II. The role of nonuniform recovery of excitability in the occurrence of unidirectional block, as studied with multiple microelectrodes. *Circ. Res.*, 39(2):168–177, 1976.
- [5] S Alonso and M Bär. Reentry near the percolation threshold in a heterogeneous discrete model for cardiac tissue. *Phys. Rev. Lett.*, 110(15):158101, 2013.
- [6] S Alonso, F Sagués, and AS Mikhailov. Taming winfree turbulence of scroll waves in excitable media. *Science*, 299(5613):1722–1725, 2003.
- [7] C Antzelevitch and A Burashnikov. Overview of basic mechanisms of cardiac arrhythmia. *Cardiac Electrophysiol. Clin.*, 3(1):23–45, 2011.
- [8] H Arce, A Xu, H González, and MR Guevara. Alternans and higher-order rhythms in an ionic model of a sheet of ischemic ventricular muscle. *Chaos*, 10(2):411–426, 2000.
- [9] Y Asano, JM Davidenko, WT Baxter, RA Gray, and J Jalife. Optical mapping of drug-induced polymorphic arrhythmias and torsade de pointes in the isolated rabbit heart. *J. Am. Coll. Cardiol.*, 29(4):831–842, 1997.

- [10] DS Auerbach, KR Gryzda, PB Furspan, PY Sato, S Mironov, and J Jalife. Structural heterogeneity promotes triggered activity, reflection and arrhythmogenesis in cardiomyocyte monolayers. J. Physiol., 589(9):2363–2381, 2011.
- [11] P Bak, K Chen, and C Tang. A forest-fire model and some thoughts on turbulence. *Phys. Lett. A*, 147(5):297–300, 1990.
- [12] A Bardou, S Achour, P Auger, and J-L Chassé. Effects of local ischemia and transient conduction blocks on the induction of cardiac reentries. *Int. J. Bifurcat. Chaos*, 6(09):1657–1664, 1996.
- [13] J Beaumont, N Davidenko, JM Davidenko, and J Jalife. Spiral waves in two-dimensional models of ventricular muscle: formation of a stationary core. *Biophys. J.*, 75(1):1–14, 1998.
- [14] O Bernus, CW Zemlin, RM Zaritsky, SF Mironov, and AM Pertsov. Alternating conduction in the ischaemic border zone as precursor of reentrant arrhythmias: a simulation study. *Europace*, 7(s2):S93–S104, 2005.
- [15] A Beuter and K Vasilakos. Tremor: Is Parkinson's disease a dynamical disease? *Chaos*, 5(1):35–42, 1995.
- [16] VN Biktashev and AV Holden. Resonant drift of autowave vortices in two dimensions and the effects of boundaries and inhomogeneities. *Chaos Soliton. Fract.*, 5(3):575–622, 1995.
- [17] Y Biton, A Rabinovitch, I Aviram, and D Braunstein. Two mechanisms of spiral-pair-source creation in excitable media. *Phys. Lett. A*, 373(20):1762– 1767, 2009.
- [18] P Bittihn, M Hörning, and S Luther. Negative curvature boundaries as wave emitting sites for the control of biological excitable media. *Phys. Rev. Lett.*, 109(11):118106, 2012.
- [19] C Boettiger and A Hastings. Quantifying limits to detection of early warning for critical transitions. J. R. Soc. Interface, 9(75):2527–2539, 2012.
- [20] VE Bondarenko, GP Szigeti, GCL Bett, S-J Kim, and L Rasmusson. Computer model of action potential of mouse ventricular myocytes. *Am. J. Physiol.-Heart C.*, 287(3):H1378–H1403, 2004.

- [21] B Borek, TK Shajahan, J Gabriels, A Hodge, L Glass, and A Shrier. Pacemaker interactions induce reentrant wave dynamics in engineered cardiac culture. *Chaos*, 22(3):033132, 2012.
- [22] G Bub, L Glass, NG Publicover, and A Shrier. Bursting calcium rotors in cultured cardiac myocyte monolayers. Proc. Natl. Acad. Sci. USA, 95(17):10283-10287, 1998.
- [23] G Bub and A Shrier. Propagation through heterogeneous substrates in simple excitable media models. *Chaos*, 12(3):747–753, 2002.
- [24] G Bub, A Shrier, and L Glass. Spiral wave generation in heterogeneous excitable media. *Phys. Rev. Lett.*, 88(5):058101, 2002.
- [25] G Bub, A Shrier, and L Glass. Global organization of dynamics in oscillatory heterogeneous excitable media. *Phys. Rev. Lett.*, 94(2):028105, 2005.
- [26] A Burashnikov and C Antzelevitch. Late-phase 3 EAD. a unique mechanism contributing to initiation of atrial fibrillation. *Pace*, 29(3):290–295, 2006.
- [27] N Bursac, F Aguel, and L Tung. Multiarm spirals in a two-dimensional cardiac substrate. *Proc. Natl. Acad. Sci. USA*, 101(43):15530–15534, 2004.
- [28] C Cabo, AM Pertsov, WT Baxter, JM Davidenko, RA Gray, and J Jalife. Wave-front curvature as a cause of slow conduction and block in isolated cardiac muscle. *Circ. Res.*, 75(6):1014–1028, 1994.
- [29] H Calkins, KH Kuck, R Cappato, J Brugada, AJ Camm, S-A Chen, HJG Crijns, RJ Damiano, DW Davies, J DiMarco, et al. 2012 HRS/EHRA/ECAS Expert Consensus Statement on Catheter and Surgical Ablation of Atrial Fibrillation: Recommendations for Patient Selection, Procedural Techniques, Patient Management and Follow-up, Definitions, Endpoints, and Research Trial Design. *Europace*, page eus027, 2012.
- [30] J-M Cao, Z Qu, Y-H Kim, T-J Wu, A Garfinkel, JN Weiss, HS Karagueuzian, and P-S Chen. Spatiotemporal heterogeneity in the induction of ventricular fibrillation by rapid pacing importance of cardiac restitution properties. *Circ. Res.*, 84(11):1318–1331, 1999.
- [31] SR Carpenter and WA Brock. Rising variance: a leading indicator of ecological transition. *Ecol. Lett.*, 9(3):311–318, 2006.

- [32] MG Chang, CY Chang, E de Lange, L Xu, R O'Rourke, HS Karagueuzian, L Tung, E Marbán, A Garfinkel, JN Weiss, et al. Dynamics of early afterdepolarization-mediated triggered activity in cardiac monolayers. Biophys. J., 102(12):2706–2714, 2012.
- [33] TR Chay. Abnormal discharges and chaos in a neuronal model system. *Biol Cybern.*, 50(4):301–311, 1984.
- [34] TR Chay, YS Fan, and YS Lee. Bursting, spiking, chaos, fractals, and universality in biological rhythms. *Int. J. Bifurcat. Chaos*, 5(03):595–635, 1995.
- [35] J-X Chen, H Zhang, and Y-Q Li. Drift of spiral waves controlled by a polarized electric field. *J. Chem. Phys.*, 124(1):014505, 2006.
- [36] P-S Chen, PD Wolf, EG Dixon, ND Danieley, DW Frazier, WM Smith, and RE Ideker. Mechanism of ventricular vulnerability to single premature stimuli in open-chest dogs. *Circ. Res.*, 62(6):1191–1209, 1988.
- [37] EM Cherry and FH Fenton. A tale of two dogs: analyzing two models of canine ventricular electrophysiology. Am. J. Physiol.-Heart C., 292(1):H43– H55, 2007.
- [38] EM Cherry and FH Fenton. Effects of boundaries and geometry on the spatial distribution of action potential duration in cardiac tissue. *J. Theor. Biol.*, 285(1):164–176, 2011.
- [39] DR Chialvo, RF Gilmour Jr, and J Jalife. Low dimensional chaos in cardiac tissue. *Nature*, 343(6259):653–657, 1990.
- [40] T Chow, DJ Kereiakes, J Onufer, A Woelfel, S Gursoy, BJ Peterson, ML Brown, W Pu, and DG Benditt. Does microvolt T-wave alternans testing predict ventricular tachyarrhythmias in patients with ischemic cardiomyopathy and prophylactic defibrillators?: The MASTER (Microvolt T Wave Alternans Testing for Risk Stratification of Post-Myocardial Infarction Patients) trial. J. Am. Coll. Cardiol., 52(20):1607–1615, 2008.
- [41] DJ Christini, ML Riccio, CA Culianu, JJ Fox, A Karma, and RF Gilmour Jr. Control of electrical alternans in canine cardiac Purkinje fibers. *Phys. Rev. Lett.*, 96(10):104101, 2006.

- [42] JR Clay, AS Kristof, J Shenasa, RM Brochu, and A Shrier. A review of the effects of three cardioactive agents on the electrical activity from embryonic chick heart cell aggregates: TTX, ACh, and E-4031. *Prog. Biophys. Mol. Biol.*, 62(3):185–202, 1994.
- [43] RH Clayton and AV Holden. Dispersion of cardiac action potential duration and the initiation of re-entry: a computational study. *Biomed. Eng. Online*, 4(1):11, 2005.
- [44] M Courtemanche, L Glass, and JP Keener. Instabilities of a propagating pulse in a ring of excitable media. *Phys. Rev. Lett.*, 70(14):2182, 1993.
- [45] M Courtemanche, JP Keener, and L Glass. A delay equation representation of pulse circulation on a ring in excitable media. SIAM J. Appl. Math., 56(1):119–142, 1996.
- [46] L Dai, KS Korolev, and J Gore. Slower recovery in space before collapse of connected populations. *Nature*, 496(7445):355–358, 2013.
- [47] L Dai, D Vorselen, KS Korolev, and J Gore. Generic indicators for loss of resilience before a tipping point leading to population collapse. *Science*, 336(6085):1175–1177, 2012.
- [48] V Dakos and J Bascompte. Critical slowing down as early warning for the onset of collapse in mutualistic communities. *Proc. Natl. Acad. Sci. USA*, 111(49):17546–17551, 2014.
- [49] V Dakos, SR Carpenter, EH van Nes, and M Scheffer. Resilience indicators: prospects and limitations for early warnings of regime shifts. *Philos. T. Roy.* Soc. B, 370(1659):20130263, 2015.
- [50] V Dakos, M Scheffer, EH van Nes, V Brovkin, V Petoukhov, and H Held. Slowing down as an early warning signal for abrupt climate change. Proc. Natl. Acad. Sci. USA, 105(38):14308–14312, 2008.
- [51] JM Davidenko. Spiral wave activity: a possible common mechanism for polymorphic and monomorphic ventricular tachycardias. *J. Cardiovasc. Electrophysiol.*, 4(6):730–746, 1993.
- [52] JM Davidenko, AV Pertsov, R Salomonsz, W Baxter, and J Jalife. Stationary and drifting spiral waves of excitation in isolated cardiac muscle. *Nature*, 1992.

- [53] RL DeHaan. Regulation of spontaneous activity and growth of embryonic chick heart cells in tissue culture. *Dev Biol*, 16(3):216–249, 1967.
- [54] RL Dehaan and HA Fozzard. Membrane response to current pulses in spheroidal aggregates of embryonic heart cells. *J. Gen. Physiol.*, 65(2):207–222, 1975.
- [55] RL DeHaan and SH Gottlieb. The electrical activity of embryonic chick heart cells isolated in tissue culture singly or in interconnected cell sheets. J. Gen. Physiol., 52(4):643–665, 1968.
- [56] PD Ditlevsen and SJ Johnsen. Tipping points: early warning and wishful thinking. *Geophys. Res. Lett.*, 37(19), 2010.
- [57] E Drouin, G Lande, and F Charpentier. Amiodarone reduces transmural heterogeneity of repolarization in the human heart. *J. Am. Coll. Cardiol.*, 32(4):1063–1067, 1998.
- [58] B Echebarria and A Karma. Instability and spatiotemporal dynamics of alternans in paced cardiac tissue. *Phys. Rev. Lett.*, 88(20):208101, 2002.
- [59] B Echebarria and A Karma. Amplitude equation approach to spatiotemporal dynamics of cardiac alternans. *Phys. Rev. E*, 76(5):051911, 2007.
- [60] N El-Sherif, M Chinushi, EB Caref, and M Restivo. Electrophysiological mechanism of the characteristic electrocardiographic morphology of Torsade de Pointes tachyarrhythmias in the long-QT syndrome detailed analysis of ventricular tridimensional activation patterns. *Circulation*, 96(12):4392–4399, 1997.
- [61] EA Ermakova and AM Pertsov. Interaction of rotating spiral waves with a boundary. *Biofizika*, 31(5):855–861, 1986.
- [62] EA Ermakova, AM Pertsov, and EE Shnol. On the interaction of vortices in two-dimensional active media. *Physica D*, 40(2):185–195, 1989.
- [63] Y-S Fan and TR Chay. Generation of periodic and chaotic bursting in an excitable cell model. *Biol Cybern.*, 71(5):417–431, 1994.
- [64] VG Fast and AG Kléber. Cardiac tissue geometry as a determinant of unidirectional conduction block: assessment of microscopic excitation spread

- by optical mapping in patterned cell cultures and in a computer model. *Cardiovasc. Res.*, 29(5):697–707, 1995.
- [65] VG Fast and AG Kléber. Role of wavefront curvature in propagation of cardiac impulse. *Cardiovasc. Res.*, 33(2):258–271, 1997.
- [66] VG Fast, S Rohr, AM Gillis, and AG Kléber. Activation of cardiac tissue by extracellular electrical shocks: Formation of secondary sources at intercellular clefts in monolayers of cultured myocytes. Circ. Res., 82(3):375–385, 1998.
- [67] FH Fenton and EM Cherry. Models of cardiac cell. *Scholarpedia*, 3(8):1868, 2008.
- [68] FH Fenton, EM Cherry, HM Hastings, and SJ Evans. Multiple mechanisms of spiral wave breakup in a model of cardiac electrical activity. *Chaos*, 12(3):852–892, 2002.
- [69] FH Fenton, EM Cherry, and BG Kornreich. Termination of equine atrial fibrillation by quinidine: an optical mapping study. *J. Vet. Cardiol.*, 10(2):87–103, 2008.
- [70] FH Fenton, A Gizzi, C Cherubini, N Pomella, and S Filippi. Role of temperature on nonlinear cardiac dynamics. *Phys. Rev. E*, 87(4):042717, 2013.
- [71] FH Fenton, S Luther, EM Cherry, NF Otani, V Krinsky, A Pumir, E Bodenschatz, and RF Gilmour. Termination of atrial fibrillation using pulsed low-energy far-field stimulation. *Circulation*, 120(6):467–476, 2009.
- [72] B Fermini and AA Fossa. The impact of drug-induced QT interval prolongation on drug discovery and development. *Nat. Rev. Drug Discov.*, 2(6):439–447, 2003.
- [73] R FitzHugh. Impulses and physiological states in theoretical models of nerve membrane. *Biophys. J.*, 1(6):445, 1961.
- [74] JJ Fox, ML Riccio, F Hua, E Bodenschatz, and RF Gilmour. Spatiotemporal transition to conduction block in canine ventricle. *Circ. Res.*, 90(3):289–296, 2002.

- [75] LH Frame and MB Simson. Oscillations of conduction, action potential duration, and refractoriness. A mechanism for spontaneous termination of reentrant tachycardias. *Circulation*, 78(5):1277–1287, 1988.
- [76] DW Frazier, PD Wolf, JM Wharton, AS Tang, WM Smith, and RE Ideker. Stimulus-induced critical point. Mechanism for electrical initiation of reentry in normal canine myocardium. J. Clin. Invest., 83(3):1039, 1989.
- [77] SA Gaeta, G Bub, GW Abbott, and DJ Christini. Dynamical mechanism for subcellular alternans in cardiac myocytes. *Circ. Res.*, 105(4):335–342, 2009.
- [78] A Garfinkel, Y-H Kim, O Voroshilovsky, Z Qu, JR Kil, M-H Lee, HS Karagueuzian, JN Weiss, and P-S Chen. Preventing ventricular fibrillation by flattening cardiac restitution. *Proc. Natl. Acad. Sci. USA*, 97(11):6061–6066, 2000.
- [79] A Garfinkel, ML Spano, WL Ditto, and JN Weiss. Controlling cardiac chaos. *Science*, 257(5074):1230–1235, 1992.
- [80] WH Gaskell. The Croonian Lecture: On the rhythm of the heart of the frog, and on the nature of the action of the vagus nerve. *Philos. T. R. Soc. Lond.*, 173:993–1033, 1882.
- [81] M Gerhardt, H Schuster, and JJ Tyson. A cellular automaton model of excitable media including curvature and dispersion. *Science*, 247(4950):1563– 1566, 1990.
- [82] A Gizzi, EM Cherry, RF Gilmour Jr, S Luther, S Filippi, and FH Fenton. Effects of pacing site and stimulation history on alternans dynamics and the development of complex spatiotemporal patterns in cardiac tissue. *Front. Physiol.*, 4, 2013.
- [83] M Gladwell. The tipping point: How little things can make a big difference. Little, Brown, 2006.
- [84] L Glass. Introduction to controversial topics in nonlinear science: Is the normal heart rate chaotic? *Chaos*, 19(2):028501, 2009.
- [85] L Glass and ME Josephson. Resetting and annihilation of reentrant abnormally rapid heartbeat. *Phys. Rev. Lett.*, 75(10):2059, 1995.

- [86] L Glass and MC Mackey. Pathological conditions resulting from instabilities in physiological control systems. Ann. NY. Acad. Sci., 316(1):214–235, 1979.
- [87] RA Gray, J Jalife, A Panfilov, WT Baxter, C Cabo, JM Davidenko, and AM Pertsov. Nonstationary vortexlike reentrant activity as a mechanism of polymorphic ventricular tachycardia in the isolated rabbit heart. *Circulation*, 91(9):2454–2469, 1995.
- [88] MR Guevara, L Glass, and A Shrier. Phase locking, period-doubling bifurcations, and irregular dynamics in periodically stimulated cardiac cells. *Science*, 214:1350–1353, 1981.
- [89] MR Guevara, A Shrier, and L Glass. Phase resetting of spontaneously beating embryonic ventricular heart cell aggregates. Am. J. Physiol.-Heart C., 251(6):H1298–H1305, 1986.
- [90] MR Guevara, A Shrier, and L Glass. Phase-locked rhythms in periodically stimulated heart cell aggregates. Am. J. Physiol.-Heart C., 254(1):H1-H10, 1988.
- [91] MR Guevara, G Ward, A Shrier, and L Glass. Electrical alternans and period doubling bifurcations. *IEEE Comp. Cardiol.*, 562:167–170, 1984.
- [92] K Hall and L Glass. How to tell a target from a spiral: the two probe problem. *Phys. Rev. Lett.*, 82(25):5164–5167, 1999.
- [93] MS Hanna, J Coromilas, ME Josephson, AL Wit, and NS Peters. Mechanisms of resetting reentrant circuits in canine ventricular tachycardia. Circulation, 103(8):1148–1156, 2001.
- [94] B-L Hao. Universal slowing-down exponent near period-doubling bifurcation points. *Phys. Lett. A*, 86(5):267–268, 1981.
- [95] B Heath, K Gingrich, and RS Kass. Ion Channels in the Heart: Cellular and Molecular Properties of Cardiac Na, Ca, and K channels. Compr. Physiol., 2002.
- [96] TJ Herron, P Lee, and J Jalife. Optical imaging of voltage and calcium in cardiac cells & tissues. *Circ. Res.*, 110(4):609–623, 2012.
- [97] AL Hodgkin and AF Huxley. The components of membrane conductance in the giant axon of Loligo. *J. Physiol.*, 116(4):473–496, 1952.

- [98] AL Hodgkin and AF Huxley. Currents carried by sodium and potassium ions through the membrane of the giant axon of Loligo. *J. Physiol.*, 116(4):449–472, 1952.
- [99] AL Hodgkin and AF Huxley. The dual effect of membrane potential on sodium conductance in the giant axon of Loligo. J. Physiol., 116(4):497–506, 1952.
- [100] AL Hodgkin and AF Huxley. A quantitative description of membrane current and its application to conduction and excitation in nerve. *J. Physiol.*, 117(4):500–544, 1952.
- [101] AL Hodgkin, AF Huxley, and B Katz. Measurement of current-voltage relations in the membrane of the giant axon of Loligo. *J. Physiol.*, 116(4):424–448, 1952.
- [102] AV Holden, W Winlow, and PG Haydon. The induction of periodic and chaotic activity in a molluscan neurone. *Biol Cybern.*, 43(3):169–173, 1982.
- [103] X Huang, W Xu, J Liang, K Takagaki, X Gao, and J-Y Wu. Spiral wave dynamics in neocortex. *Neuron*, 68(5):978–990, 2010.
- [104] RE Ideker, X Zhou, and SB Knisley. Correlation among fibrillation, defibrillation, and cardiac pacing. *Pace*, 18(3):512–525, 1995.
- [105] T Ikeda, M Yashima, T Uchida, D Hough, MC Fishbein, WJ Mandel, P-S Chen, and HS Karagueuzian. Attachment of meandering reentrant wave fronts to anatomic obstacles in the atrium role of the obstacle size. Circ. Res., 81(5):753-764, 1997.
- [106] H Ito and L Glass. Spiral breakup in a new model of discrete excitable media. *Phys. Rev. Lett.*, 66(5):671, 1991.
- [107] V Iyer, R Mazhari, and RL Winslow. A computational model of the human left-ventricular epicardial myocyte. *Biophys. J.*, 87(3):1507–1525, 2004.
- [108] B Jia, H Gu, L Li, and X Zhao. Dynamics of period-doubling bifurcation to chaos in the spontaneous neural firing patterns. *Cogn. Neurodyn.*, 6(1):89–106, 2012.
- [109] ME Josephson. Clinical cardiac electrophysiology: techniques and interpretations. Lippincott Williams & Wilkins, 2008.

- [110] HS Karagueuzian, SS Khan, K Hong, Y Kobayashi, T Denton, WJ Mandel, and GA Diamond. Action potential alternans and irregular dynamics in quinidine-intoxicated ventricular muscle cells. Implications for ventricular proarrhythmia. *Circulation*, 87(5):1661–1672, 1993.
- [111] A Karma. Spiral breakup in model equations of action potential propagation in cardiac tissue. *Phys. Rev. Lett.*, 71(7):1103, 1993.
- [112] A Karma. Electrical alternans and spiral wave breakup in cardiac tissue. *Chaos*, 4(3):461–472, 1994.
- [113] A Karma. Physics of cardiac arrhythmogenesis. *Annu. Rev. Condens. Matter Phys.*, 4(1):313–337, 2013.
- [114] JP Keener. Causes of propagation failure in excitable media. In *Temporal Disorder in Human Oscillatory Systems*, pages 134–140. Springer, 1987.
- [115] JP Keener. The dynamics of three-dimensional scroll waves in excitable media. *Physica D*, 31(2):269–276, 1988.
- [116] DT Kim, Y Kwan, JJ Lee, T Ikeda, T Uchida, K Kamjoo, Y-H Kim, JJC Ong, CA Athill, T-J Wu, et al. Patterns of spiral tip motion in cardiac tissues. Chaos, 8(1):137–148, 1998.
- [117] M-Y Kim, M Aguilar, A Hodge, E Vigmond, A Shrier, and L Glass. Stochastic and spatial influences on drug-induced bifurcations in cardiac tissue culture. *Phys. Rev. Lett.*, 103(5):058101, 2009.
- [118] AG Kléber, MJ Janse, and VG Fast. Normal and abnormal conduction in the heart. *Compr. Physiol.*, 2011.
- [119] AG Kléber and U Rudy. Basic mechanisms of cardiac impulse propagation and associated arrhythmias. *Physiol. Rev.*, 84(2):431–488, 2004.
- [120] W Kong, AE Pollard, and VG Fast. A new optrode design for intramural optical recordings. *IEEE T. Bio-Med. Eng.*, 58(11):3130–3134, 2011.
- [121] VI Koroleva and J Bures. Circulation of cortical spreading depression around electrically stimulated areas and epileptic foci in the neocortex of rats. *Brain Res.*, 173(2):209–215, 1979.

- [122] VC Kowtha, A Kunysz, JR Clay, L Glass, and A Shrier. Ionic mechanisms and nonlinear dynamics of embryonic chick heart cell aggregates. *Prog. Biophys. Mol. Biol.*, 61(3):255–281, 1994.
- [123] MA Kramer, W Truccolo, UT Eden, KQ Lepage, LR Hochberg, EN Eskandar, JR Madsen, JW Lee, A Maheshwari, E Halgren, et al. Human seizures self-terminate across spatial scales via a critical transition. *Proc. Natl. Acad. Sci. USA*, 109(51):21116–21121, 2012.
- [124] VI Krinskii. Spread of excitation in an inhomogeneous medium (state similar to cardiac fibrillation). *Biofizika*, 11(4):776, 1966.
- [125] T Krogh-Madsen and DJ Christini. Action potential duration dispersion and alternans in simulated heterogeneous cardiac tissue with a structural barrier. *Biophys. J.*, 92(4):1138–1149, 2007.
- [126] C Kuehn. A mathematical framework for critical transitions: Bifurcations, fast–slow systems and stochastic dynamics. *Physica D*, 240(12):1020–1035, 2011.
- [127] A Kunysz, L Glass, and A Shrier. Overdrive suppression of spontaneously beating chick heart cell aggregates: experiment and theory. *Am. J. Physiol.-Heart C.*, 269(3):H1153–H1164, 1995.
- [128] RS Lankipalli, T Zhu, D Guo, and G-X Yan. Mechanisms underlying arrhythmogenesis in long QT syndrome. J. Electrocardiol., 38(4):69–73, 2005.
- [129] KR Laurita and DS Rosenbaum. Interdependence of modulated dispersion and tissue structure in the mechanism of unidirectional block. *Circ. Res.*, 87(10):922–928, 2000.
- [130] KJ Lee, EC Cox, and RE Goldstein. Competing patterns of signaling activity in dictyostelium discoideum. *Phys. Rev. Lett.*, 76(7):1174, 1996.
- [131] TM Lenton. Early warning of climate tipping points. *Nature Climate Change*, 1(4):201–209, 2011.
- [132] C Lerma, CF Lee, L Glass, and AL Goldberger. The rule of bigeminy revisited: analysis in sudden cardiac death syndrome. *J. Electrocardiol.*, 40(1):78–88, 2007.

- [133] B-W Li, M-C Cai, H Zhang, AV Panfilov, and H Dierckx. Chiral selection and frequency response of spiral waves in reaction-diffusion systems under a chiral electric field. *J. Chem. Phys.*, 140(18):184901, 2014.
- [134] G-R Li, J Feng, L Yue, and M Carrier. Transmural heterogeneity of action potentials and  $I_{to1}$  in myocytes isolated from the human right ventricle. Am. J. Physiol.-Heart C., 275(2):H369–H377, 1998.
- [135] A Libchaber, C Laroche, and S Fauve. Period doubling cascade in mercury, a quantitative measurement. *J. Phys. Lett.*, 43(7):211–216, 1982.
- [136] Q Lu, Z Yang, L Duan, H Gu, and W Ren. Dynamics and transitions of firing patterns in deterministic and stochastic neuronal systems. *Chaos Soliton. Fract.*, 40(2):577–597, 2009.
- [137] C-H Luo and Y Rudy. A model of the ventricular cardiac action potential. Depolarization, repolarization, and their interaction. Circ. Res., 68(6):1501–1526, 1991.
- [138] S Luther, FH Fenton, BG Kornreich, A Squires, P Bittihn, D Hornung, M Zabel, J Flanders, A Gladuli, L Campoy, et al. Low-energy control of electrical turbulence in the heart. *Nature*, 475(7355):235–239, 2011.
- [139] MC Mackey and L Glass. Oscillation and chaos in physiological control systems. *Science*, 197(4300):287–289, 1977.
- [140] A Mahajan, Y Shiferaw, D Sato, A Baher, R Olcese, L-H Xie, M-J Yang, P-S Chen, Juan G Restrepo, A Karma, et al. A rabbit ventricular action potential model replicating cardiac dynamics at rapid heart rates. *Biophys.* J., 94(2):392–410, 2008.
- [141] R Majumder, R Pandit, and AV Panfilov. Turbulent electrical activity at sharp-edged inexcitable obstacles in a model for human cardiac tissue. Am. J. Physiol.-Heart C., 307(7):H1024–H1035, 2014.
- [142] R Mandapati, A Skanes, J Chen, O Berenfeld, and J Jalife. Stable microreentrant sources as a mechanism of atrial fibrillation in the isolated sheep heart. *Circulation*, 101(2):194–199, 2000.
- [143] RM May. Thresholds and breakpoints in ecosystems with a multiplicity of stable states. *Nature*, 269(5628):471–477, 1977.

- [144] RM May, SA Levin, and G Sugihara. Complex systems: Ecology for bankers. *Nature*, 451(7181):893–895, 2008.
- [145] PE McSharry, LA Smith, and L Tarassenko. Prediction of epileptic seizures: are nonlinear methods relevant? *Nat. Med.*, 9(3):241–242, 2003.
- [146] J Milton and P Jung. *Epilepsy as a dynamic disease*. Springer Science & Business Media, 2002.
- [147] GR Mines. On dynamic equilibrium in the heart. *J. Physiol.*, 46(4-5):349–383, 1913.
- [148] GK Moe, WC Rheinboldt, and JA Abildskov. A computer model of atrial fibrillation. Am. Heart J., 67(2):200–220, 1964.
- [149] JM Morgan, D Cunningham, and E Rowland. Dispersion of monophasic action potential duration: demonstrable in humans after premature ventricular extrastimulation but not in steady state. *J. Am. Coll. Cardiol.*, 19(6):1244–1253, 1992.
- [150] SC Müller, T Plesser, and B Hess. The structure of the core of the spiral wave in the Belousov-Zhabotinskii reaction. *Science*, 230(4726):661–663, 1985.
- [151] J Nagumo, S Arimoto, and S Yoshizawa. An active pulse transmission line simulating nerve axon. *Proc. IRE.*, 50(10):2061–2070, 1962.
- [152] SM Narayan, DE Krummen, K Shivkumar, P Clopton, W-J Rappel, and JM Miller. Treatment of atrial fibrillation by the ablation of localized sources: CONFIRM (Conventional Ablation for Atrial Fibrillation With or Without Focal Impulse and Rotor Modulation) trial. *J. Am. Coll. Cardiol.*, 60(7):628–636, 2012.
- [153] D Noble. A modification of the Hodgkin-Huxley equations applicable to Purkinje fibre action and pacemaker potentials. *J. Physiol.*, 160(2):317–352, 1962.
- [154] JB Nolasco and RW Dahlen. A graphic method for the study of alternation in cardiac action potentials. *J. Appl. Physiol.*, 25(2):191–196, 1968.

- [155] T Nomura and L Glass. Entrainment and termination of reentrant wave propagation in a periodically stimulated ring of excitable media. *Phys. Rev.* E, 53(6):6353, 1996.
- [156] NF Otani. Termination of reentrant cardiac action potential propagation using far-field electrical pacing. *IEEE T. Bio-Med. Eng.*, 58(7):2013–2022, 2011.
- [157] E Pálsson and EC Cox. Origin and evolution of circular waves and spirals in Dictyostelium discoideum territories. *Proc. Natl. Acad. Sci. USA*, 93(3):1151–1155, 1996.
- [158] SV Pandit, RB Clark, WR Giles, and SS Demir. A mathematical model of action potential heterogeneity in adult rat left ventricular myocytes. *Biophys.* J., 81(6):3029–3051, 2001.
- [159] AV Panfilov and JP Keener. Effects of high frequency stimulation on cardiac tissue with an inexcitable obstacle. *J. Theor. Biol.*, 163(4):439–448, 1993.
- [160] JM Pastore, SD Girouard, KR Laurita, FG Akar, and DS Rosenbaum. Mechanism linking T-wave alternans to the genesis of cardiac fibrillation. *Circulation*, 99(10):1385–1394, 1999.
- [161] JM Pastore and DS Rosenbaum. Role of structural barriers in the mechanism of alternans-induced reentry. *Circ. Res.*, 87(12):1157–1163, 2000.
- [162] D Paydarfar and DM Buerkel. Dysrhythmias of the respiratory oscillator. *Chaos*, 5(1):18–29, 1995.
- [163] AM Pertsov, JM Davidenko, R Salomonsz, WT Baxter, and J Jalife. Spiral waves of excitation underlie reentrant activity in isolated cardiac muscle. *Circ. Res.*, 72(3):631–650, 1993.
- [164] AM Pertsov and EA Ermakova. Mechanism of the drift of a spiral wave in an inhomogeneous-medium. *Biofizika*, 33(2):338–342, 1988.
- [165] SG Priori, E Aliot, C Blomstrom-Lundqvist, L Bossaert, G Breithardt, P Brugada, AJ Camm, R Cappato, SM Cobbe, C Di Mario, et al. Task force on sudden cardiac death of the European Society of Cardiology. Eur. Heart J., 22(16):1374–1450, 2001.

- [166] A Pumir, V Nikolski, M Hörning, A Isomura, K Agladze, K Yoshikawa, R Gilmour, E Bodenschatz, and V Krinsky. Wave emission from heterogeneities opens a way to controlling chaos in the heart. *Phys. Rev. Lett.*, 99(20):208101, 2007.
- [167] T Quail, N McVicar, M Aguilar, M-Y Kim, A Hodge, L Glass, and A Shrier. Chaotic dynamics in cardiac aggregates induced by potassium channel block. Chaos, 22(3):033140, 2012.
- [168] ML Riccio, ML Koller, and RF Gilmour. Electrical restitution and spatiotemporal organization during ventricular fibrillation. Circ. Res., 84(8):955–963, 1999.
- [169] DM Roden, R Lazzara, M Rosen, PJ Schwartz, J Towbin, GM Vincent, et al. Multiple mechanisms in the long-QT syndrome current knowledge, gaps, and future directions. *Circulation*, 94(8), 1996.
- [170] JM Rogers. Wave front fragmentation due to ventricular geometry in a model of the rabbit heart. *Chaos*, 12(3):779–787, 2002.
- [171] DS Rosenbaum, LE Jackson, JM Smith, H Garan, JN Ruskin, and RJ Cohen. Electrical alternans and vulnerability to ventricular arrhythmias. New Engl. J. Med., 330(4):235–241, 1994.
- [172] KJ Sampson and CS Henriquez. Interplay of ionic and structural heterogeneity on functional action potential duration gradients: Implications for arrhythmogenesis. *Chaos*, 12(3):819–828, 2002.
- [173] MC Sanguinetti, C Jiang, ME Curran, and MT Keating. A mechanistic link between an inherited and an acquired cardiac arrhythmia: HERG encodes the  $I_{Kr}$  potassium channel. Cell, 81(2):299–307, 1995.
- [174] MC Sanguinetti and NK Jurkiewicz. Two components of cardiac delayed rectifier K+ current. Differential sensitivity to block by class III antiarrhythmic agents. J. Gen. Physiol., 96(1):195–215, 1990.
- [175] MC Sanguinetti and M Tristani-Firouzi. hERG potassium channels and cardiac arrhythmia. *Nature*, 440(7083):463–469, 2006.
- [176] N Saoudi, F Cosio, A Waldo, S-A Chen, Y Iesaka, M L, S Saksena, J Salerno, and W Schoels. Classification of atrial flutter and regular atrial tachycardia according to electrophysiologic mechanism and anatomic bases: a

- statement from a joint expert group from the Working Group of Arrhythmias of the European Society of Cardiology and the North American Society of Pacing and Electrophysiology. *J. Cardiovasc. Electrophysiol.*, 12(7):852–866, 2001.
- [177] D Sato, DM Bers, and Y Shiferaw. Formation of spatially discordant alternans due to fluctuations and diffusion of calcium. *PLOS ONE*, 8(12):e85365, 2013.
- [178] D Sato, L-H Xie, TP Nguyen, JN Weiss, and Z Qu. Irregularly appearing early afterdepolarizations in cardiac myocytes: random fluctuations or dynamical chaos? *Biohpys. J.*, 99(3):765–773, 2010.
- [179] D Sato, L-H Xie, AA Sovari, DX Tran, N Morita, F Xie, H Karagueuzian, A Garfinkel, JN Weiss, and Z Qu. Synchronization of chaotic early afterdepolarizations in the genesis of cardiac arrhythmias. *Proc. Natl. Acad. Sci.* USA, 106(9):2983–2988, 2009.
- [180] M Scheffer, J Bascompte, WA Brock, V Brovkin, SR Carpenter, V Dakos, H Held, EH Van Nes, M Rietkerk, and G Sugihara. Early-warning signals for critical transitions. *Nature*, 461(7260):53–59, 2009.
- [181] TK Shajahan, B Borek, A Shrier, and L Glass. Scaling properties of conduction velocity in heterogeneous excitable media. *Phys. Rev. E*, 84(4):046208, 2011.
- [182] TK Shajahan, B Borek, A Shrier, and L Glass. Spiral–pacemaker interactions in a mathematical model of excitable medium. *New J. Phys.*, 15(2):023028, 2013.
- [183] T Shibasaki. Conductance and kinetics of delayed rectifier potassium channels in nodal cells of the rabbit heart. *J. Physiol.*, 387(1):227–250, 1987.
- [184] A Shrier and JR Clay. Repolarization currents in embryonic chick atrial heart cell aggregates. *Biophys. J.*, 50(5):861, 1986.
- [185] RH Simoyi, A Wolf, and HL Swinney. One-dimensional dynamics in a multicomponent chemical reaction. *Phys. Rev. Lett.*, 49(4):245, 1982.
- [186] S Sinha, KM Stein, and DJ Christini. Critical role of inhomogeneities in pacing termination of cardiac reentry. *Chaos*, 12(3):893–902, 2002.

- [187] JM Smith, EA Clancy, CR Valeri, JN Ruskin, and RJ Cohen. Electrical alternans and cardiac electrical instability. *Circulation*, 77(1):110–121, 1988.
- [188] JM Starobin and CF Starmer. Boundary-layer analysis of waves propagating in an excitable medium: Medium conditions for wave-front-obstacle separation. *Phys. Rev. E*, 54(1):430, 1996.
- [189] JM Starobin, YI Zilberter, EM Rusnak, and CF Starmer. Wavelet formation in excitable cardiac tissue: the role of wavefront-obstacle interactions in initiating high-frequency fibrillatory-like arrhythmias. *Biophys. J.*, 70(2):581–594, 1996.
- [190] O Steinbock, J Schütze, and SC Müller. Electric-field-induced drift and deformation of spiral waves in an excitable medium. *Phys. Rev. Lett.*, 68(2):248, 1992.
- [191] WG Stevenson, PL Friedman, PT Sager, LA Saxon, D Kocovic, T Harada, I Wiener, and H Khan. Exploring postinfarction reentrant ventricular tachycardia with entrainment mapping. J. Am. Coll. Cardiol., 29(6):1180– 1189, 1997.
- [192] WG Stevenson, H Khan, Ph Sager, LA Saxon, HR Middlekauff, PD Natterson, and I Wiener. Identification of reentry circuit sites during catheter mapping and radiofrequency ablation of ventricular tachycardia late after myocardial infarction. *Circulation*, 88(4):1647–1670, 1993.
- [193] MO Sweeney. Antitachycardia pacing for ventricular tachycardia using implantable cardioverter defibrillators. *Pace*, 27(9):1292–1305, 2004.
- [194] P Talkner and P Hänggi. In F Moss and P McClintock, editors, Noise in Nonlinear Dynamical Systems, volume 2, pages 87–99. Cambridge University Press, 1989.
- [195] AJ Tanskanen, JL Greenstein, B O'Rourke, and RL Winslow. The role of stochastic and modal gating of cardiac L-type Ca 2+ channels on early after-depolarizations. *Biophys. J.*, 88(1):85–95, 2005.
- [196] KHWJ Ten Tusscher, D Noble, PJ Noble, and AV Panfilov. A model for human ventricular tissue. Am. J. Physiol.-Heart C., 286(4):H1573-H1589, 2004.

- [197] NA Trayanova. Whole-heart modeling applications to cardiac electrophysiology and electromechanics. *Circ. Res.*, 108(1):113–128, 2011.
- [198] JJ Tyson and JP Keener. Singular perturbation theory of traveling waves in excitable media (a review). *Physica D*, 32(3):327–361, 1988.
- [199] B Van der Pol and J Van der Mark. LXXII: The heartbeat considered as a relaxation oscillation, and an electrical model of the heart. *Philos. Mag.*, 6(38):763–775, 1928.
- [200] AO Verkerk, R Wilders, MMGJ van Borren, RJG Peters, E Broekhuis, K Lam, R Coronel, JMT de Bakker, and HL Tan. Pacemaker current  $(I_f)$  in the human sinoatrial node. Eur. Heart J., 28(20):2472-2478, 2007.
- [201] RL Verrier, T Klingenheben, K Malik, N El-Sherif, DV Exner, SH Hohnloser, T Ikeda, JP Martínez, SM Narayan, T Nieminen, et al. Microvolt T-wave alternans: Physiological basis, methods of measurement, and clinical utility? Consensus guideline by International Society for Holter and Noninvasive Electrocardiology. J. Am. Coll. Cardiol., 58(13):1309–1324, 2011.
- [202] RL Verrier and M Malik. Quantitative T-wave alternans analysis for guiding medical therapy: An underexploited opportunity. *Trends Cardiovasc. Med.*, 2014.
- [203] GP Walcott, CR Killingsworth, and RE Ideker. Do clinically relevant transthoracic defibrillation energies cause myocardial damage and dysfunction? *Resuscitation*, 59(1):59–70, 2003.
- [204] AL Waldo and AL Wit. Mechanisms of cardiac arrhythmias. *Lancet*, 341(8854):1189–1193, 1993.
- [205] R Wang, JA Dearing, PG Langdon, E Zhang, X Yang, V Dakos, and M Scheffer. Flickering gives early warning signals of a critical transition to a eutrophic lake state. *Nature*, 492(7429):419–422, 2012.
- [206] MA Watanabe, FH Fenton, SJ Evans, HM Hastings, and A Karma. Mechanisms for discordant alternans. J. Cardiovasc. Electrophysiol., 12(2):196–206, 2001.
- [207] LD Weise and AV Panfilov. Emergence of spiral wave activity in a mechanically heterogeneous reaction-diffusion-mechanics system. *Phys. Rev. Lett.*, 108(22):228104, 2012.

- [208] N Wiener and A Rosenblueth. The mathematical formulation of the problem of conduction of impulses in a network of connected excitable elements, specifically in cardiac muscle. *Arch. Inst. Cardiol. Mex.*, 16(3):205–265, 1946.
- [209] K Wiesenfeld. Noisy precursors of nonlinear instabilities. *J. Stat. Phys.*, 38(5-6):1071–1097, 1985.
- [210] AT Winfree. Spiral waves of chemical activity. *Science*, 175(4022):634–636, 1972.
- [211] AT Winfree. Electrical instability in cardiac muscle: phase singularities and rotors. J. Theor. Biol., 138(3):353–405, 1989.
- [212] AT Winfree. Alternative stable rotors in an excitable medium. *Physica D*, 49(1):125-140, 1991.
- [213] AT Winfree. Varieties of spiral wave behavior: An experimentalist's approach to the theory of excitable media. *Chaos*, 1(3):303–334, 1991.
- [214] FX Witkowski, LJ Leon, PA Penkoske, WR Giles, ML Spano, WL Ditto, and AT Winfree. Spatiotemporal evolution of ventricular fibrillation. *Nature*, 392(6671):78–82, 1998.
- [215] A Xu and MR Guevara. Two forms of spiral-wave reentry in an ionic model of ischemic ventricular myocardium. *Chaos*, 8(1):157–174, 1998.
- [216] G-X Yan, Y Wu, T Liu, J Wang, RA Marinchak, and PR Kowey. Phase 2 early afterdepolarization as a trigger of polymorphic ventricular tachycardia in acquired long-QT syndrome direct evidence from intracellular recordings in the intact left ventricular wall. *Circulation*, 103(23):2851–2856, 2001.
- [217] RM Zaritski and AM Pertsov. Stable spiral structures and their interaction in two-dimensional excitable media. *Phys. Rev. E*, 66(6):066120, 2002.
- [218] EC Zeeman. Catastrophe theory: Selected papers, 1972–1977. Addison-Wesley, 1977.
- [219] CW Zemlin, K Mukund, VN Biktashev, and AM Pertsov. Dynamics of bound states of same-chirality spiral waves. *Phys. Rev. E*, 74(1):016207, 2006.

- [220] CW Zemlin, K Mukund, M Wellner, R Zaritsky, and AM Pertsov. Asymmetric bound states of spiral pairs in excitable media. *Phys. Rev. Lett.*, 95(9):098302, 2005.
- [221] CW Zemlin and AM Pertsov. Anchoring of drifting spiral and scroll waves to impermeable inclusions in excitable media. *Phys. Rev. Lett.*, 109(3):038303, 2012.
- [222] X Zhao, DG Schaeffer, CM Berger, and DJ Gauthier. Small-signal amplification of period-doubling bifurcations in smooth iterated maps. *Nonlin. Dyn.*, 48(4):381–389, 2007.